NUREG/CR-3806
ANL-84-36

NUREG/CR-3806
ANL-84-36

ENVIRONMENTALLY ASSISTED CRACKING IN LIGHT WATER REACTORS:

ANNUAL REPORT

October 1982 – September 1983

by

W. J. Shack, T. F. Kassner, D. S. Kupperman,
T. N. Claytor, J. Y. Park, P. S. Maiya,
W. E. Ruther, and F. A. Nichols

ARGONNE NATIONAL LABORATORY, ARGONNE, ILLINOIS
Operated by THE UNIVERSITY OF CHICAGO

Prepared for the Office of Nuclear Regulatory Research
U. S. NUCLEAR REGULATORY COMMISSION
under Interagency Agreement DOE 40-550-75

Argonne National Laboratory, with facilities in the states of Illinois and Idaho, is owned by the United States government, and operated by The University of Chicago under the provisions of a contract with the Department of Energy.

NUREG/CR-3806
ANL-84-36

Distribution
Code: R5

ARGONNE NATIONAL LABORATORY
9700 South Cass Avenue
Argonne, Illinois 60439

ENVIRONMENTALLY ASSISTED CRACKING IN LIGHT WATER REACTORS:

ANNUAL REPORT
October 1982—September 1983

by

W. J. Shack, T. F. Kassner, D. S. Kupperman,
T. N. Claytor,* J. Y. Park, P. S. Maiya,
W. E. Ruther, and F. A. Nichols

Materials Science and Technology Division

Report Completed
June 1984

Prepared for the Division of Engineering Technology
Office of Nuclear Regulatory Research
U. S. Nuclear Regulatory Commission
Washington, D. C. 20555

NRC FIN No. A2212

*Components Technology Division

ENVIRONMENTALLY ASSISTED CRACKING IN LIGHT WATER REACTORS: ANNUAL REPORT

October 1982 -- September 1983

ABSTRACT

This progress report summarizes work performed by the Argonne National Laboratory and subcontractors at GARD Inc., Pacific Northwest Laboratory, and E. F. Rybicki, Inc. on environmentally assisted cracking in light water reactors during the twelve months from October 1982 to September 1983.

NRC FIN No.	FIN Title
A2212	Environmentally Assisted Cracking in Light Water Reactors

TABLE OF CONTENTS

TABLE OF CONTENTS (Contd.)

ENVIRONMENTALLY ASSISTED CRACKING IN LIGHT-WATER REACTORS: ANNUAL REPORT[a]

October 1982--September 1983

Executive Summary

Leaks and cracks in the heat-affected zones (HAZs) of weldments in austenitic stainless steel piping and associated components in boiling water reactors (BWRs) have been observed since the mid-1960s. Cracking has continued to occur and indications have been found in all parts of the recirculation system including the largest-diameter lines. Proposed remedies include (1) procedures primarily intended to produce a more favorable residual stress state in the HAZ adjacent to welds, (2) replacement of the piping with materials that are more resistant to stress corrosion cracking, and (3) modification of the reactor coolant environment to decrease the susceptibility to cracking. In addition to evaluating these remedies it is also important to understand the influence of key variables, such as residual stress, crack growth rates, and the margin for leak-before-break (LBB) in flawed piping, which may impact regulatory decisions on operating plants.

Finite element calculations of the stresses in 12- and 24-in.-dia pipes that have undergone Induction-Heating-Stress-Improvement (IHSI) or weld overlay procedures have been carried out for piping with flaws. For shallow cracks these processes still produce compressive residual stress states on the inner surface, and the stresses at the crack tips remain compressive under design loads. Additional analyses are needed to determine the maximum crack depths for which the processes are effective. The LBB margin for piping with a part-through crack completely around the circumference and a throughwall crack over a portion of the circumference has been assessed. Even severely degraded piping is shown to have a significant LBB margin, although the available margin decreases rapidly with increases in depth of the part-through crack.

---

[a]RSR FIN Budget No. A2212; RSR Contact: J. Muscara.

Most of the available data on crack growth rates for Type 304 stainless steel have been obtained on furnace-sensitized materials in high-purity water with 8 ppm dissolved oxygen under constant load. Crack growth tests are currently in progress to investigate the effect of impurities, loading history, and the degree of sensitization on crack growth rates in more prototypic BWR environments. However, since crack growth tests are extremely time consuming, only a limited number of these parameters can be examined, and constant-extension-rate-tensile (CERT) tests are being carried out for a much wider range of conditions.

The CERT tests have shown a strong synergistic interaction between the dissolved oxygen and impurity concentrations of the water. For dissolved oxygen concentrations between 0.1 and 8 ppm, even low levels of impurities (viz., 0.1 ppm sulfate or chloride) markedly increase intergranular stress-corrosion cracking (IGSCC) to the extent that the susceptibility is not a strong function of the oxygen concentration over this range. Similarly, impurities diminish variations in IGSCC susceptibility owing to the degree of sensitization of the steel. Materials that are susceptible to cracking in both high-purity and impurity environments show higher crack propagation rates in the impurity environments ($\sim$2-3 times faster).

At the much lower dissolved oxygen levels (<50 ppb) that can be achieved with hydrogen additions ($\sim$2 ppm) to the feedwater in BWRs, the susceptibility to IGSCC decreases significantly. However, careful control of impurity levels will also be required. Although our current results illustrate the interaction between dissolved oxygen and impurity concentration, we are not able at present to define tolerable levels for the impurities in low-oxygen coolant environments.

The most widely used alternative piping material is Type 316 "Nuclear Grade" stainless steel with controlled carbon and nitrogen levels. Laboratory tests have demonstrated a high resistance of this steel to IGSCC in pure water, but much less testing has been carried out in environments with low levels of impurities typical of BWR recirculating loop water under normal operation. Our results have confirmed the resistance of Type 316NG to IGSCC in impurity environments for heat treatments associated with weld

sensitization in Types 304 and 316 SS. However, transgranular cracking has been observed in CERT tests in environments with chlorides and sulfates. This may be an artifact of the high strains produced in these tests, but preliminary information indicates that the cracks appear to initiate at fairly low strains. Even in these cases the crack growth rates are about an order of magnitude lower than the intergranular crack growth rates observed in conventional Type 304 SS under the same conditions.

Laboratory testing of materials intended to have a 30-year lifetime invariably requires accelerated testing. To extrapolate confidently from these tests to in-reactor loading situations, a better understanding of the effects of loading history on stress-corrosion cracking (SCC) susceptibility and of the mechanisms actually involved in the cracking process is needed. A model, which is based on an estimate of the crack-tip strain rate, has been used to develop correlations between the measured parameters in the slow strain rate test (i.e., the crack propagation rate, time to failure, maximum stress, etc.,) and the nominal strain rate.

Tests have also been performed to examine IGSCC susceptibility under pure torsion (mode III) and tensile loading (mode I). Relatively long failure times (greater than a factor of 50) have been observed under constant torsional loads compared to tensile loads at the same fraction of the ultimate strength for sensitized Type 304 SS in 289°C water with 8 ppm dissolved oxygen and 0.1 ppm sulfate as H_2SO_4. These very tentative results suggest that atomic hydrogen from the corrosion process may play a role in IGSCC of Type 304 SS in BWR-like environments.

Characterization of acoustic signals and leak rates from cracks produced by mechanical and thermal fatigue and IGSCC has begun in the acoustic leak detection (ALD) test facility. Data were obtained on two field-induced intergranular cracks. The minimum leak rate that is detectable through intergranular cracks at a distance of 0.5 m is 0.001 gal/min under laboratory conditions for a frequency window of 200-400 kHz. A comparison of acoustic spectra from two cracks at a leak rate of 0.005 gal/min revealed nearly identical signals in this frequency range. These data suggest that geometrical effects may be less significant at frequencies above 200 kHz.

Cross-correlation techniques for locating leaks and distinguishing among leak types were also demonstrated.

After ultrasonic testing revealed cracks in the recirculation header of the Georgia Power Co. Hatch-1 BWR, an ALD system was installed. The leak detection system at Hatch was reproduced and evaluated to determine the sensitivity and dynamic range. The results suggest that the background noise in the range from 200 to 400 kHz at a recirculation header of a BWR operating at full power is only a few decibels above the electronic noise. At a distance of 0.5 m the system should be capable of detecting leaks of less than 0.01 gal/min. Other background data have been acquired at the Watts Bar Nuclear Reactor in Tennessee. An ANL waveguide system, including transducer and electronics, was installed (in cooperation with PNL) on an accumulator safety injection pipe. Data were acquired on background noise from 50 to 400 kHz during the hot functional test. Significant effort was expended to develop hardware for the acoustic leak detection system. Under a subcontract to ANL, GARD Inc. established a system configuration and then proposed a breadboard system.

The possibility of using ultrasonic wave scattering patterns to discriminate between intergranular cracks and geometric reflectors has been explored. Thirteen reflectors (e.g., field- and graphite-wool-induced intergranular cracks, weld roots, and slits) were examined. This work led to the design and fabrication of a 7-element skew-angle probe for 28-in.-dia pipe, which was assembled for ANL by Magnaflux Corp. This probe is now being evaluated for its capability to distinguish cracks from geometrical reflectors. The nondestructive evaluation (NDE) work with cast stainless steel included acquisition of data on the velocity and attenuation of sound in isotropic and anisotropic cast stainless steel.

ENVIRONMENTALLY ASSISTED CRACKING IN LIGHT-WATER REACTORS: ANNUAL REPORT

October 1982--September 1983

by

W. J. Shack, T. F. Kassner, D. S. Kupperman, T. N. Claytor, J. Y. Park, P. S. Maiya, W. E. Ruther, and F. A. Nichols

The objective of this program is to develop an independent capability for prediction, detection, and control of intergranular stress corrosion cracking (IGSCC) in light-water reactor (LWR) systems. The program is primarily directed at IGSCC problems in existing plants, but also includes the development of recommendations for plants under construction and future plants. The scope includes the following: (1) development of the means to evaluate acoustic leak detection systems objectively and quantitatively; (2) evaluation of the influence of metallurgical variables, stress, and the environment on IGSCC susceptibility, including the influence of plant operations on these variables; and (3) examination of practical limits for these variables to effectively control IGSCC in LWR systems. The initial experimental work concentrates primarily on problems related to pipe cracking in BWR systems. However, ongoing research work on other environmentally assisted cracking problems involving pressure vessels, nozzles, and turbines will be monitored and assessed, and where unanswered technical questions are identified, experimental programs to obtain the necessary information will be developed to the extent that available resources permit.

The effort is divided into six subtasks: (A) Leak Detection and Nondestructive Evaluation; (B) Analysis of Sensitization; (C) Crack Growth Rate Studies; (D) Evaluation of Nonenvironmental Corrective Actions; (E) Evaluation of Environmental Corrective Actions; and (F) Mechanistic Studies. These subtasks reflect major technical concerns associated with IGSCC in LWR systems, namely: leak and crack detection, the role of materials susceptibility, the role of stress in crack initiation and propagation, and the role of the environment. The program seeks to evaluate potential solutions to IGSCC problems in LWRs, by direct experimentation (including full-scale welded pipe tests), by analysis of components from operating reactors, and through the development of a better basic understanding of the various phenomena.

A. Leak Detection and Nondestructive Evaluation (D. Kupperman, T. N. Claytor, R. Groenwald* and R. N. Lanham)

1. Background

No currently available single leak-detection method combines optimal leakage detection sensitivity, leak-locating capability, and leakage measurement accuracy. For example, while quantitative leakage determination is possible with condensate flow monitors, sump monitors, and primary coolant inventory balance, these methods are not adequate for locating leaks and may not have adequate sensitivity to meet code requirements.

Improved leak detection capability at specified sites is possible by use of acoustic monitoring or moisture-sensitive tape technology. However, current acoustic monitoring has no source discrimination (i.e., pipe cracks or valve leaks) and provides no flow rate information (a small leak may saturate the system). Moisture-sensitive tape also does not provide quantitative leak rate information and gives no specific location information other than location of tape; moreover, its usefulness with the new "soft blanket" insulation needs to be demonstrated. Leak detection techniques require further improvement in the following areas: (1) identifying leak sources through location information and leak characterization, so as to eliminate false calls; (2) quantifying and monitoring leak rates; and (3) minimizing the number of installed transducers in a "complete" system through increased sensitivity.

Since the issuance of NRC IE bulletins 83-02 and 82-03 and the training of ultrasonic inspection personnel, the probability of detecting IGSCC under field conditions has increased. However, it appears that the increased sensitivity of current inspections has resulted in considerable overcalling by field inspectors. The detection of IGSCC and the discrimination of intergranular cracks from geometric and metallurgical reflectors are difficult technical goals. The ultrasonic inspection of cast stainless steel using the current UT techniques applied in the field is another difficult technical problem to resolve.

---

*GARD, Inc., Niles, Illinois.

2. Objectives

The objectives of this program for leak detection are a) develop a facility to quantitatively evaluate acoustic leak detection systems, b) assess the effectiveness and reliability of acoustic leak detection techniques, c) develop a prototype acoustic leak detection system, d) establish sensitivity, reliability, and decision-making capability of a prototype system through laboratory testing, and e) assess the effectiveness of a field-implementable acoustic leak detection system. The program will establish whether meaningful quantitative data on leak rates and location can be obtained from acoustic signatures of leaks due to cracks (IGSCC and fatigue) in low- and high-pressure lines, and whether these can be distinguished from other types of leaks. It will also establish calibration procedures for acoustic data acquisition and show whether advanced signal processing can be employed to enhance the adequacy of ALD schemes.

The program objectives for ultrasonic NDE are a) assess the adequacy of a multielement skew angle probe to distinguish intergranular cracks from geometrical reflectors, b) assess a field implementable method for characterizing cast SS microstructure to determine in-service inspection (ISI) reliability, and c) evaluate new ultrasonic inspection problems (i.e., weld overlays).

3. Technical Progress

a. Leak Detection

(1) Description of the Acoustic Leak Detection Facility

Figure 1 shows a photograph of the system, which consists of ∿30 feet (10 m) of 10-in. Schedule 80 piping in a "U" shape. One part of the pipe run (left), used for testing radioactive pipe sections with field-induced leaks (2 installed), is housed in an exhaust hood to prevent any radioactivity from entering the room during testing. Another part of the pipe run (right) is used to test nonradioactive pipe sections containing artificial leaks and laboratory-grown cracks (2 thermal fatigue, 3 fatigue cracks).

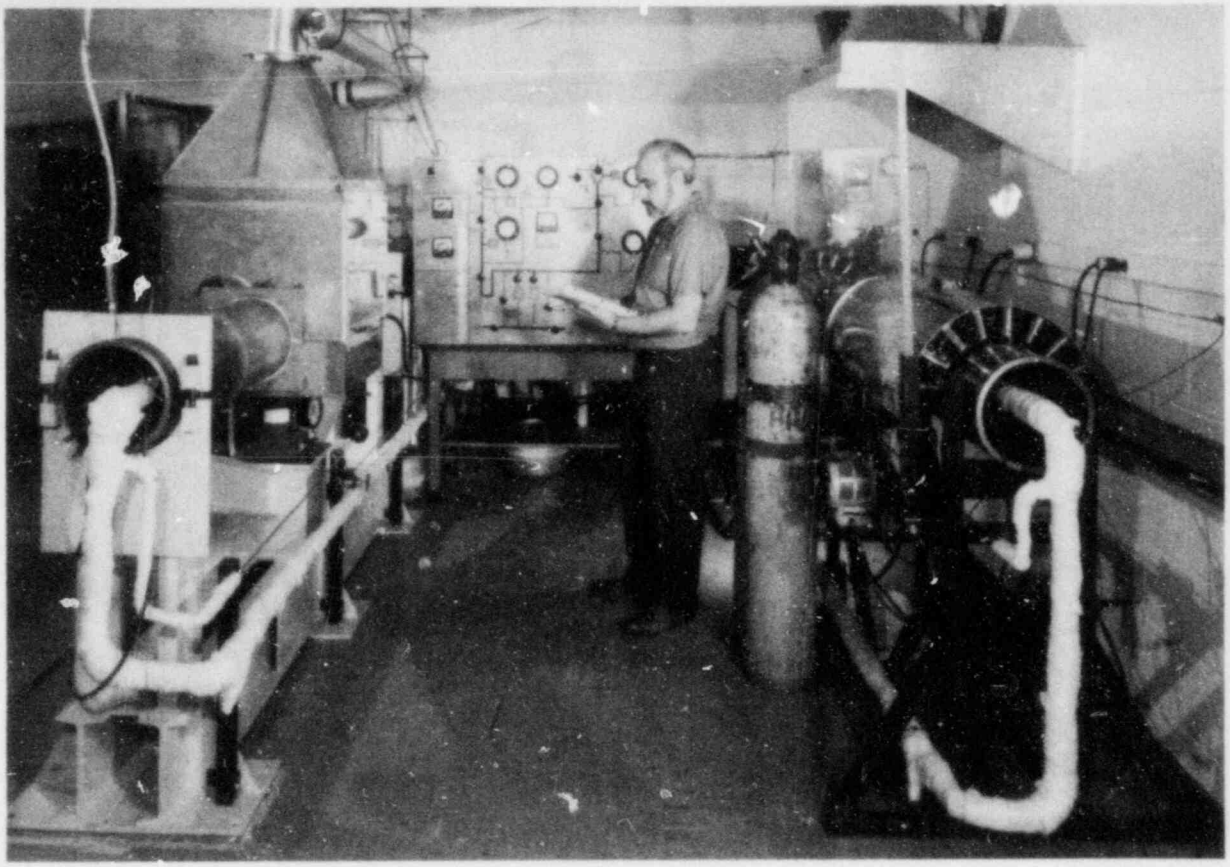

Fig. 1. Photograph of Acoustic Leak Detection Facility.

The system for supplying pressurized hot water to the leak site is at the rear. A small pressure vessel is welded to the inner surface of a pipe section that contains the leak to be tested. The pipe section is then welded or soldered into an opening in the wall of the 10-in. pipe run. The pipe run currently can be stressed to vary the crack opening and thus the leak rate.

Transducers are placed at several locations along the pipe run to acquire acoustic data from the leaks and establish the attenuation characteristics and leak location capability. Insulation of the type used in reactors is added to sections of the piping to determine its effect on acoustic signal generation and attenuation. To better simulate in-reactor conditions, the pipe is filled with water. For high-temperature tests, however, internal dams isolate the region near the crack. This is necessary to reduce heat losses and permit the cracked region to be heated efficiently.

Detection of leak requires that $S_e = S_1 - T_1 - N_1 + PG > 0$ where S_e = signal excess at detector output, S_1 = source level and is affected by waveguide geometry, insulation, and circumferential position, T_1 = transmission loss down the pipe, N_1 = background noise level and PG = system gain (all terms are dB). Data on all terms of this relationship have now been acquired and will be discussed in the following sections.

(2) Characteristics of Leaks from IGSCC

As a result of the high temperature (∿540°F; ∿282°C) and pressure (∿1100 psi; 7.6 MPa) of water in BWR piping, leakage from intergranular cracks will involve two-phase flow. Both the characteristics of the flow and the concomitant generation of acoustic signals are extremely complex and difficult to model. Relatively simple two-phase flow models, which appear at least qualitatively correct, have been developed by Henry[1] and a computer program based on this model has been developed by Collier et al.[2] The model predicts that the flow rate increases as the temperature of the fluid decreases. An increase in flow with decreasing temperature was, in fact, observed experimentally for an intergranular crack.[3]

As discussed in previous reports,[3,4] an increase in the acoustic signal generally occurs when the flow rate is increased at constant temperature. However, this is not always the case.[4] For comparable conditions, data have been generated that show decreasing acoustic signal with increasing flow rate at values of <0.01 gal/min. For constant flow rates, the acoustic signal decreases with fluid temperature. Fortunately, the effect is not severe near BWR operating temperatures. Figure 2 shows a curve for a flow rate of ∿0.005 gal/min.

The spectra of acoustic leak signals have also been measured previously[3] with a special broadband receiver with a conically shaped piezoelectric element. The frequency response of this probe approaches that of a capacitance transducer. The power spectrum obtained for a leak through an intergranular crack at a flow rate of ∿0.004 gal/min (15 cm^3/min) falls off by ∿16-20 dB over the frequency range from 100 to 500 kHz. Beyond 500 kHz, very little if any acoustic signal was detected. These data are

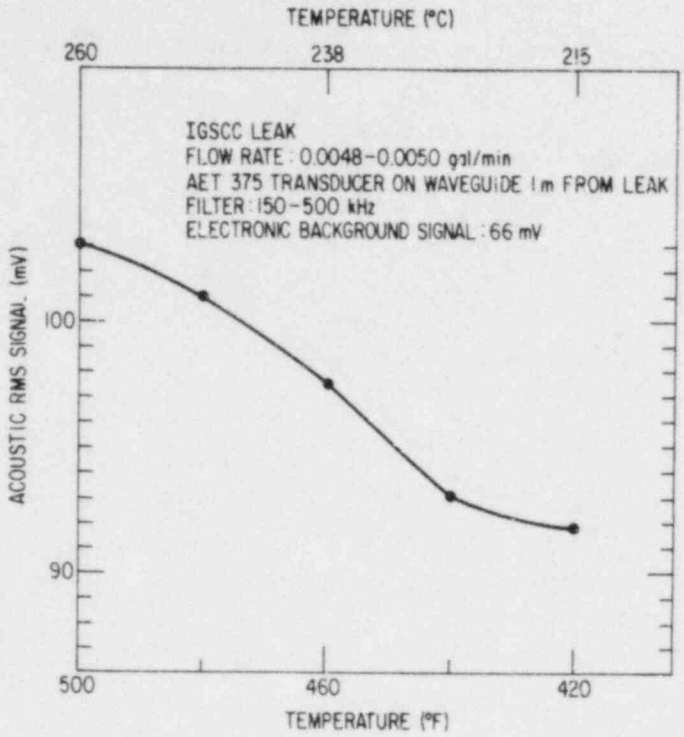

Fig. 2. Acoustic Signal vs Fluid Temperature for Constant Flow Rate.

consistent with the Skudrzyk and Haddle model,[5] which relates the acoustic signal to turbulent flow in the crack and predicts a $(\text{frequency})^{-3}$ dependence for the power spectrum (a 21-dB drop over the range from 100 to 500 kHz).

It is important to identify a suitable frequency "window" for a field acoustic leak detection system. This can be accomplished by comparing leak spectra with background noise data for reactors to determine a frequency range with a favorable signal-to-noise ratio and observing how well acoustic data correlate with flow rates. Data from the monitoring at the Watts Bar reactor (see Section 6) and from the literature[6] show that the background noise is reduced significantly at frequencies above 200 kHz. Even flow from a small intergranular crack (flow rate of ~0.004 gal/min or 15 cm^3/min) produces a significant acoustic signal in the frequency range from 300 to 400 kHz; therefore, this may be the optimum window. In this frequency range, the attenuation is only about 2 dB/m.

Factors that can affect the acoustic leak signal have been discussed[3,7] and the results are reviewed in this report. The presence of waveguides, pipe insulation, and electrical interference, and the relative circumferential position of the transducer and leak site must be considered when carrying out an analysis of acoustic leak signals. The most significant effect is produced by insulation, which can cause an increase in acoustic signal; the magnitude of the increase appears to depend on the flow rate of the leak. For a slit-type leak with a low flow rate (∿0.02 gal/min or ∿80 cm^3/min), the addition of mirror insulation has been shown to enhance a signal by ∿5 to 15 dB in the frequency range from 200 to 500 kHz. For a slit-type leak with a higher flow rate (∿0.2 gal/min or ∿900 cm^3/min), the signal increased by less than 3 dB when insulation was added. However, the addition of insulation did not significantly enhance the signal from the intergranular crack at a flow rate of <0.01 gal/min.

(3) Acoustic Signal vs Leak Rate Data

Three fatigue and two thermal fatigue cracks have been welded into the pipe run. Tests have begun with these laboratory-grown cracks. Originally, one of the leaks was very small (∿0.001 gal/min) despite the fact that the exit length is longer than the other field-induced intergranular cracks studied, which had a flow rate of about 0.005 gal/min. In order to increase the flow rate from the second crack, corrosion products were removed from the crack with Dow Chemical DOWCON-1 solution. In addition, the surface was ground down about 4 mm (from top of weld crown) to open the crack exit length from 4 to 10 mm. The length of the crack at the inner surface is 13 mm. This crack does not show a uniform plume as do other intergranular cracks for comparable leak rates. The very small leak (0.001 gal/min) could barely be detected acoustically with a 375-kHz receiver, at ∿200 mm from the source. Initially, the crack may have been uncharacteristically tight since at that time the loading system was inadequate to stress the crack to typical reactor loads.

The crack was opened by loading the pipe to a level 50% greater than previous attempts (now approaching ∿7 ksi). As a result, it is now possible to reach flow rates above 0.01 gal/min. A comparison of

acoustic spectra of the two intergranular cracks for flow rates of 0.005 gal/min indicate virtually identical signals in the frequency range 200-400 kHz. Below 200 kHz, the difference in geometry between the two cracks apparently is reflected in a lower signal (~5 dB) for crack #2 (see Fig. 3). These data suggest that geometrical effects may be less significant at frequencies above 200 kHz and a correlation of leak rate with acoustic signals may be more reliable at higher frequencies.

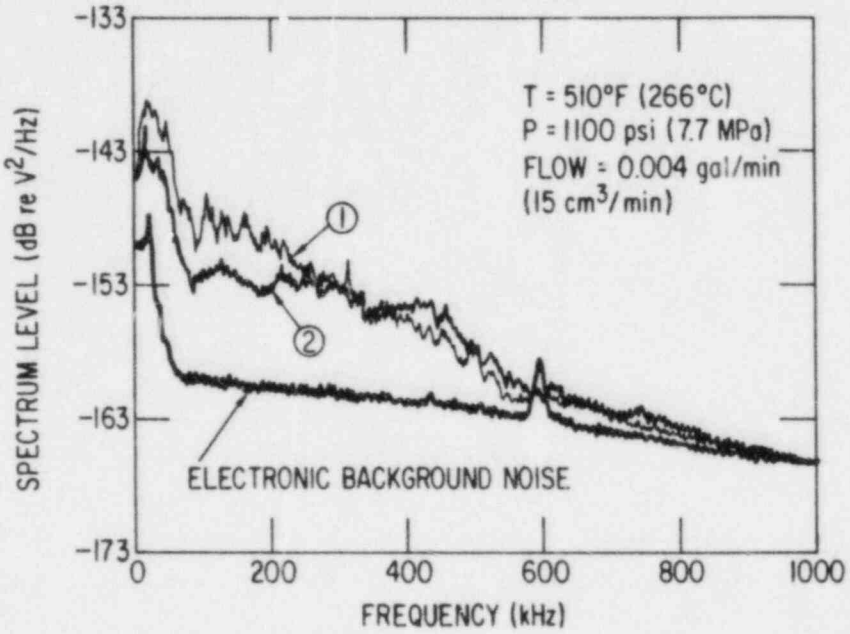

Fig. 3. Acoustic Leak Signal versus Frequency for Two IGSCC Leaks at the Same Flow Rate.

Acoustic emission noise generated by the smaller of the two thermal fatigue cracks (TFCs) was measured with the NBS transducer and compared to the noise generated by flow through an intergranular crack. The spectrum level is shown in Fig. 4 for each crack type. The spectra are similar in shape except that the noise level from the intergranular crack (at 400 kHz) is 5 dB or 1.8 times the level produced by the TFC even though the flow rate was only half of that of the TFC. This is consistent with previous observations that intergranular cracks produce more noise (at equivalent flow) than slits.

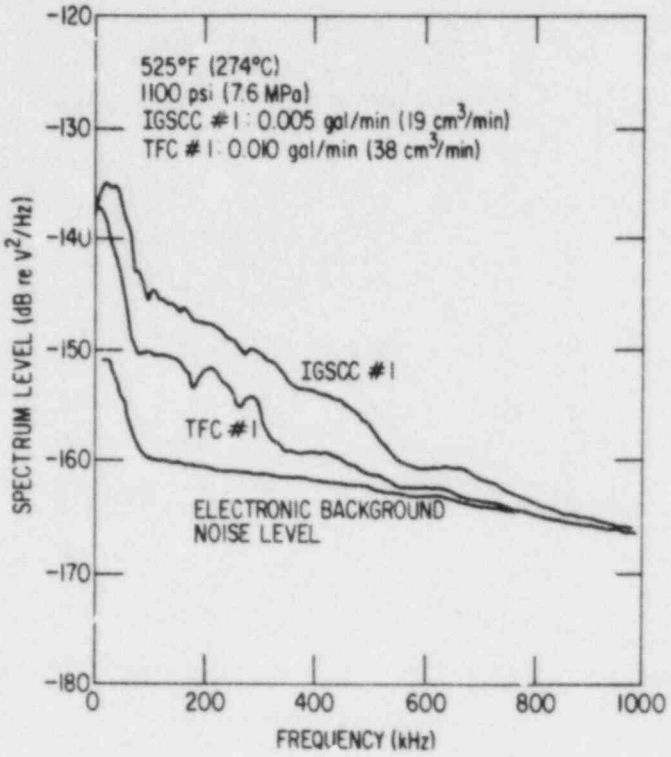

Fig. 4. Acoustic Signal versus Frequency for an Intergranular Crack at 0.005 gal/min (19 cm^3/min) and a Thermal Fatigue Crack at 0.010 gal/min (32 cm^3/min).

An important consideration for leak detection is the dependence of the acoustic emission signal on leak rate. This dependence may vary with frequency and depends on the mechanism that produces the sound. To obtain acoustic noise output as a function of leak rate and frequency, thermal fatigue crack #1 was stressed to 55,000 lbs and the leak signal measured in three frequency bands, viz., 30-40, 100-150, and 300-400 kHz. The curves in Fig. 5 reveal that the acoustic signals increase with flow rate and become less dependent on flow at higher frequency, and the variance in the data decreases at high frequencies. The acoustic emission output voltage for the three bands is given by the equations

$$V_m = 8400\ F^{1.3} \quad \text{(30-40 kHz)}, \tag{1}$$

$$V_m = 2100\ F^{1.2} \quad \text{(100-150 kHz)}, \tag{2}$$

$$V_m = 63\ F^{0.5} \quad \text{(300-400 kHz)}. \tag{3}$$

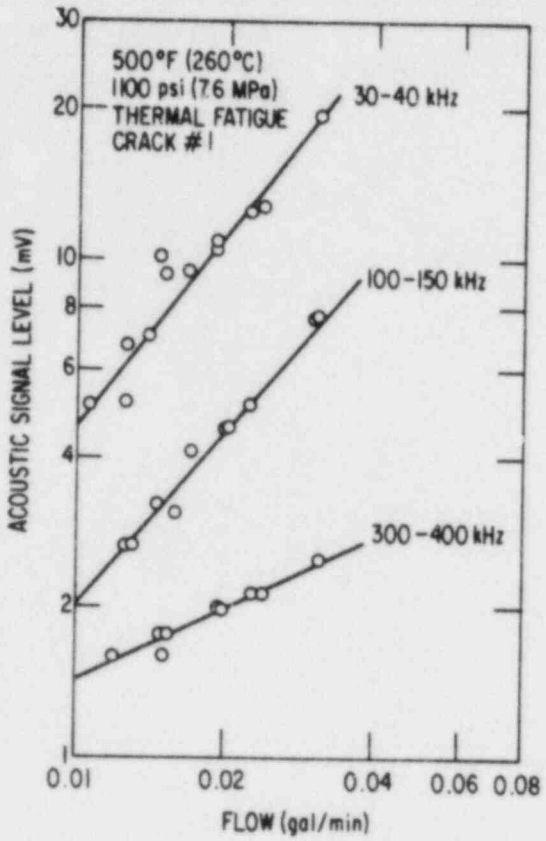

Fig. 5. Acoustic Signal vs Flow Rate for a Thermal Fatigue Crack at 500°F. Three frequency ranges are presented.

In Eqs. (1-3), V_m is given in microvolts and F is in gal/min. Because the variation of the acoustic output with flow rate depends on frequency, there may be more than one distinct noise-producing mechanism. At present, it is thought that almost all of the noise from the intergranular and transgranular cracks is due to steam flow. The NBS transducer is sensitive to airborne noise and this could be the cause of some of the signal enhancement at low frequencies. Further tests with the NBS transducer are planned to determine if the low-frequency sensitivity is distorting the results.

For intergranular crack #1, the leakage rate varied by more than an order of magnitude for loads in the range of 0 to 55,000 lbs applied to the bottom of the 10-in. Schedule 80 pipe directly under the crack. The results in Fig. 6 show that the acoustic output is not directly proportional to leak rate but follows the dependence given below (300-400 kHz):

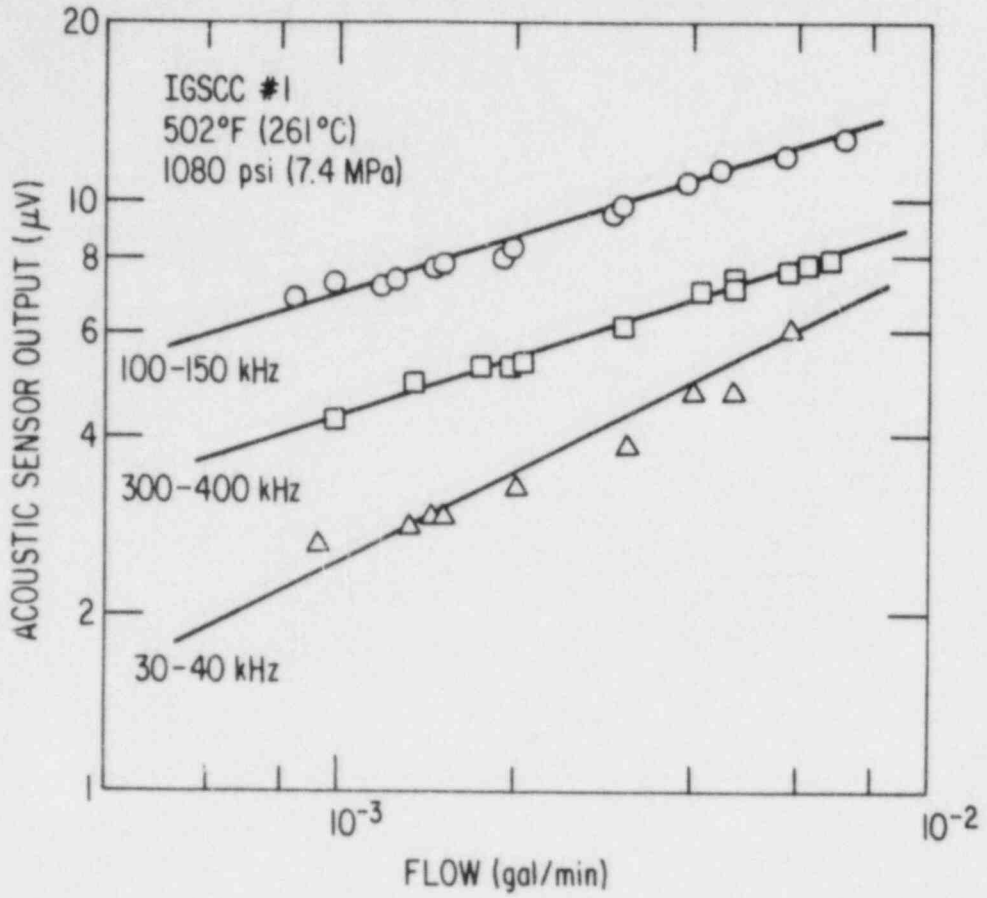

Fig. 6. Acoustic Leak Signal vs Flow Rate in Three Frequency Ranges for Intergranular Crack #1 at ~500°F.

$$V_m = 40.3\ F^{0.34} \qquad (0.001 < F < 0.01\ \text{gal/min}), \tag{4}$$

where V_m is in microvolts and F is in gal/min and the transducer is located 1 m from the crack. Extrapolation of this result to 1 gal/min indicates that 40 μV would be produced at 1 m. This should be compared to the ~45 μV of background noise (maximum for 300-400 kHz) that was measured at Watts Bar.

The acoustic noise output for intergranular crack #2 is shown in Fig. 7. The acoustic output is plotted as a function of flow rate for three frequency bands. The acoustic output in the 300-400 kHz band is given by the equation

$$V_m = 66.3\ F^{0.40} \qquad (0.001 \leq F < 0.01\ \text{gal/min}). \tag{5}$$

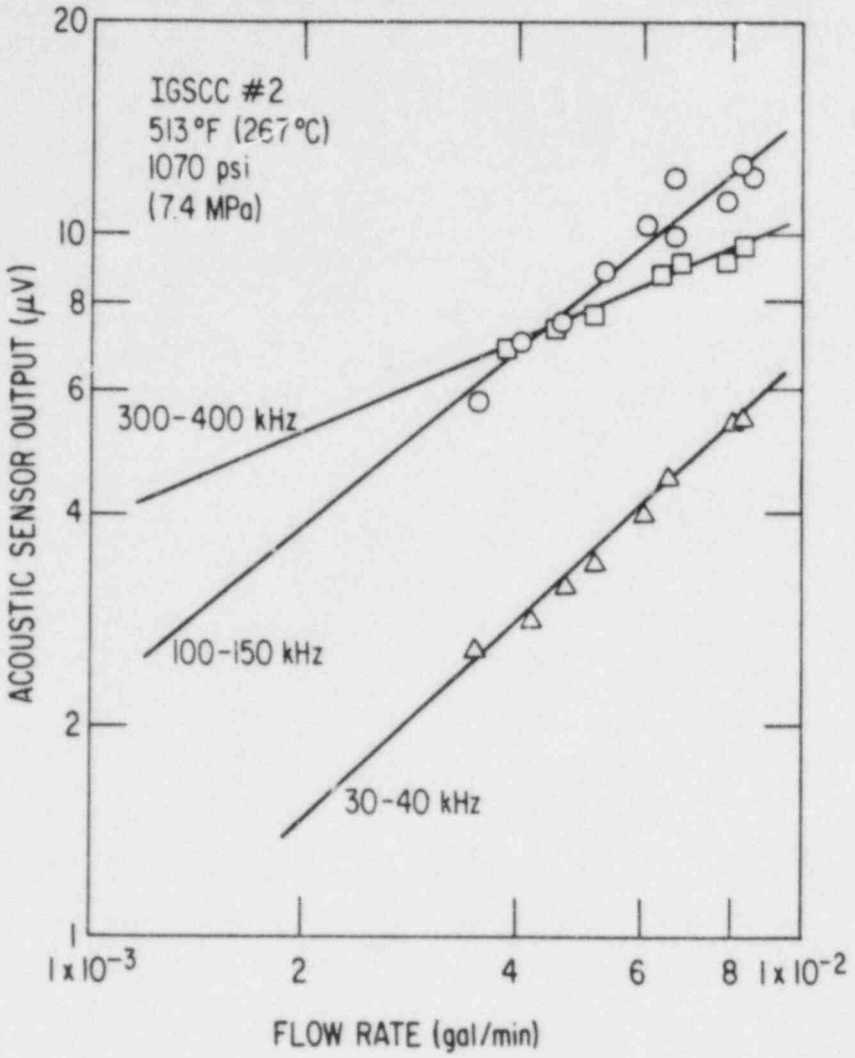

Fig. 7. Acoustic Leak Signal vs Flow Rate in Three Frequency Ranges for Intergranular Crack #2 at ~500°F.

The data correlation in the 300-400 kHz band is close to that obtained from intergranular crack #1. Only in this frequency regime is the acoustic leak noise comparable when extrapolated to 1 gal/min (within 4 dB for both leaks). At 30-40 and 100-150 kHz, the differences are 24 and 18.3 dB, respectively. Therefore, high-frequency acoustic noise measurement may offer a way to measure leak rate quantitatively (within limits) even from different-size cracks.

The noise produced by the two intergranular cracks was also characterized as a function of water pressure, which influences the leakage rate. The results of a variable-pressure test (992-1830 psi) on crack #1 at

a constant temperature (494°F) and load (0 psi) are shown in Fig. 8. The results are plotted as a function of flow and are similar to Figs. 6 and 7. At 300-400 kHz the flow rate dependence of the acoustic signal is given by

$$V_m = 22.4\ F^{0.21} \qquad (0.0001 < F < 0.001). \tag{6}$$

This result (combined with data from Figs. 6 and 7) indicates that acoustic output depends not only on flow rate but also on crack geometry. A comparison of Fig. 4 with Figs. 2 and 3 shows that the geometry effect is more important in the 30-40 kHz range than in the 300-400 kHz range.

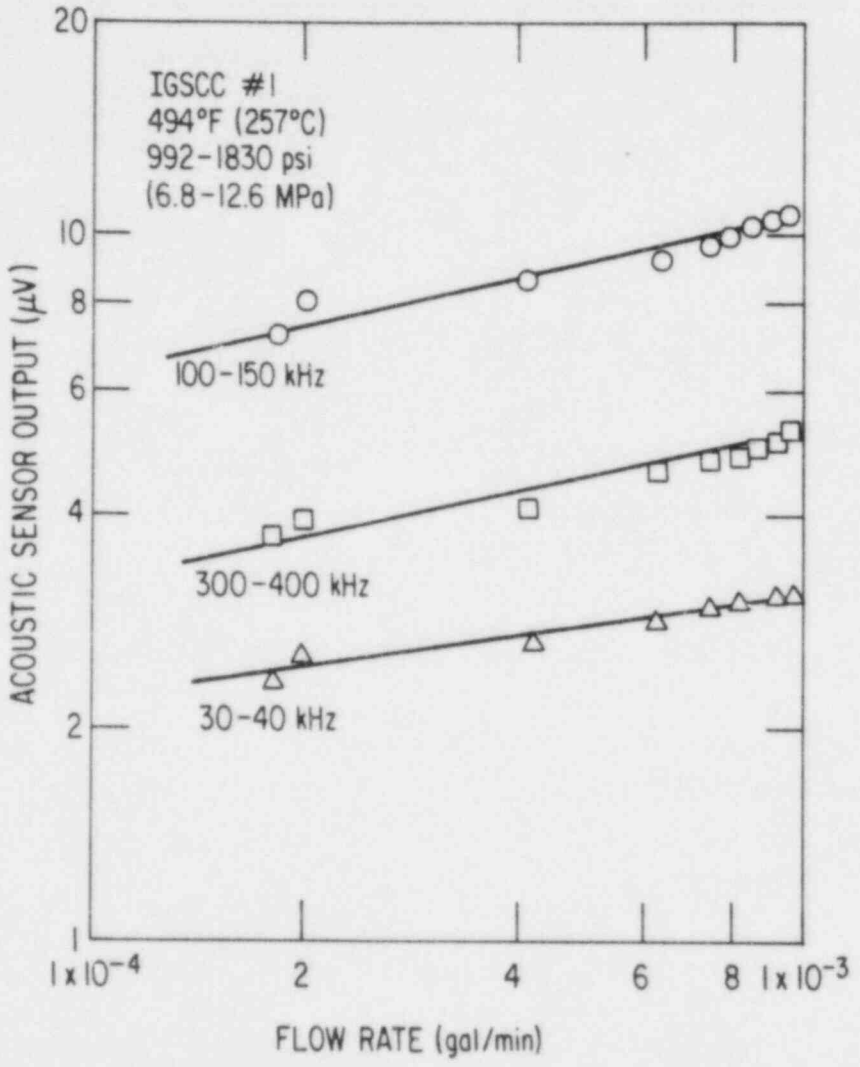

Fig. 8. Acoustic Leak Signal vs Flow Rate in Three Frequency Ranges for Intergranular Crack #1 at ~500°F. Leak rate was varied by increasing the system pressure.

Attenuation data have also been acquired for water-filled pipes in the frequency range of 200–400 kHz. Figure 9 shows the signal versus distance along the pipe run, which has a long section filled with water (indicated in the figure). The present ANL results are consistent with those in the literature.

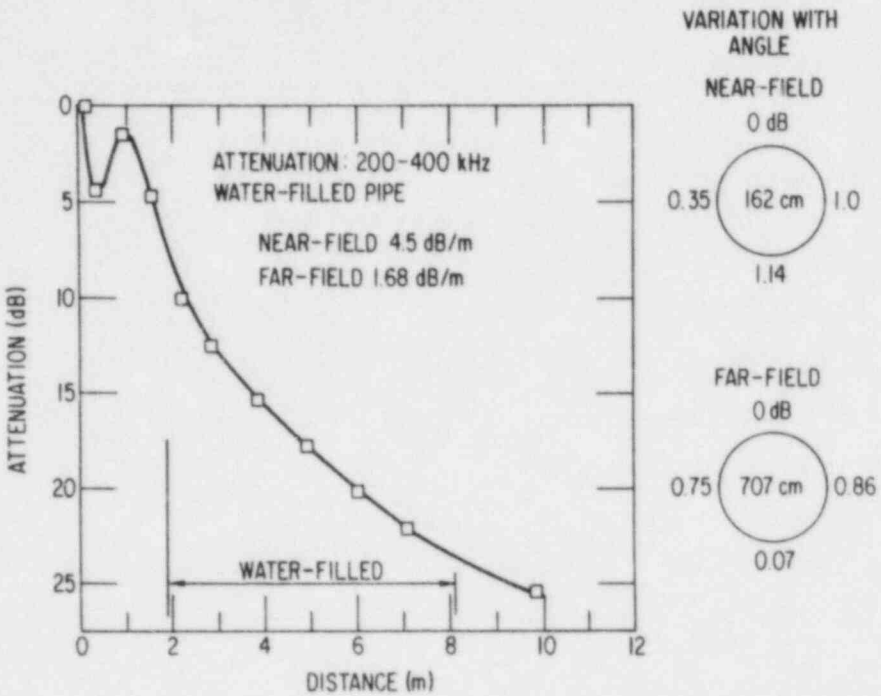

Fig. 9. Acoustic Signal (Attenuation) vs Distance Along a 10-in. Schedule 80 Pipe in the 200–400 kHz Frequency Range.

(4) Leak Location by Cross-Correlation Analysis

Cross-correlation is being evaluated as a means of achieving improved detection sensitivity for location of leaks even in the presence of background noise. The cross-correlation for time τ is defined as

$$R_{xy}(\tau) = \lim_{T\to\infty} \frac{1}{T} \int_0^T x(t)y(t+\tau)dt \ , \qquad (7)$$

where x(t) and y(t) are the input time domain signals over record length T. Incoherent background noise (such as flow noise) will average to approximately zero as the inverse of the number of data records averaged.

(5) Autocorrelation Analysis

More recently the propagation characteristics of leak-associated acoustic emissions (LAAEs) were investigated with correlation-processing techniques in an effort to establish a method for determining the location of a leak after its presence has been detected. The principles exploited are not unlike those employed in sonar, radar, and seismology for time delay estimation. The signal-processing approaches taken, however, are quite dissimilar. Radar and sonar applications, for example, typically require processing techniques that have been optimized for detection of a known signal that is buried in noise. The signal source, a transmitter, provides useful a priori information in this case. Where the source of the signal being processed is inaccessible, or unmeasurable as in the present case, the processing techniques become more dependent on assumptions, and therefore are more sensitive to processing errors. Signal sampling rate, filtering, and record length were carefully considered in an effort to minimize these errors. The results of our investigations of correlation-processing techniques are summarized below.

The autocorrelation function proved to be a potentially useful means of leak detection, as did its frequency-transform counterpart, the power spectrum. Figure 10 compares autocorrelation functions for a leak through an intergranular crack and a 2-mil (50-μm) slit, and background noise. Only the leak-related correlograms exhibit negative correlation peaks. Figure 11 shows autocorrelation functions for the leak recorded at increasing distances from the leak source (the numbered transducer positions are defined in Fig. 9 of Ref. 3). The leak characteristics are evident even at transducer position 8, approximately 6 m (18 ft) from the source.

The autocorrelation function was also useful as a tool for identifying LAAE propagation characteristics, an important prelude to cross-correlation analysis. The degree of symmetry of AE propagation in opposite directions was investigated, as were the effects of joints and other acoustic interfaces in the ANL test loop. Symmetrical transducer placements were investigated first. Autocorrelation plots were generated for data recorded with the same AET-375 transducer (3048) at two different sites,

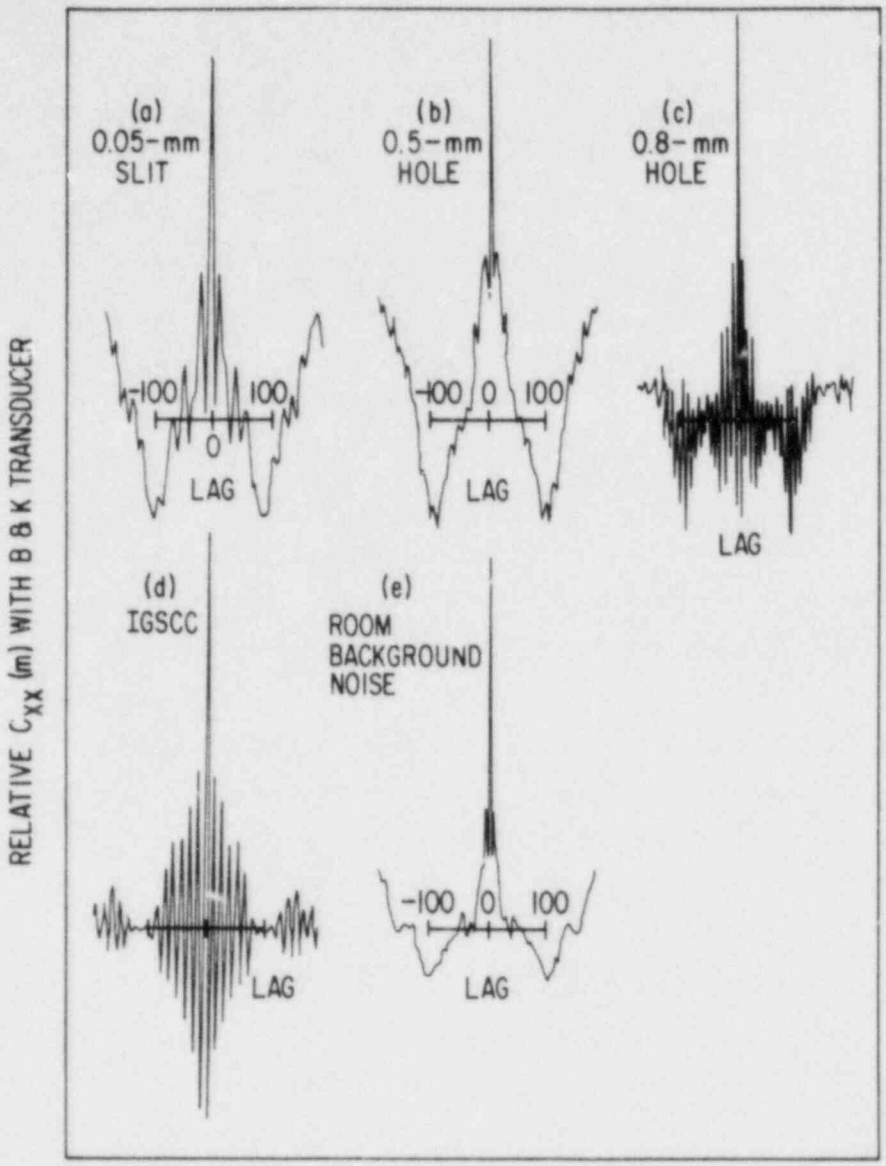

Fig. 10. Comparison of Autocorrelation Functions for Leaks through an Intergranular Crack, a 2-mil (50-μm) Slit, and Background Noise.

designated L and R, which were 1 m from the crack in opposite directions. Figure 12a shows the resulting autocorrelation functions. The data recorded at L yielded a slightly broader function than did the data recorded at R. For comparison, the experiment was repeated with a second AET-375 transducer, 3313 (Fig. 12b); the results proved to be reasonably independent of the transducer used, suggesting that the difference in the two functions is an artifact of the test facility. The only major difference in the transducer sites was that position L was located near the end of the pipe. The pipe

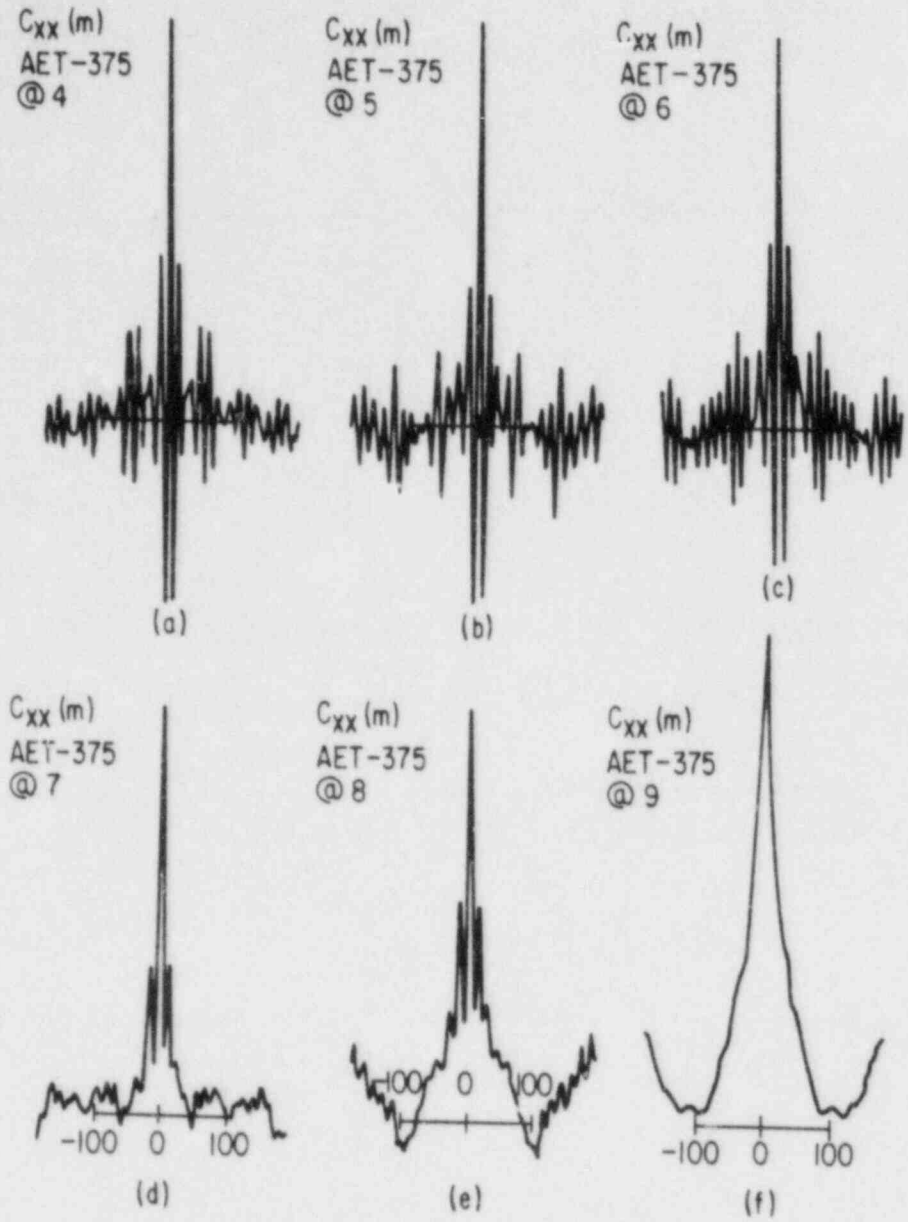

Fig. 11. Autocorrelation Functions for a Leak through an Intergranular Crack, Recorded at Increasing Distance from Source. Position 8 is 6 m away from source. Transducer positions are defined in Fig. 9b of Ref. 3.

ends had previously been partially covered with sound-absorbent material to minimize potential reflections which, if superimposed on the LAAEs, would result in additional (albeit smaller) peaks. The autocorrelation functions for the data recorded near the pipe ends indicate that the reflections have not been completely eliminated.

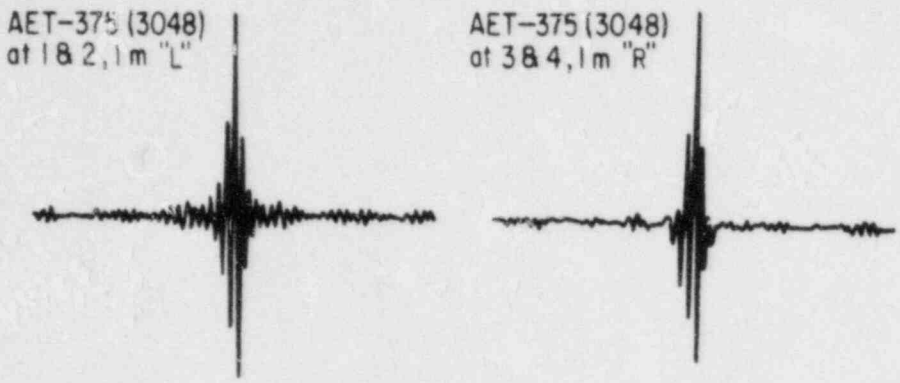

(a)

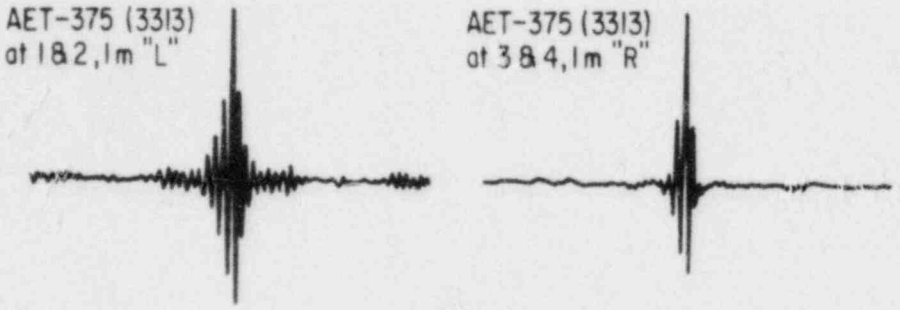

(b)

Fig. 12. (a) Autocorrelation Functions for a Leak through an Intergranular Crack, Obtained with AET-375 (3048) Transducer at Position L (1 m to left of leak) or Position R (1 m to right of leak). (b) Results Obtained at Same Positions with a Different Transducer.

(6) Acoustic Background Noise

a. Hatch Reactor

After ultrasonic testing revealed cracks in the Georgia Power Co. HATCH-1 BWR recirculation header, an ALD system was installed by Georgia Power and Nutech personnel. The transducer and waveguide are similar to those being evaluated at ANL for leak detection. Data from HATCH-1 can give an indication of background noise at the BWR recirculation header sweepolet weld. The HATCH system uses an AET 204A

miniature acoustic emission system and an AET AC375L sensor on a 1/2-in.-dia, 10-in.-long threaded stainless steel rod with a flat bottom. The waveguide is threaded through a mounting plate to hold it in direct contact with the pipe.

This system was reproduced and tested at ANL to establish its sensitivity and dynamic range. Figure 13 shows a plot of digital readout (proportional to the rms signal output) vs gain setting for the instrument. In order to approximate the HATCH-1 "B" conditions, ultrasonic waves were electronically generated on the pipe run to simulate background noise. For gains similar to that used in the field, the resulting dotted curve agrees well with the lower HATCH-B curve, which was obtained during reactor operation at 94% full power. At 100% full power, the HATCH-1 "B" readouts increased by about 20%; this is consistent with a model which assumes that the background noise is flow noise and thus increases as the cube of fluid velocity. If one assumes that the reactor power is proportional to fluid velocity and the rms signal is proportional to the acoustic noise level, the data appear reasonable.

The sensitivity of the system is demonstrated by the easily detected increase in signal when a 0.002 gal/min leak, at a distance of 0.5 m, is added to the simulated background noise (dash-dot line in Fig. 13). These results suggest that at the recirculation header of a BWR at full power, the acoustic background noise in the 200-400 kHz range is only a few dB above the electronic noise.

The dynamic range of the system is illustrated in Fig. 14, which shows a strip-chart recording (similar to those made at HATCH) of readout voltage vs time for leak rates of 0.002 to 0.006 gal/min. Under BWR operating conditions, the ANL system is saturated by the signal from a 0.006-gal/min leak through an intergranular crack at a distance of 0.5 m. A broadened dynamic range would clearly be desirable.

This example indicates the level of ALD capability that is currently available. There is no source discrimination (a large valve leak can register the same as a small crack leak) and there is no flow

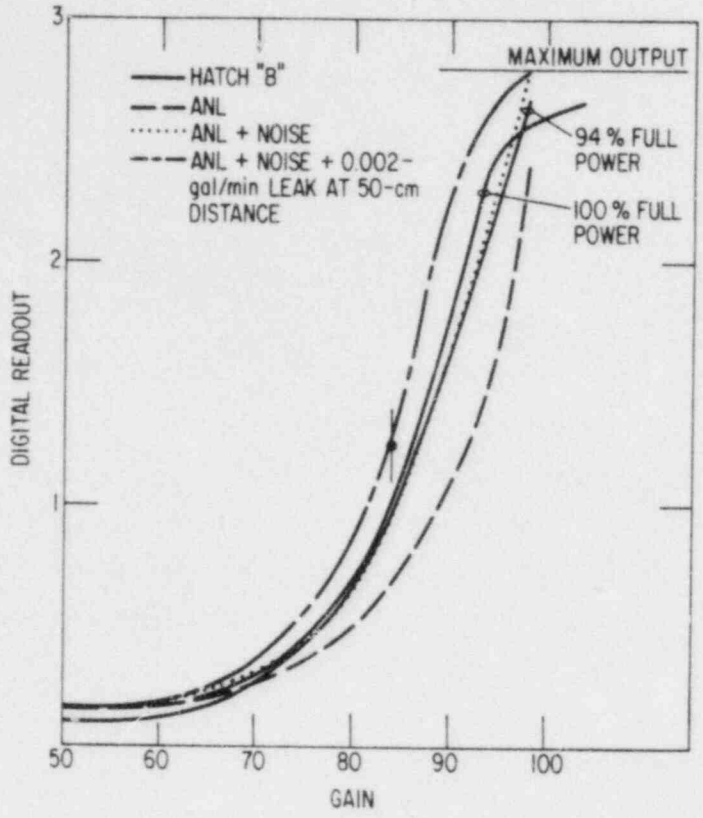

Fig. 13. Digital Readout vs Grain Setting of AET 204A Acoustic Emission System. ANL laboratory results are compared with data from the HATCH BWR monitoring system, with waveguide on header sweepolet. AET 375 transducers were used. The dark circle represents the setting used in the field.

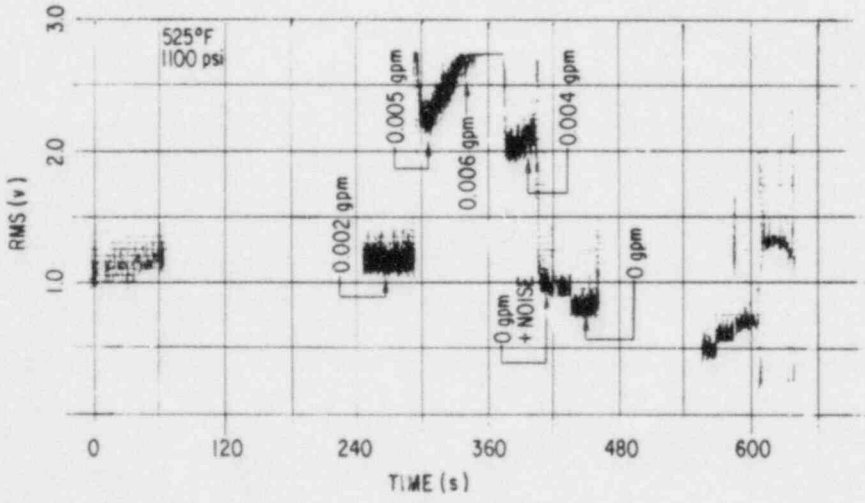

Fig. 14. Dynamic Sensitivity and Range of HATCH System (200-400 kHz).

rate information. A more sophisticated system is clearly needed to (a) eliminate false calls through improved leak location and characterization data, (b) quantify leak rate through analysis of rms time domain structure and spectral data, and (c) minimize the number of installed transducers in a complete system through reliable design and increased system sensitivity.

b. Field-implementable Acoustic Waveguide System

Two waveguide systems have been completed. Both designs use a 250-mm-long, 3-mm-dia waveguide rod of Type 304 SS. An AET 375 acoustic emission transducer is attached to the end of the waveguide rod with a spring washer. One system (Fig. 15) is a "quick-connect" type; the waveguide passes through a plate, which is strapped to the outside of the reflective insulation, and the round waveguide tip presses against the pipe surface via a spring-loading device (10-lb load). Gold foil serves as the couplant. In the other system, the waveguide tip passes through the insulation and is screwed through a plate that is strapped directly to the pipe outer surface. Silicon grease is used as a couplant. The force applied to the pipe at the waveguide tip is larger than with the spring-loaded system, but it cannot be measured as reliably. The analysis of preliminary results indicates that comparable acoustic signal levels can be reached with both designs. The systems are similar in sensitivity to the PNL waveguide and probe (which uses a magnet to hold the waveguide down and therefore is not appropriate for SS piping); an ∿6-dB signal is obtained at a distance of ∿1 m from a 0.005-gal/min leak.

c. Watts Bar

An acoustic emission transducer was mounted on the accumulator safety injection pipe (Fig. 16) (on the cold leg of loop 2) of the Watts Bar reactor No. 1. The transducer (AET 375 S/N 6002) was attached to the uninsulated 10-in. stainless steel pipe with a 10-in. waveguide probe assembly. An acoustic emission preamp with a gain of 40 dB was used to amplify the signal from the transducer and drive a 50 Ω cable. The cable terminated in the control room where another amplifier and signal recording equipment were located. Prior to installation, the transducer and waveguide

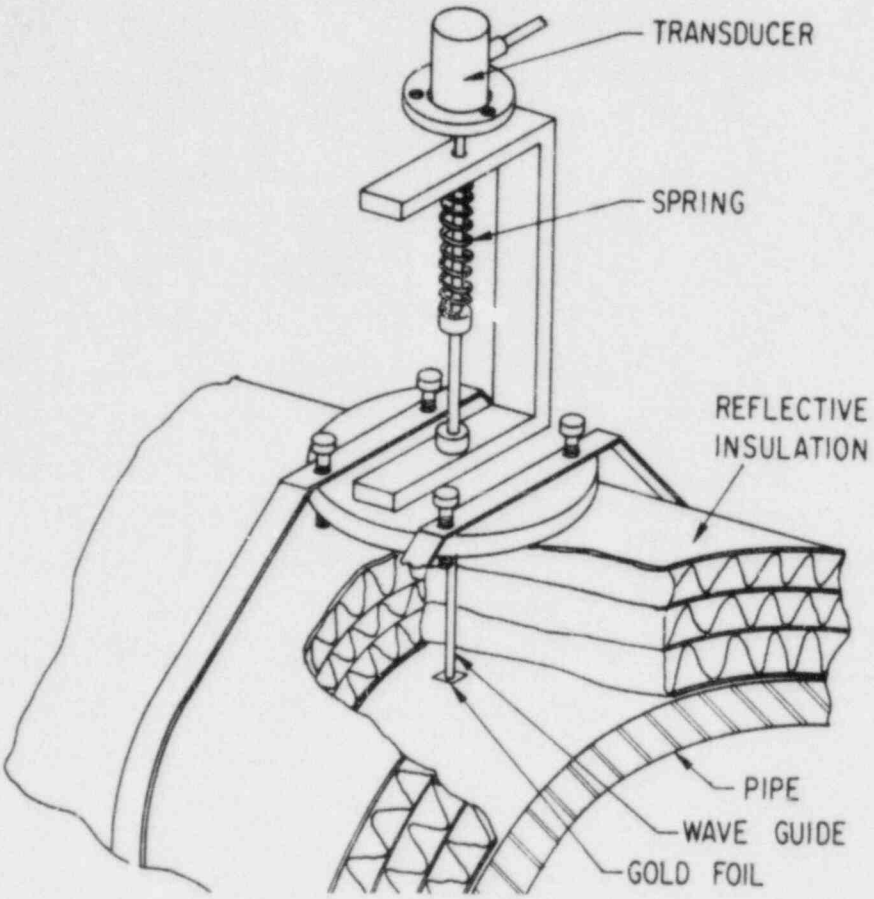

Fig. 15. Schematic of "Quick-Connect" Waveguide Attachment System.

assembly was calibrated in the laboratory against the NBS standard transducer. Results at five frequencies are shown in Table I. At 375 kHz the NBS transducer and the AET 375 have almost the same sensitivity. This is fortunate because it simplifies the comparison between the noise signals measured in the laboratory with the NBS transducer and the signals measured at Watts Bar with the AET 375.

After the transducer was installed at Watts Bar, its sensitivity was determined by the pencil lead impulse test. The transducer produced a signal that was 1.4 dB greater than that produced by the identical test in the laboratory.

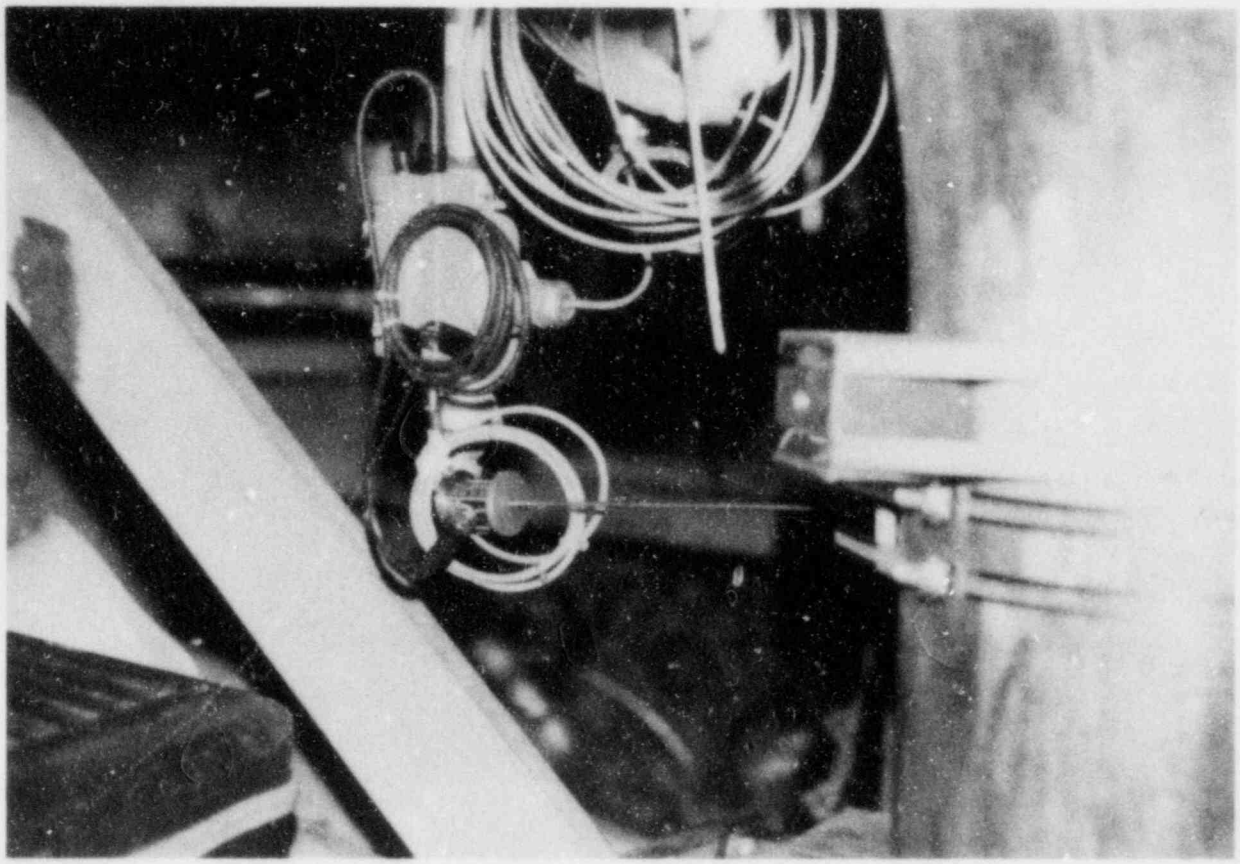

Fig. 16. Photograph Showing Acoustic Emission Transducer, Preamplifier and Waveguide System to Acoustically Monitor the Safety Injection Pipe at Watts Bar Reactor No. 1 during a Hot Functional Test.

Table I. Comparison of Acoustic Output from NBS and AET 375 Acoustic Emission Transducers

Frequency (kHz)	Transducer Output (dB)		
	NBS	AET 375	Difference
90	-131.0	-144.0	-6.0
150	-142.5	-159.0	-16.5
255	-151.0	-160.5	-9.5
320	-152.5	-160.0	-7.5
375	-154.5	-154.0	+0.5

Background noise was monitored before, during and after a hot flow test. Before and after the test, the water temperature and pressure were near ambient conditions (75-95°F at 30-75 psi); during the hot flow test the water temperature and pressure reached reactor operating conditions (557°F, 2235 psi). In general, the reactor noise level was greatest with all four reactor coolant pumps on and with the water at low temperature and pressure. Table II contains a summary of the noise levels measured at 200-400 kHz (primarily near 375 kHz) for various reactor conditions.

Table II. Acoustic Noise Level in the 200-400 kHz Frequency Band

Reactor Pump Status	Water Temperature, °F	Water Pressure, psi	Noise Level Transducer Output, μV	Notes
All pumps off	75	20	3.4	After installation
All pumps off	110	300	2.8	After installation
RCP-2 on	110	300	620	Hot flow test
All pumps on	350	400	390	Hot flow test
All pumps on	450	1200	83	Hot flow test
All pumps on	558	2235	92	Hot flow test
All pumps off	95	74	38	After hot flow test
All pumps off	94	29	32	After hot flow test

As can be seen from Table II, the background noise decreased with increasing system pressure. This has been observed in other reactor background noise tests and is probably related to decreased cavitation in the pumps. Still, the noise at full operating power was 28 dB over the quiescent state. Since the transducer was very close to the pump, the values for background noise reported here are probably near the maximum values that will be found on the

primary piping. They are also much higher than those present at the recirculation header of the Hatch reactor.

(7) Development of Breadboard-Type Leak Detector

(a) Coordination of Efforts with PNL

A meeting was held with PNL personnel to coordinate the current GARD/ANL and PNL efforts on this program. The PNL program is directed at crack growth monitoring in nuclear piping. The PNL system is further along in its development than the GARD/ANL leak detector; a prototype of the PNL system is to be installed on the Watts Bar reactor. Signal bandwidth and amplitude requirements of the two systems, as well as overall system architecture, were discussed. Signal processing is approached differently in the two systems because acoustic emissions from leaks are continuous in nature, whereas burst- or event-type acoustic emission is associated with crack propagation. The benefits of a combined system, however, are significant. An overall reduction in hardware (transducers and preamplifiers) coupled with a corresponding reduction in installation complexity would reduce the system cost, and would be looked upon favorably by the nuclear industry. Therefore, the needs of these two systems will be reviewed from time to time to assess whether changes have occurred that will make the use of common system elements more feasible than it now appears.

PNL personnel plan to modify their system to allow continuous rms data to be taken. At present, there is an overlap in the frequency windows chosen for leak detection and crack growth monitoring. It may be possible to use the same transducer-waveguide system.

(b) Hardware

The system configuration for the breadboard system has been established. The breadboard system, as originally proposed,

utilized a local microcomputer to control data acquisition and to provide operator interface; communication with a minicomputer at GARD was to be accomplished via two modems and a dedicated telephone line. All he data analysis routines would be resident in the minicomputer and would be called remotely from the laboratory satellite system. Similarly, the resultant analyses would be transmitted to the satellite for display and stored in the minicomputer's archives. There might be some latency related to data transmission time, but the on-line data analysis principles would be adequately evaluated with such a breadboard system.

An alternative that was subsequently considered was the use of a transportable minicomputer with an appropriate front end. This avoids the need for telephone lines and modems and their associated costs along with the efforts associated with establishing a remote inter-computer interface. Currently available at GARD is a Motorola M68000 which was originally thought to be adequate for this application. Such a system would certainly have sufficient computational power to meet the needs of this program; however, software-generating capability is currently limited to a 68000 assembler, which would greatly increase the efforts required to generate the analysis software (i.e., FFT and correlation routines). Fortran could not be made available, owing to licensing restrictions.

An investigation of other available minicomputers narrowed the field to the three candidates listed in Table III. They all have comparable hardware capabilities: 256 or 512 kilobytes of RAM and 20-33 megabytes of Winchester disk storage with tape or floppy-disk backup. The Dual and AIM Technology systems utilize the Motorola 68000 CPU, whereas the DEC system has the latest proprietary LSI CPU, which probably has similar or greater capabilities. The Unix operating system used by AIM and Dual is more versatile and "user-friendly" than DEC's RT-11. Both operating systems support the Fortran compilers needed for this project. The greater flexibility of the Unix system, however, provides for easier integration of Fortran-callable routines (not necessarily written in Fortran), which will be helpful in controlling the data acquisition hardware and handling the arrays of data thereby generated. The three Fortran compilers/assemblers were comparable in cost. The DEC system offered an optional Signal

Table III. Comparison of Minicomputer Capabilities

	Computer Systems		
	DEC Micro II	AIM Technology	Dual 83/20
CPU	DEC LSI-11 (latest version)	Motorola 68000	Motorola 68000
Operating System	RT-11	UNIX	UNIX
Fortran Software Fee	$1,000	$1,200	$600
External Interface	Q-Bus adapter	Multibus adapter	S-100 interface
RAM (kilobytes)	256	512	512
Mass Storage	20-megabyte Winchester; 1-megabyte floppy disk	33-megabyte Winchester; ½-in. Mag. Tape	20-megabyte Winchester; 1-megabyte floppy disk
Mainframe	DEC Q-Bus	Multibus	S-100 Bus
Approximate Cost	$10,000	$17,000	$13,300
Availability	July-Aug. 1983	30 Days ARO	15 Days ARO
Customer Efforts Needed to Achieve System Operation	None	Customer Responsible for System Integration & Checkout	None

Technology package for data analysis at a cost of $6,000. However, public-domain analysis programs are offered by IEEE and others at minimal cost. The Q-bus employed by DEC restricts the user, to some degree, to DEC-supplied hardware, whereas the Multibus and S-100 bus systems are well supported by multiple sources of compatible hardware boards and interfaces. AIM Technology, primarily a board supplier, provides a system which requires

customer integration and checkout. The others are supplied ready-to-go with a minimum of inter-chassis cable connection. Although any of these three systems would meet the needs of this project, the attractive cost of the DEC system is outweighed by its unavailability until midyear. The Dual system was selected because it provides slight advantages in cost and delivery time, and a significant advantage in that customer effort is not required to integrate the system.

An additional implementation change involved purchasing an off-the-shelf transient digitizer in lieu of fabricating one. The unit that was first considered was the LeCroy TR 8837, a two-channel digitizer that could operate at sampling rates of up to 25 MHz in the dual-channel mode (50-MHz single channel). It was programmable in terms of sampling frequency and pretrigger mode and had an internal 16 K sample memory. The TR 8837 has since been superseded by a single-channel unit. This has a higher maximum sampling rate (32 MHz), and two or more units can be slaved together in a multiple-channel mode. Interestingly, two of the new units (TR 8837F) are lower in cost than the original dual-channel TR 8837.

All of the LeCroy units are designed for operation in CAMAC enclosures. The use of a crate, crate controller, and S-100 interface will be required. The digitizer and its supporting hardware can be more than adequately covered by the original estimated costs of materials and labor to develop a custom two-channel digitizer. A nine-slot minicrate is proposed, which will provide ample space for all the above-mentioned hardware along with the necessary signal-conditioning hardware (filters, preamps, etc.) to interface transducers with the digitizers. This will result in a neat, workable package for the breadboard system.

(c) Software

The software development for this program is divided into two primary tasks. The first is the evaluation of available data analysis programs to determine their applicability. The available programs are typically in the public domain and are published by IEEE and

other sources. The second task is the generation of required analysis routines that are not currently available, along with the mainline programs needed for leak detection. The mainline programs will utilize the analysis routines (both those obtained from other sources and those generated here) as subroutines for flaw detection, location, and characterization. The efforts on this task began when the Dual 83/20 computer system was received. Initial efforts were directed to the evaluation of programs that are currently available from IEEE. Routines were extracted from five source program listings and were modified for this application by (a) restructuring them into subroutine format, (b) redimensioning real and complex arrays to fit the present application, and (c) manipulating the data arrays to attain compatibility with each author's array format. The subroutines evaluated to date are described in Table IV. Included are FFT, correlation, digital filtering, and sample rate conversion routines, all of which may be useful in this project. Also included are some plotting routines which will be of interim value.

Table IV. Summary of Software Routines for Acoustic Signal Analysis

Subroutine	Description
FFT	Implements simple decimation-in-time algorithm which computes Fourier coefficients for a complex input sequence.
CORR	Uses classic biased correlation estimator and is the most efficient approach in performing the actual correlation.
FDESIGN	A finite impulse response (FIR) filter design program.
FCONVERT	Performs sampling rate conversion (i.e., interpolation or decimation) of a sampled data sequence.

(8) Calibration Procedures

Three calibration procedures are being considered for checking transducer-waveguide systems after field installation. They are the pencil-lead-breaking method, the gas jet method, and electronic pulsing. The first two of these techniques were examined during the current reporting period. In the lead-breaking technique, the lead (0.5-mm dia) of a Pentel mechanical pencil is extended 5 mm beyond the end of the pencil body and is broken by pressing the pencil lead against the pipe at an angle of 30° to the pipe. (If this technique is demonstrated to be useful, fixtures will be fabricated to standardize the procedure.) The breaking of the lead was detected by an AET-375 transducer mounted on a waveguide at a distance of 0.2 m from the pipe surface. Excellent reproducibility of the captured acoustic transient signal was evident from four successive breaks in which the digitized and stored transient pulses were compared. This technique may be useful as a convenient and rapid way to check the ALD system after installation. The method would not be applicable, however, to remote in-situ calibration. This could be carried out by the gas jet technique or by electronic pulsing.

In current work on the gas jet technique, a jet of nitrogen gas from the 1.5-mm-dia exit hole of a Swagelok fitting was directed normal to the pipe surface from a distance of 6 mm. An rms signal (50 kHz to 1 MHz) with a magnitude 4 times that of electronic background was detected at a distance of 1 m. The broadband IQI-501 transducer was employed to obtain information on frequency spectra. The acoustic spectrum from the gas jet shows greater frequency dependence than does the spectrum from a leak through an intergranular crack. Relatively more signal at lower frequencies is present in the gas jet spectrum. Furthermore, most of the detected gas-jet acoustic signal is in the form of surface waves; this is not the case for crack leaks. It has also been determined that the acoustic signal is relatively insensitive to the exact height of the gas jet above the surface for heights of about 10 mm. This calibration technique has the advantage of providing a reproducible, continuous acoustic signal that is somewhat representative of an actual leak. This technique appears to be well suited to remote calibration. Its chief disadvantages are the

inconvenience associated with setting up the system and problems associated with the presence of insulation.

The sending of electronic pulses to a calibrating transducer is also under investigation as a technique for remote calibration. In this technique an electronic signal is used to pulse a transducer (on a waveguide) which then generates an acoustic signal in the pipe. In this technique the transducers used to generate the calibration signal would not be used for receiving acoustic leak signals. A method would have to be established for distinguishing anomalous behavior of receivers from anomalous behavior of pulsers. The electronic pulsing technique offers a relatively simple procedure for continuous in-situ monitoring of an ALD system. The disadvantage is the need for additional transducers on the pipe and possible problems with coupling the waveguides of the transmitting transducers to the pipe.

The data now acquired in this program allow us to make some estimates of the sensitivity of an acoustic leak detection system in a field environment. Figure 17 shows the acoustic signal intensity (in a 300-400 kHz window) versus distance along a 10-in. schedule 80 pipe for 0.01, 0.1 and 2 gal/min flow rates. The acoustic signal versus flow rate data at values >0.01 gal/min were determined from an extrapolation of low-flow data from two intergranular cracks. The shading represents the difference in extrapolation from the two sets of curves. The lower curve was obtained by assuming a $(\text{flow})^{0.32}$ dependence for the acoustic signal, which is consistent with Battelle Columbus data on graphite-wool-grown IGSCC in 12-in. pipes. The BCL data show a $(\text{flow})^{0.28}$ dependence over four orders of magnitude in flow rate (private communication, Collier of BCL). Also shown are upper and lower estimates for background noise data. The upper line was derived from the Watts Bar hot functional test. The lower level is a combination of inferred background noise from the Hatch installation and data from KWU (Fischer, private communication) indicating a factor of 10 variation in background noise for the PWR they monitored. As can be seen at a distance of 3 m (10 feet), leaks as small as 0.01 gal/min could be detected in areas of low background noise, whereas leaks on the order of 2 gal/min may be detectable in areas with very high background noise. Leaks as small as 0.1 gal/min may be detectable at the source even with very high

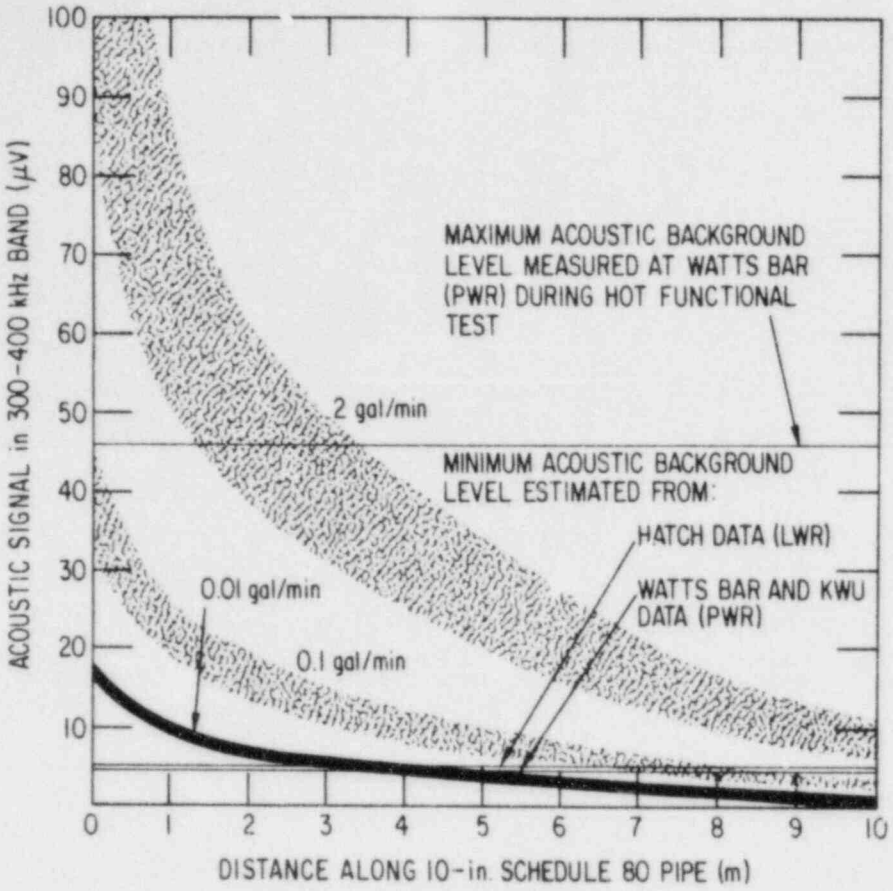

Fig. 17. Acoustic Leak Signal Intensity versus Distance Along a 10-in. Schedule 80 Pipe for Various Flow Rates. The shading represents uncertainties in extrapolating data from low to high flow rates.

acoustic background levels. Acoustic data were taken 1 m from the leak. Beyond that an attenuation of 2 dB/m for the 300-400 kHz bandwidth and an insertion loss of 5 dB for the first meter between the leak and sensor were assumed.

(9) Moisture-sensitive Tape

A system to test the sensitivity of moisture-sensitive tape was constructed in the laboratory. It consists of a 10-in. Schedule 80 pipe section, 1 m in length, heated to 500°F and covered with reflective insulation. A small (1/4-in.-dia) hole was drilled in the insulation (as per installation instructions for the moisture-sensitive tape) so water could drop onto the tape. The sensor was mounted on the bottom of the pipe and the steam leak was positioned on the top of the pipe directly over the tape for the initial tests. Steam was introduced between the pipe and the

insulation with a 1/8-in.-dia copper tube. Physically, the leak was 0.3 m away from the tape.

This configuration for the tape and the leak is similar to what one would use in a plant to monitor welds for leakage. According to the supplier, 3 to 4 inches of tape on a stainless carrier strap would be placed under each weld to be monitored, with a tube to direct the water to the tape. Up to 700 welds can be monitored with presently available systems.

Two types of moisture-sensitive tapes were supplied with the instrumentation. Sensor A is an improved sensor tape that is less susceptible to false alarms caused by external sources of water. Sensor B is an older type of tape which is more sensitive to water. At a temperature of 470°F and a 0.05 gal/min flow of water/steam through the leak, sensor B responded to the leak within 8.6 minutes. Sensor A, under nearly identical conditions (440°F, 0.05 gal/min) responded after 28.5 minutes. Sensor B took about 5 minutes to return to normal resistance when dried with a heat gun after the test. Sensor A did not dry out completely after 20 minutes with the heat gun. The sensor will probably have to be baked in an oven at 200°F for several hours to return the resistance to the as-received condition.

(10) Summary - Acoustic Leak Detection

Acoustic characteristics of leaking IGSCC were established as well as the effect of waveguide geometry and insulation on leak detection. Cross correlation techniques were demonstrated for locating leaking IGSCC and distinguishing leak type. A frequency range (∿200-400 kHz) for optimizing signal-to-noise ratio for leak detection was established. A waveguide/transducer system for field use was assessed and tested under laboratory conditions as well as during a hot functional test. The HATCH BWR acoustic leak detection system was simulated to obtain an estimate of background noise and the sensitivity of the HATCH system. Background data was obtained during a Watts Bar (PWR) hot functional test. The minimum detectable leak rate for laboratory conditions was established and estimated for field conditions (0.01 to 2 gal/min, depending on background noise). Calibration procedures for AE monitoring have been evaluated. A moisture-

sensitive tape system was acquired and evaluation was initiated. The breadboard acoustic leak detection system (GARD) is nearly complete.

b. Ultrasonic Nondestructive Evaluation

(1) Objectives

This task involves examining the possibility of using ultrasonic wave scattering patterns to discriminate between IGSCC and geometrical reflectors. The potential use of nontraditional methods to improve flaw detection in centrifugally cast stainless steel (CCSS) and weld metal and to investigate special NDE problems, such as inspection of weld overlay, will be explored.

(2) Distinguishing IGSCC from Geometrical Reflectors

Because intergranular cracks have an irregular and generally branched character, they may produce a broader scattering pattern than a geometrical reflector. The dependence of echo amplitude on the angle of incidence to the reflector surface could then be used to help distinguish cracks from geometrical reflectors. Whether this idea could be useful under field conditions needs to be established.

Seven cracks and four geometrical reflectors in Type 304 SS pipe specimens were examined with 2.25-MHz, 45° shear waves in a pulse-echo mode. The amplitude was plotted against the skew angle θ by peaking the signal for each θ. The change in signal with θ was sharper for the geometrical reflectors than for the cracks. This difference was quantified by measuring the "full width at 3/4 maximum signal" (FW3/4M) for the curves. Table V describes the specimens and gives the results. For the cracks, the FW3/4M values ranged from 50° to 70°; for the geometrical reflectors, the values ranged from 26° to 38°. These results represent only a limited number of samples, and only sparse data have been acquired from metallurgical reflectors, but the approach appears promising at this time. If the type of information discussed here can be acquired in the field (perhaps by a multielement probe), the chance of distinguishing cracks from geometrical reflectors may be improved under some circumstances.

Table V. FW3/4M Values Obtained[a] for Cracks and Geometrical Reflectors in Type 304 SS Pipe Specimens

Reflector	FW3/4M (deg)
Geometrical Reflectors	
End of pipe	38
2-mm-deep EDM notch	34
Weld root in 12-in. pipe	26
Weld root in 20-in. pipe	30
IGSCC	
Graphite-wool-grown axial cracks in 12-in. pipe[b]	60,70,64,64
Graphite-wool-grown circumferential cracks in 12-in. pipe[b]	51,50
Field-induced circumferential crack in 10-in. pipe	70

[a] 2.25-MHz, 45° shear waves in pulse-echo mode.

[b] Provided by EPRI's Nondestructive Evaluation Center.

As a result of this effort a probe has been designed that can be used with a multiscanner to provide the data needed for IGSCC discrimination. The problems associated with designing such a multielement probe are 1) the need for uniform coupling of many wedges and 2) the need for a small enough probe size to avoid interference with the weld crown. A 7-crystal probe was found to be suitable for use on large (28-in.-dia) pipes. The design of the "multiple element skew angle" (MESA) probe is indicated in Fig. 18.

The initial design, aimed toward inspection of 28-in. (0.7-m)-dia pipes, uses seven interlocking miniature 45°-angle shear-wave probes in a rubber "frame" (which provides enough flexibility to ensure uniform coupling with the pipe surface), with a multiscanner and individual gain control for each channel. The gain for each element can be adjusted to

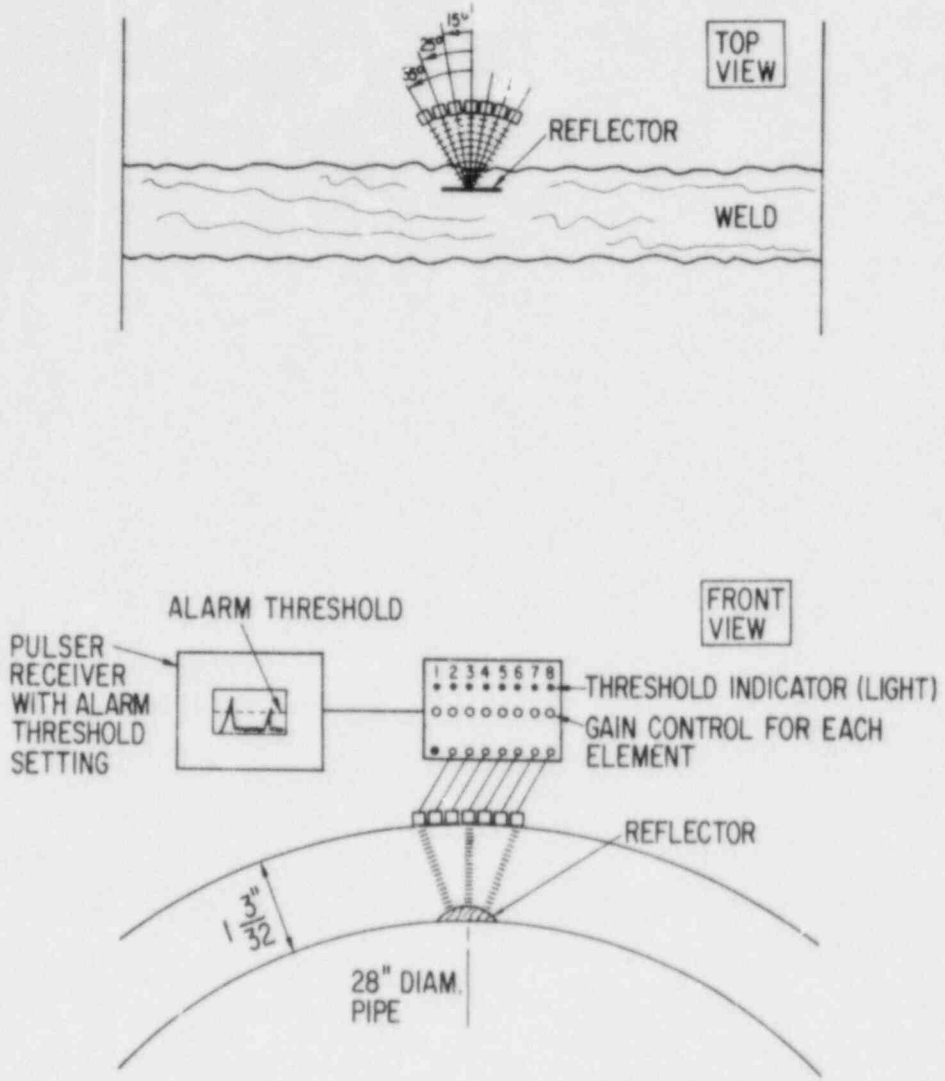

Fig. 18. Schematic Representation of Multielement Skew Angle (MESA) Probe for Discriminating Cracks from Geometric Reflectors.

compensate for the degree of reduction in amplitude with skew angle that characterizes geometrical reflectors. After the gain of the pulser-receiver is adjusted to the calibrated level, IGSCC can in principle be identified by the presence of above-threshold echo signals for the transducers positioned at large skew angles; the signals generated at large skew angles by a geometrical reflector will fall below the threshold.

A "MESA" probe has been fabricated by Magnaflux. This probe has seven elements, each approximately 3/16-in. wide, and operates at 2.25 MHz. The probe is currently being evaluated under laboratory conditions, with field-induced cracks in large-diameter pipes from the Nine-Mile Point Nuclear Reactor.

(3) NDE of Centrifugally Cast Stainless Steel

Cast stainless steel (CSS), because of its coarse grain structure, presents a major difficulty in the ultrasonic inspection of reactor components such as piping in pressurized water reactors. CSS samples were examined at frequencies as low as 0.5 MHz to identify optimal ultrasonic testing conditions for this material. Both isotropic and anisotropic samples were tested (the latter are transversely isotropic, owing to the presence of long columnar grains).

Two types of CCSS samples have been evaluated. The samples are both from cast Type 304 SS piping (~27-in. dia), but they have different microstructures. Sample A has equiaxed 1 to 2-mm-dia grains and Sample B has large columnar grains ($\gtrsim$10 mm long and ~2 mm wide). Experiments were performed to determine the degree of texturing in these samples. If the anisotropic CCSS resembled SS weld metal during ultrasonic inspection, then techniques developed for one material would also be applicable to the other. In addition, if the two specimens had different textures, they could be used to determine whether the inspectability of CSS is related to the degree of anisotropy in the sample.

Angle beam testing in CCSS with columnar grains often is carried out with 1-MHz longitudinal waves that propagate at approximately 45° to the long axis of the columnar grains because a focusing effect occurs at this propagation angle for longitudinal (but not shear) waves. Also, grain boundary scattering is less than for shear waves at the same wave length. For stress corrosion cracks in isotropic stainless steel, the problem reduces to one of increasing the ratio of wavelength to grain size. A 65-mm-thick block of isotropic CSS (grain size of 1-2 mm) containing a 10-mm-deep EDM notch and a 6-mm-dia side-drilled hole was used to compare

the effectiveness of shear and longitudinal waves. The sample is shown in Fig. 19. To match the 6-mm wavelength of 1-MHz longitudinal waves, a shear wave frequency of 0.5 MHz was used. Figure 20 shows typical radio frequency signals obtained from the side-drilled hole (upper traces) and notch (lower traces) with normal-incidence shear waves (left) from a Panametrics 0.5-MHz, 1-in.-dia transducer and normal-incidence longitudinal waves (right) from a Panametrics 1-MHz, 1/2-in.-dia transducer; . e transducers were placed on the "slope" of the sample to generate the equivalent of 45°-angle beams. The results indicate that for comparable wavelengchs, shear and longitudinal waves generate comparable signals for a side-drilled hole. However, for the notch, the reflection generated by the 0.5-MHz shear waves is much stronger than that for the 1-MHz longitudinal waves. The loss of signal for the longit:dinal waves is the result of mode conversion at the notch. These results, although limited, suggest that angle beam testing at 0.5 MHz may be the choice for inspecting isotropic CCSS with grain sizes in the range of 1 to 2 mm. The sensitivity for these lower frequency shear waves is, of course, lower because of the long wavelengths; therefore, only relatively large flaws will be detectable. Note that the polarization of the shear wave can be varied by rotating the transducer. As one might expect for isotropic CCSS, varying the polarization had relatively little effect on reflected echoes.

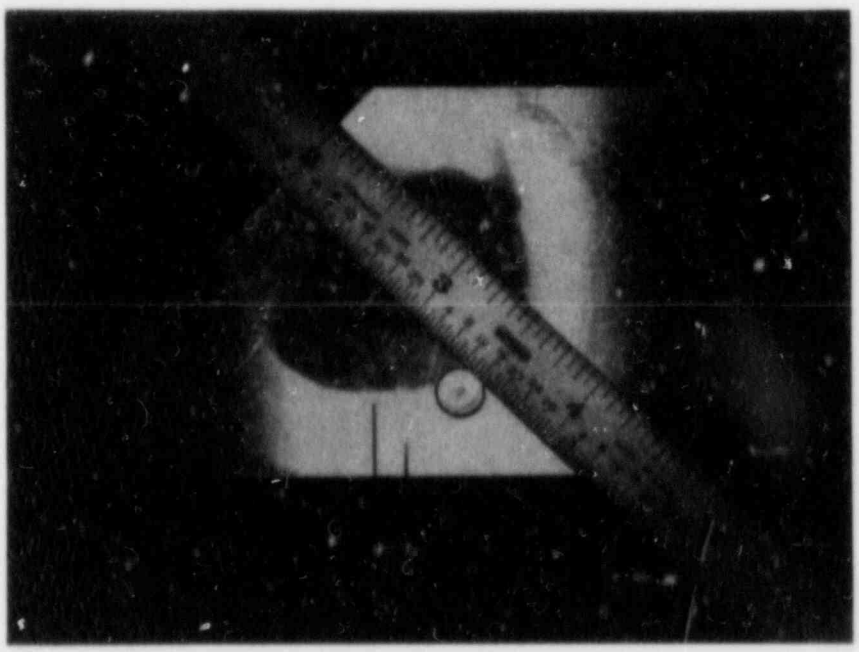

Fig. 19. Photograph of Isotropic CCSS Sample (Grain Diameter of 1-2 mm) Containing EDM Notch and 6-mm-dia Side-drilled Hole.

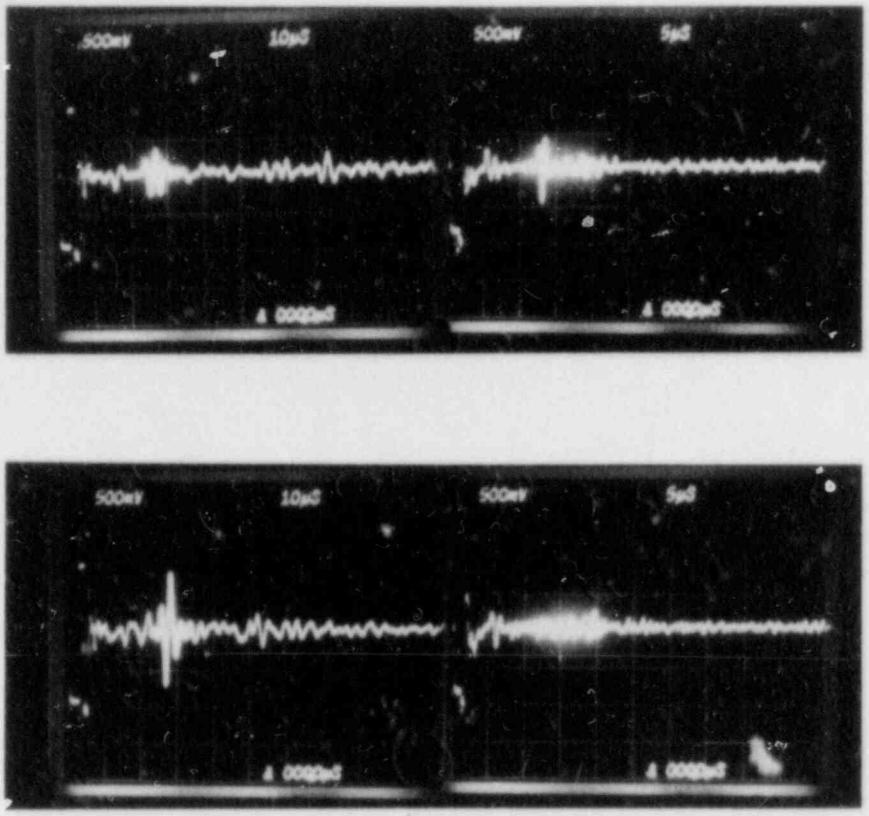

Fig. 20. Radio Frequency Echo Signals from Isotropic CCSS Sample of Fig. 19. Signals from (top) side-drilled hole and (bottom) EDM notch were obtained with (left) 0.5-MHz shear waves and (right) 1.0-MHz longitudinal waves. Transducers were placed on the sloping side of the sample to simulate 45°-angle beams.

The effect of lowering the frequency of the shear waves from 1 to 0.5 MHz can be seen in Fig. 21. Here, 45° shear waves were generated with Panametrics 1-in.-dia transducers on plastic wedges. For a 25-mm-thick wrought plate, comparable signals were obtained from the corner at both frequencies with a "1-V" acoustic path (top). For the isotropic half of a piece of 27-in.-dia welded pipe (60 mm thick), insonified along a "1/2-V" path, a signal was observed at 0.5 MHz (bottom left), whereas none was seen at 1 MHz (bottom right). No signals were seen when the anisotropic half of the specimen was interrogated.

The present results show that the attenuation of ultrasonic waves is not necessarily lower in isotropic CCSS than in anisotropic CCSS; this is because anisotropic material provides a "window" of low attenuation for longitudinal waves propagating at about 45° to the columnar grains,

ISOTROPIC CCSS

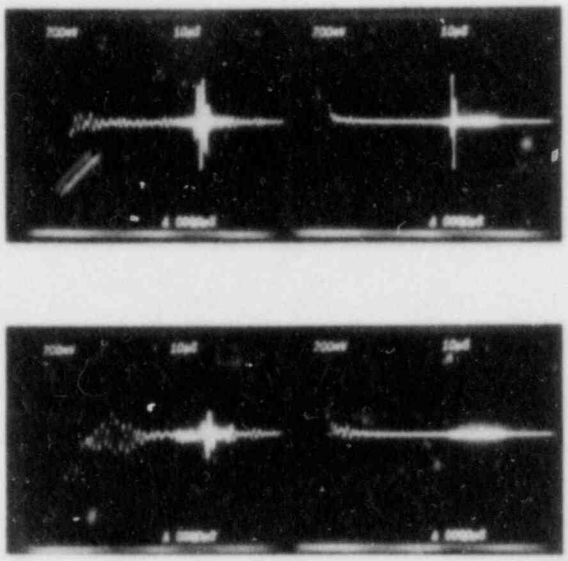

0.5 MHz 1.0 MHz

45° SHEAR WAVES

10-MM-DEEP EDM NOTCH

IN 25-MM-THICK PLATE

Fig. 21. Radio Frequency Echo Signals from Corner Reflectors in (Top) a 25-mm-thick Plate of Small-grained Wrought SS, Insonified along "1-V" Path, and (Bottom) a 27-in.-diam. Pipe Section of Isotropic CCSS, Insonified along "1/2-V" Path. Signals were obtained with (left) 0.5-MHz and (right) 1.0-MHz shear waves.

whereas isotropic material does not. If isotropic CCSS (with ∿1 to 2-mm-dia grains) is to be inspected, the results of this study suggest that 0.5-MHz shear waves may provide the best combination of penetration and sensitivity for manual-type inspection; they would give a high ratio (3-6) of wavelength to grain size, and would produce minimal mode conversion problems compared with longitudinal waves. For anisotropic material, 1-MHz longitudinal waves appear to be optimum.

(4) Ultrasonic Examination of a Manifold End Cap Containing an IGSCC

Cracks near the manifold end cap weld in the HATCH-2, Georgia Power Co. reactor, were detected by ultrasonic in-service inspection (ISI) techniques. A section of the end cap, including the weld and part of the connecting pipe, was sent to Argonne National Laboratory for ultrasonic examination. Destructive analysis was carried out and correlated with the ultrasonic data.

The pipe was examined with a Sonic Mark I pulser-receiver, KB-Aerotech dual 1.5-MHz, 45° shear-wave probe, and Ultragel couplant. The ultrasonic echo amplitude data as a function of the circumferential position of the transducer are presented in Fig. 22. Echo amplitudes are larger on the cap side of the weld. For both sides the variation in signal amplitude is about 10 dB. The indications reported by the field inspection team are also shown. Cracks were reported on both sides of the weld. Destructive analysis showed a crack on the cap side only, between positions 12 and 16 as indicated. Although this region had the largest echo signal in the inspection at ANL, the signal was only a few dB larger than other signals from geometrical reflectors on the cap side. Signals on both sides of the weld were generally greater than 10% DAC (with a 1/8-in.-dia side-drilled hole as a reference reflector). At positions 4 and 12, two separate signals were detected but with different transit times. This could be an indication of a crack, with one signal produced by the weld geometry (root) and the other by the crack. However, the destructive analysis showed that no cracks were present at position 4. In this case, both UT signals were from geometrical reflectors; one from the weld root, the other from lack of fusion.

Considerable overcalling of cracks is evident in this example. The overcalling appears to be due to the presence of an undercut on the cap side of the weld and a weld root oriented in such a way that UT signals on the pipe side reflected from the root were relatively strong.

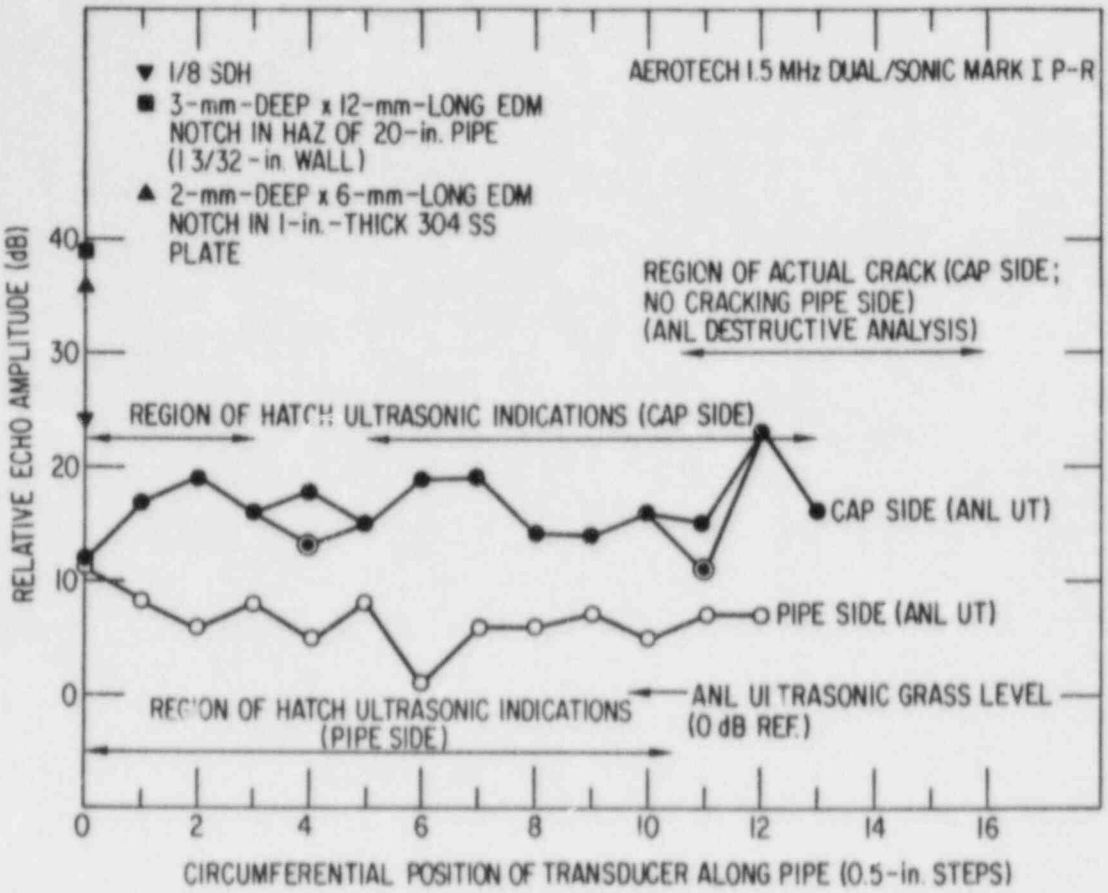

Fig. 22. Comparison of ANL and HATCH Ultrasonic Data from End Cap Weld and Indication of Region of Cracking Established by Destructive Examination.

It is generally believed that the depth of intergranular cracks cannot be estimated from the amplitude of the ultrasonic echo signal because of the extreme tightness of the crack, presence of corrosion products between crack surfaces, branching of the crack, and the irregular crack faces. The amplitude of the echo signal was compared with the crack depth from destructive analysis. As expected, no correlation between crack depth and echo amplitude was evident.

A commonly used technique for depth sizing is the probe motion technique (also called dynamic echo or amplitude drop). With this technique the echo amplitude is plotted versus transducer position as the

transducer is moved across the defect. The size (depth) of the reflector is considered to be the distance the transducer moves between the points 20 dB (or 6 dB) down from the maximum signal amplitude. This technique can provide useful data for reflectors with surfaces normal to the ultrasonic beam, for very rough surfaces, or for irregular geometries. For pipes with access limited to the outside surface, and with angle beam waves, attempts to measure the depths of intergranular cracks have been unsuccessful. The depths of shallow cracks are overestimated whereas deep cracks are undersized. The data in Fig. 23 are consistent with previous results, i.e., the 20-dB drop results using a 1/4-in. 2.25-MHz, 45° shear-wave are independent of depth. Furthermore, the same result is seen when a geometrical reflector

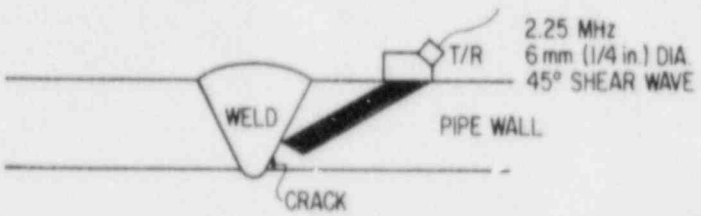

HATCH-II
END CAP TO PIPE WELD CRACK

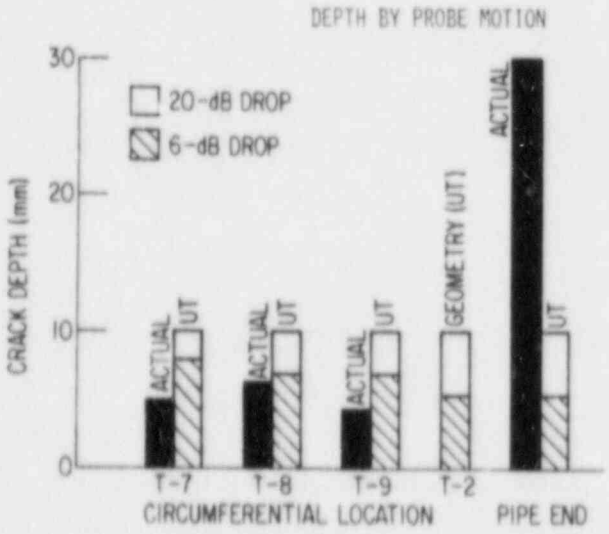

Fig. 23. Comparison of Ultrasonic Crack Depth Estimated by Probe Motion Technique and Actual Depth Established by Destructive Examination. Two geometrical reflectors are shown for comparison (one is a pipe end).

or the end of the pipe is examined. The same conclusion can be drawn from the 6-dB point data; that is, no correlation was found between the commonly used probe motion technique for sizing the depth of IGSCC and the actual crack depth.

If an ultrasonic echo from the tip of the crack can be seen, then the depth can be estimated by time-of-flight or satellite pulse methods. Signals from the crack tip would be seen on the CRT screen ahead of the signal from the base (corner) of the crack. With proper calibration procedures, this time difference can be related to crack depth. However, no crack-tip echo signals could be detected from this crack and no size estimates could be made.

The conclusions of this study are:

1. Although one region of the end cap contained IGSCC, the cracks were not present where field inspection teams had indicated (found by UT) because of the presence of geometrical reflectors.

2. Sizing of the intergranular cracks by commonly used probe motion techniques was not successful.

3. Crack-tip echoes were not detectable with conventional ultrasonic testing equipment and thus time-of-flight (satellite pulse) techniques for sizing were not successful.

(5) Summary - Ultrasonic NDE

Ultrasonic scattering data from IGSCC and geometrical reflectors have been acquired (the intergranular cracks yield an echo amplitude versus skew angle curve which is not as sharp as that for geometrical reflectors). The assembly of a multielement skew angle probe for IGSCC identification in 28-in. pipes was completed and the probe is under evaluation. Velocity of sound and attenuation data have been acquired in isotropic and anisotropic cast SS. The results show that a lower degree of anisotropy does not reduce attenuation in large-grain material since the

main factor in attenuation is the magnitude of ultrasonic wavelength relative to grain size. Large artificial flaws (e.g., 10-mm-deep notch at 40-mm path) could not be detected in isotropic CCSS (1 to 2-mm-dia grains) using longitudinal or shear waves down to 1 MHz frequency, but could be found with 0.5-MHz shear waves.

B. Analysis of Sensitization (J. Y. Park)

1. Introduction

The microstructural changes resulting from thermal exposure, which produce susceptibility to intergranular corrosion (IGC), are collectively known as sensitization. It is one of the major causative factors in the IGSCC of austenitic stainless steels in LWR environments. Under normal isothermal heat treatments, sensitization of austenitic stainless steels such as Types 304 and 316 occurs in the temperature range of about 500 to 850°C. However, Type 304 SS may be sensitized at temperatures below this range if carbide nuclei are present at grain boundaries. This low-temperature sensitization (LTS) phenomenon in Type 304 SS has been demonstrated in laboratory experiments in the temperature range from 350 to 500°C. Extrapolations of this behavior to plant operating temperatures (288°C) yield estimated times ranging from 10 to 1000 years for significant LTS to occur. These wide variations have been attributed to differences in the amount of strain, dislocation density, and/or impurity element concentration of the materials, but with the current level of understanding, the susceptibility to LTS of arbitrary heats of material cannot be assessed.

It is also not clear that the susceptibility to IGSCC produced by long, relatively low-temperature thermal aging can be adequately assessed by conventional measures of the degree of sensitization (DOS), such as the electrochemical potentiokinetic reactivation (EPR) technique or ASTM A262 Practices A through E. These tests have been developed and qualified primarily on the basis of the IGC susceptibility produced by high-temperature furnace sensitization or welding.

The objectives of this subtask are to establish the importance of LTS of materials under long-term reactor operating conditions, and to evaluate the effect of thermomechanical history on the correlation of IGSCC susceptibility with tests such as the EPR technique and ASTM A262 Practices A through E.

2. Summary of Results

The sensitization behavior of several heats of material was investigated under relatively short-term, high-temperature aging conditions. Iso-EPR curves were constructed for three heats of Type 304 SS in terms of aging time and temperature. Investigation of the effect of plastic deformation on LTS was initiated and a plastic strain of 5.3% was noted to have significantly increased EPR values of furnace sensitized Type 304 SS. CERT tests have been carried out for furnace or weld sensitized Type 304 SS in order to examine the correlation between EPR values and IGSCC susceptibility. A Type 304 SS specimen that was aged at 450°C for 1000 h had an EPR value of 2 C/cm^2 (a previously suggested critical value when sensitization was produced by relatively short-time high-temperature treatments), but showed IGSCC in a CERT test at 288°C in 8 ppm oxygenated water. Low-temperature aging of 4-in.-dia. pipe weldments treated with the IHSI, HSW, LPHSW and CRC remedies are continuing at 288, 315, 350, and 400°C. A Type 304 SS 22-in. end-cap-to-pipe weldment from the Hatch-2 reactor was examined. Typical intergranular cracks were found in the HAZ of the weldment.

3. Technical Progress

EPR measurements have been performed on Type 304 SS (Heat No. 10285, 30956, and 53319) specimens that were furnace heat treated at 450-750°C for 0.17-1000 h, in order to examine general high-temperature sensitization behavior. Time-temperature-EPR curves were constructed from the EPR measurements for temperatures of 600-700°C and times of 0.1-100 h (Fig. 24). The increase in EPR value due to aging is fastest for Heat No. 10285. Although the carbon concentration is the same (0.06 w/o) for the three heats, the concentrations of other alloy elements vary. Cihal[8] has proposed a model for the effect of such variations on relative resistance to intergranular corrosion, in which the relative resistance K is calculated from the effective chromium and carbon concentrations as follows:

$$Cr(\%)_{eff} = Cr(\%) + 1.7\ Mo(\%) \tag{8}$$

$$C(\%)_{eff} = C(\%) + 0.002[Ni(\%) - 7.9] \tag{9}$$

$$K = Cr(\%)_{eff} - 100\ C(\%)_{eff}\ . \tag{10}$$

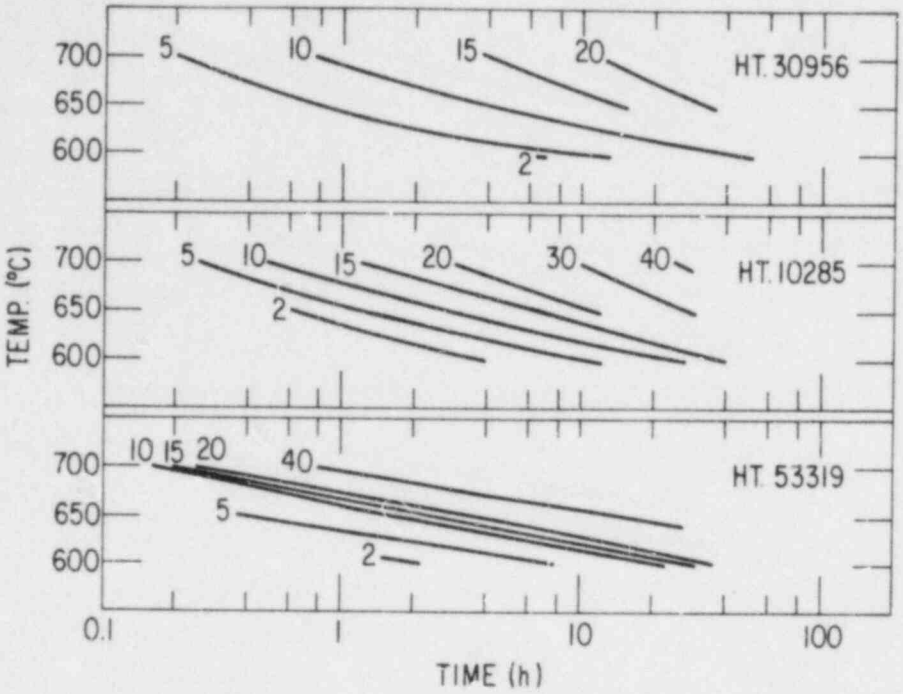

Fig. 24. Iso-EPR Curves for Type 304 Stainless Steel Heat Nos. 30956, 10285 and 53319. EPR value (C/cm^2) is noted for each curve.

The K values calculated for Heats 10285, 30956, and 53319 are 12.9, 13.7, and 12.4, respectively. The ranking of the relative resistance to intergranular corrosion is consistent with the EPR measurements. However, one cannot state conclusively that the minor differences in Cr, Ni, and Mo concentration account for all of the observed heat-to-heat variations in sensitization behavior. Faster LTS kinetics have been reported for mill-annealed Type 304 SS compared to solution-treated material, and the role of grain-boundary impurity segregation and other metallurgical features has been discussed previously.[9,10]

The EPR values were compared with the ASTM A262-A and -E test results for Types 304, 304NG, and 316NG SS specimens. The same specimen was used for the three different tests. The results are summarized in Table VI. Specimens with low EPR values ($\lesssim 4$ C/cm^2) exhibited light surface attack by the ASTM A262-E test. There are some discrepancies among the methods in terms of ranking the material according to susceptibility; e.g., for Type 304 SS (Heat No. 10285), the specimen (700°C/10 min + 450°C/257 h) with the highest EPR value (15 C/cm^2) showed less intergranular penetration than another specimen

Table VI. DOES OF Stainless Steels as Measured by EPR and ASTM A262 Methods

Alloy Type	Heat No.	Heat Treatment[a]	EPR, C/cm^2	Etch Structure (ASTM A262-A)	Intergranular Penetration Depth, mm (ASTM A262-E)
304	10285	SHT + 700°C/10 min	3	Step/Dual	Light Surface Etch
		SHT + 600°C/24 h	9	Dual	>1.2
		700°C/10 min + 500°C/45 h	8	Dual/Ditch	>0.8
		700°C/10 min + 452°C/120 h	8	Ditch	0.6
		700°C/10 min + 450°C/257 h	15		0.7
	30956	SHT + 600°C/24 h	9		1.3
		700°C/10 min + 450°C/256 h	10		>1.1
		650°C/4 h	8		0.6
		600°C/48 h	9		>1.6
	53319	SHT + 700°C/10 min + 500°C/238 h	11	Dual	0.03
		600°C/4 h	11		0.3
304NG	97770	SHT + 650°C/24 h	22		Light Surface Etch
		700°C/10 min + 500°C/146 h	7	Step/Dual	No attack
316NG	P91576	SHT + 700°C/146 h	2	Dual	Light Surface Etch
		650°C/530 h	4		

[a]SHT: Prior solution heat treatment (1050°C/0.5 h).

(SHT + 600°C/24 h) with a lower EPR value (9 C/cm^2). It is generally agreed that the ASTM A262-E test is sensitive to grain-boundary chromium depletion. The EPR test is also found to be sensitive to chromium depletion rather than chromium carbide precipitation; a Type 304 SS specimen (Heat No. 10285) was sensitized to an EPR value of 34 C/cm^2 by a 750°C/24 h treatment, but subsequent healing of grain boundary chromium depletion by a prolonged aging for 240 h at the same temperature substantially decreased the EPR value to 4 C/cm^2. Further work is needed for a better understanding of the correlation between the results by different DOS test methods.

The effect of plastic deformation on sensitization behavior of Type 304 SS is being investigated. Specimens (Heat No. 10285) were heat treated at 1050°C for 0.5 h and then at 700°C for 10 minutes. After these heat treatments the specimens were plastically deformed for 0-10% strain, and then aged at various time-temperature conditions. The results from the specimens with 5.3% plastic strain aged at 500-600°C are summarized in Table VII. The plastic deformation enhanced the EPR value significantly. It is believed that plastic deformation increases sensitization kinetics by introducing short-

Table VII. Effect of Plastic Strain on Sensitization

Heat Treatment[a]	EPR (C/cm^2)	
	ε_p = 0 (%)	ε_p = 5.3 (%)
500°C/100 h	3	5
550°C/24 h	6	8
600°C/24 h	16	21

[a]Specimens were heat treated (1050°C/0.5 h + 700°C/10 min) prior to plastic strain.

circuit paths for diffusion in materials and also possibly by increasing the number of carbide nucleation sites. Studies are continuing for different aging conditions, plastic strains, and heats of material.

The effect of thermomechanical history on the correlation of IGSCC susceptibility with various DOS measurements is also being investigated. IGSCC propagation rates have been measured for an LTS-treated Type 304 SS (Heat No. 10285) 1TCT specimen in water with 8 ppm dissolved oxygen, at 289°C and 8.3 MPa. The results are presented in Section C. The data suggest that although crack growth rate may depend strongly on DOS at very low levels, it is only weakly dependent on DOS at the higher levels characteristic of weld and furnace sensitization in high-carbon material. CERT tests have also been carried out in a high-purity water environment with 8 ppm dissolved oxygen at a nominal strain rate of 2×10^{-6} s^{-1}. For Heat No. 10285, an LTS treatment of 500°C/24 h resulted in an EPR value of 1 C/cm^2 and did not produce IGSCC in the CERT test, but an LTS treatment at lower temperature for a longer time, 450°C/1000 h, resulted in an EPR value of 2 C/cm^2 and produced IGSCC susceptibility (IG failure with 17% uniform elongation). CERT tests and DOS measurements are also being performed for LTS treatments at the other time-temperature conditions.

Low-temperature aging at 288, 315, 350 and 400°C of specimens from 4-in.-diameter Type 304 SS (Heat No. 53319) pipe weldments with four different remedy treatments (IHSI, HSW, LPHSW and CRC) is continuing. The specimens were examined by the ASTM A262-A test in the as-welded condition before aging.

All the weldments were sensitized in the HAZ, where ditch structures were evident (Fig. 25). These weldments may be close to the maximum level of IGSCC susceptibility that can be induced by sensitization per se; if this is the case, the effect of further LTS may not be fully revealed. An alternative heat of Type 304 SS with a moderate carbon concentration (0.05%) is being considered. A Type 304 SS 4-in.-dia. piping (Heat No. 82103) with 0.05 w/o carbon had been examined as a possible alternative heat of material. EPR values were measured after solution heat treatment (1050°C/1 h) and aging at 550-750°C for 0.08-24 h. The solution heat treatment caused extensive and uneven grain growth, and the subsequent aging resulted in rapid sensitization, and hence this heat was not chosen for further investigation. A field-failed Type 304 SS 22-in. pipe manifold weldment from Hatch-2 BWR was examined. Typical intergranular cracks were found in the HAZ of the weldment. The EPR values in the HAZ where cracks were found varied from 22 to 29 C/cm^2. A separate report is being prepared on this investigation.[11]

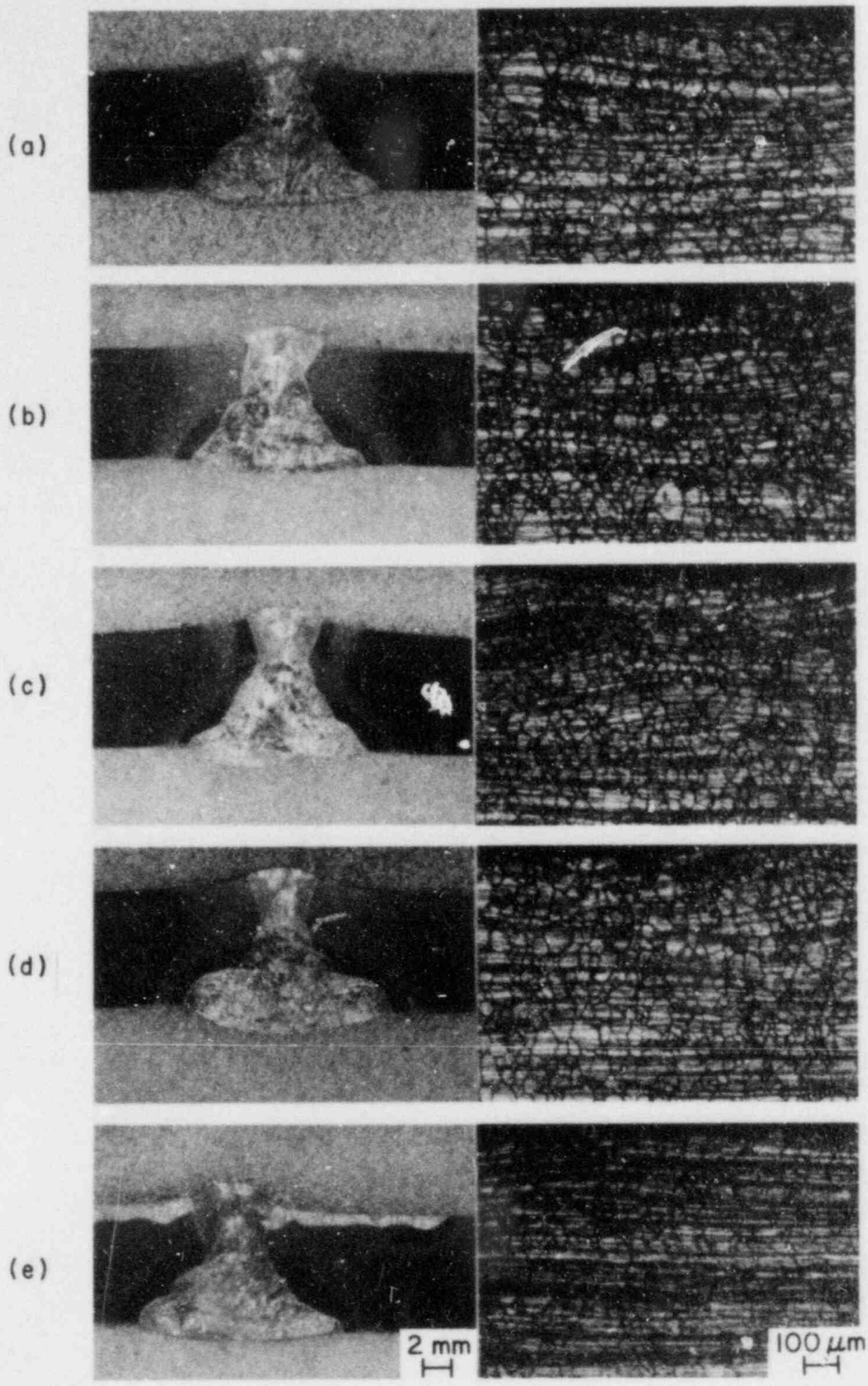

Fig. 25. ASTM A262-A Test Results for Type 304 SS (Heat No. 53319) Pipe Weldments. (a) Conventional weld, (b) IHSI, (c) HSW, (d) LPHSW, and (e) CRC.

C. Crack Growth Rate Studies (J. Y. Park and W. J. Shack)

1. Introduction

The early instances of IGSCC in operating BWRs generally occurred in small pipes, and the response to the detection of IGSCC was to repair or replace the cracked piping immediately. It is now clear that for reactors with standard Type 304 SS piping material, cracking can occur anywhere in the recirculation system, including the main recirculation line. Because of the severe economic consequences of long forced outages for repair or replacement, the utilities have considered other approaches for dealing with cracked pipe. The possibilities include continued operation and monitoring for any subsequent growth for an indefinite period, continued operation and monitoring until a repair can be scheduled to minimize outage, and immediate repair or replacement.

Understanding crack growth behavior is, of course, important for other reasons besides assessing the safety implications of flawed piping. A better understanding would permit a more rational extrapolation of laboratory test results to the prediction of behavior in operating plants. Current work on the measurement of crack growth rates seeks to characterize these rates in terms of the linear-elastic-fracture-mechanics (LEFM) stress intensity as well as the level of sensitization and the amount of oxygen present in the coolant. The work in this subtask is aimed at a systematic evaluation of the validity of the use of LEFM to predict IGSCC growth. The capability of data obtained under one type of loading history to predict crack growth under a different loading history will be investigated. The effect of flaw geometry on crack propagation rates will also be considered.

2. Summary of Results

Stress corrosion crack growth rates were measured in furnace sensitized Type 304 stainless steel in deionized water with 8 ppm dissolved oxygen at 289°C and 8.3 MPa. The degree of sensitization (DOS) varied from 4-15 C/cm^2 as measured by the EPR method. The influence of load ratio and

frequency was investigated over the range R = 0.5-0.94 and f = 1×10^{-3} - 1×10^{-1} Hz, with maximum stress intensities K_{max} = 28-38 MPa $m^{\frac{1}{2}}$. Under these conditions, crack growth rates varied from 1×10^{-10} to 6×10^{-9} m/s. Crack growth rate increased at low R values. No significant correlation could be established between the growth rates and crack-tip strain rates estimated by a linear fracture mechanics approach. The data also suggest that although crack growth rate may strongly depend on DOS at very low levels, it is only weakly dependent on DOS at the higher levels most characteristic of weld and furnace sensitization in high-carbon material.

3. Technical Progress

Crack growth rate tests have been continued for Type 304 SS (Heat No. 10285) 1TCT specimens in high-purity deionized water with 8 ppm dissolved oxygen at 289°C and 8.3 MPa (1200 psi). The specimens had been furnace heat treated for 700°C/10 min, with a subsequent additional treatments of 450°C/146 h, 450°C/250 h or 500°C/24 h. The EPR values of companion test coupons were 8, 15 and 4 C/cm^2 for specimen numbers C-09, -17, and -11, respectively. Growth rates at maximum stress intensities (K_{max}) ranging from 19-34 MPa $m^{\frac{1}{2}}$, load ratios (R) of 0.5, 0.94 and 1, and frequencies (f) of 0, 2×10^{-3} and 1×10^{-1} Hz have been reported previously.[12] The cyclic-loading tests have been performed using a sawtooth waveform with an unloading time of 5 s. The current series of tests established (at a fixed K) the effect of R ratio and frequency on the growth rate. The tests were carried out at R = 0.5, 0.6, 0.7, 0.79, 0.8 and 0.94, f = 0, 1×10^{-3} and 2×10^{-3} Hz and the results were analyzed in terms of crack-tip strain rates. The crack length was continuously monitored by the compliance method, using in-situ clip gages. Figure 26 shows crack length versus test time for three 1TCT specimens. Interruption or changes in the test conditions (R, f or K value) occurred at points (1) through (21). Average crack propagation rates were obtained by least-squares linear regression analysis for each test condition, and the results, along with those reported previously,[12] are summarized in Table VIII. The calculated crack propagation rates for specimens C-09 and C-17 do not include data obtained beyond the interruption (9), since the crack lengths for those specimens appeared to decrease at later times (Fig. 26); this suggested that the clip gages had begun to malfunction.

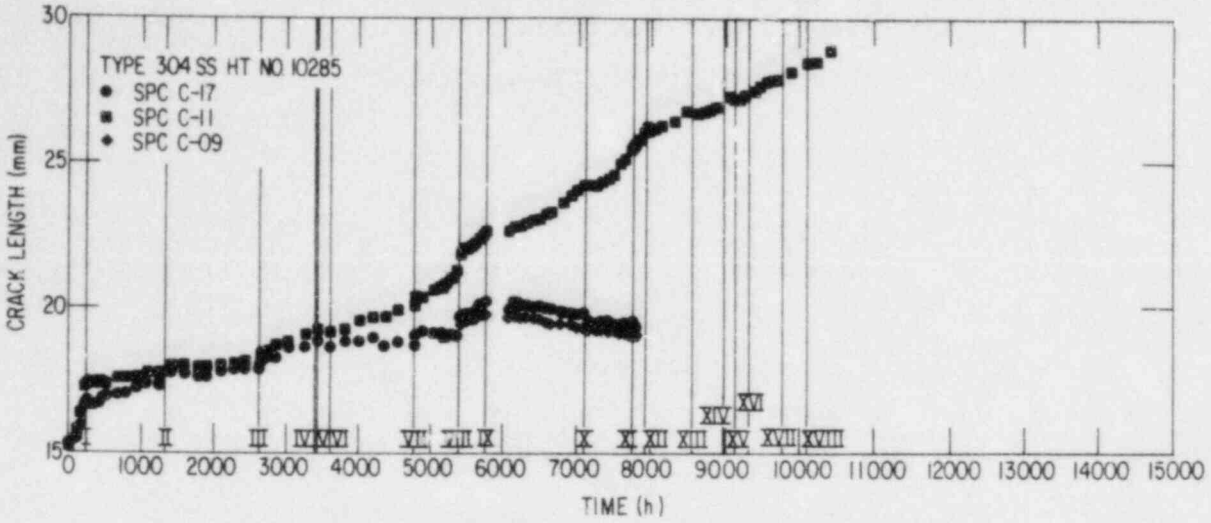

Fig. 26. Plots of Crack Length vs Time for Heat No. 10285 Specimens.

Table VIII. Crack Propagation Rates in Type 304 SS Specimens (Heat No. 10285) Sensitized to Two Levels and Tested in 289°C Water with 8 ppm O_2

F(Hz)	R	$\dot{\varepsilon}_T(s^{-1})^a$	K_{max}(MPa $m^{1/2}$)	$\dot{a}$(m/s)
		EPR = 4 C/cm^2		
0	1	-	33-34	1.2×10^{-10}
0	1	-	36-37	2.9×10^{-10}
0	1	-	37-38	4.5×10^{-10}
1×10^{-3}	0.5	1.4×10^{-4}	31-32	2.6×10^{-10}
2×10^{-3}	0.5	2.7×10^{-4}	30-31	8.9×10^{-10}
2×10^{-3}	0.5	2.7×10^{-4}	30-33	3.4×10^{-9}
2×10^{-3}	0.6	1.7×10^{-4}	32-33	6.6×10^{-10}
2×10^{-3}	0.7	9.3×10^{-5}	30-31	3.4×10^{-10}
2×10^{-3}	0.7	9.3×10^{-5}	32-33	5.9×10^{-10}
2×10^{-3}	0.79	4.5×10^{-5}	31-32	5.5×10^{-10}
2×10^{-3}	0.79	4.5×10^{-5}	34-36	5.4×10^{-10}
2×10^{-3}	0.8	4.1×10^{-5}	29-32	7.4×10^{-10}
2×10^{-3}	0.8	4.1×10^{-3}	30-31	4.4×10^{-10}
1×10^{-1}	0.94	1.8×10^{-4}	30-31	3.1×10^{-10}
1×10^{-1}	0.94	1.8×10^{-4}	31-32	1.9×10^{-10}
		EPR = 15 C/cm^2		
0	1	-	32-33	2.2×10^{-10}
2×10^{-3}	0.5	2.7×10^{-4}	30-32	2.8×10^{-9}
2×10^{-3}	0.6	1.7×10^{-4}	28-29	5.6×10^{-9}
1×10^{-1}	0.94	1.8×10^{-4}	30	2.1×10^{-10}

[a] $\dot{\varepsilon}_T = -1/T \ln[1 - (1 - R)^2/2]$.

Ford[13] has proposed that the crack growth rate is proportional to the square root of the crack-tip strain rate, i.e.,

$$\dot{a}_{SCC} = A\dot{\varepsilon}_T^n \ , \tag{11}$$

where $\dot{a}_{SCC}$ is crack growth rate, $\dot{\varepsilon}_T$ is crack-tip strain rate, and A and n ($\sim$0.5) are constants. As discussed in Section D this relation appears to be consistent with data obtained from CERT tests at different extension rates.

Analysis of fracture mechanics crack growth tests requires an expression for the crack-tip strain rate. Under constant applied loads, the crack-tip strain rate is determined by the time-dependent plastic deformation, i.e., creep, near the crack tip. For cyclic applied loads of sufficiently high frequency (and sufficiently low R values), the strains are imposed by the external loading mechanism. Estimates of the crack-tip strain rates in this case can be obtained from LEFM. Scott and Truswell[14] have suggested a relation of the form

$$\dot{\varepsilon} = \frac{1}{T} \ln[1 - (1 - R)^2/2] \ , \tag{12}$$

where T is the rise time for the tensile portion of the load cycle. (Related expressions for crack-tip strains in fatigue have been proposed by Rice[15] and others.) Equation (12), since it neglects constant-load creep, predicts $\dot{\varepsilon}_T$ = 0 for the constant load case. It also predicts that the crack-tip strain rate is independent of the value K and hence, together with Eq. (11), predicts that the crack growth rate is independent of K. This prediction is contradicted by many experimental observations, but the use of Eq. (12) to analyze the effect of R and T at fixed K was explored. Estimates of the crack-tip strain rate from Eq. (12) are included in Table VIII for the tests on Heat 10285 where both R and f are varied. Figure 27 shows the crack-tip strain rate versus crack growth rate. No significant correlation can be established. Tests are currently in progress for additional R values and frequencies, and alternative formulations for the crack-tip strain rate are being explored.

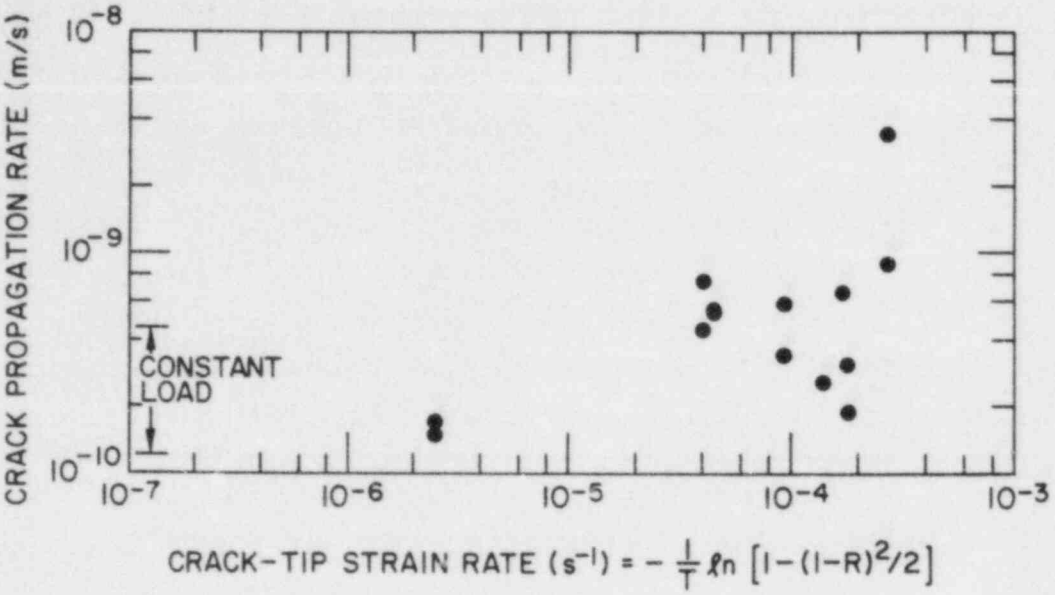

Fig. 27. Crack Propagation Rate vs Crack Tip Strain Rate for Type 304 SS (Heat No. 10285).

D. Evaluation of Nonenvironmental Corrective Actions (P. S. Maiya and W. J. Shack

1. Introduction

The fundamental premise of the current efforts to prevent IGSCC in BWR piping is that IGSCC involves a complex interaction among material susceptibility (sensitization), the stresses acting on the material, and the environment; and that suitable alteration or variation of these parameters can produce immunity to IGSCC. Nonenvironmental corrective actions seek to mitigate either the material susceptibility or the state of stress on the inside surface of the weldment. They include techniques for improving the margin against IGSCC of a susceptible material like Type 304 SS and the identification of alternate materials that are inherently more resistant to IGSCC.

The objective of the current work is an independent assessment of the proposed remedies developed by the utilities and the vendors. Additional testing and research has been carried out to eliminate gaps in the existing data base on alternative materials and fabrication and to develop a better understanding of the relation between the existing laboratory results and satisfactory in-reactor operating performance. Current efforts in this task include additional screening tests for alternate materials, a study of stress redistribution near flawed weldments with IHSI and weld overlays to determine the effect of in-service loading conditions on residual stress distribution in the piping, and analyses of the remaining lifetime of cracked pipe to develop a margin for leak before break (LBB).

2. Summary of Results

The relative susceptibility of Types 316NG, 316 and 304 SS to SCC in environments with impurity additions at levels similar to those specified in Regulatory Guide 1.56 limits has been investigated. CERT experiments were performed over a range of strain rates, $\dot{\varepsilon}$, between 10^{-5} and 4×10^{-8} s^{-1} at 289°C in oxygenated water containing chloride and sulfate impurities, which

were added as acids. These tests have shown that Type 316NG SS is extremely resistant to IGSCC under the heat treatment and environmental conditions where the conventional Types 316 and 304 SS suffer significant degradation as a result of IGSCC. However, Type 316NG SS does show susceptibility to transgranular SCC (TGSCC) in impurity environments, which could be of interest under transient or even under normal BWR water-chemistry conditions. In high oxygen environments (e.g., 8 ppm O_2 + 0.5 ppm Cl^-) susceptibility to TGSCC occurs at a higher strain rate ($\dot{\varepsilon} \gtrsim 2 \times 10^{-6}$ s^{-1}) but in the normal environments, based on limited experimental results, TGSCC susceptibility occurs when the strain rate is lowered in the test from 10^{-6} to $\lesssim 10^{-7}$ s^{-1}. However, the average transgranular crack growth rates are roughly one order of magnitude lower than the average intergranular crack growth rates observed in Type 316 SS under identical heat treatment and environmental conditions.

Based on CERT test data and consistent with the results reported under Subtask E, it also appears that for impurity levels within the Regulatory Guide 1.56 limits, intergranular crack growth rates in sensitized austenitic stainless steels can be 3-4 times higher than those obtained for the same materials in high-purity water under the same loading conditions. This enhanced susceptibility is associated with specific anions (e.g., SO_4^{2-}, Cl^-) and not with cations such as Na^+, H^+ (and hence not with the pH per se). The cracking susceptibility of the materials generally increases with the degree of sensitization (as quantified by EPR techniques) in impurity environments, although this is reflected to a lesser degree in the failure times than in the average crack growth rates determined in CERT tests.

The extent of cracking was found to be a significant function of strain rate (i.e., it increases as $\dot{\varepsilon}$ decreases). A model based on mechanistic considerations which describes the effect of strain rate on IGSCC susceptibility has been developed and correlations between the strain rate (nominal) and quantifiable IGSCC susceptibility parameters (e.g., average crack growth rate and time to failure) have been derived. These relationships are in good agreement with the experimental results of this and other studies. The model appears applicable to a wide range of water chemistries that are of interest in BWRs. It permits determination of IGSCC susceptibility at the slower strain rates based on limited results obtained at the higher strain

rates. Thus the model provides a basis for extrapolating the laboratory results obtained at higher strain rates to the slow strain rate regime ($\lesssim 10^{-8}$ s^{-1}) characteristic of loading conditions on piping in operating BWRs. In addition, it is shown that the average crack-tip strain rate in CERT experiments can be estimated by use of a J-integral approach. The experimental data suggest average crack growth rate is proportional to the square root of the estimated average crack tip strain rate. This result is consistent with that deduced from a mechanistic model, and the crack tip strain rate approach as well as the analysis of strain rate effects represent an important step in developing a better understanding of the effect of loading history on IGSCC susceptibility.

Stress relaxation experiments were performed on Types 316 and 304 SS to investigate stress/strain/strain-rate behavior at 28-289°C and hence to develop a better understanding of the effect of loading history on IGSCC. Experiments at low temperature have been completed and the data can be described by constitutive equations developed by Hart[16] over a wide range of strain rates from 10^{-4}-10^{-10} s^{-1}. For materials in the as-received, solution-annealed and sensitized conditions, it is found that the strain rates produced for an imposed stress depend on the material condition.

Numerous calculations have been performed to demonstrate the effectiveness of residual stress improvement techniques such as IHSI and weld overlays, however, most of the results pertain to uncracked weldments. Finite element calculations have been carried out in this program, under a subcontract to E. F. Rybicki, Inc., to quantify the range of crack sizes and applied loads for which the IHSI and weld overlay remedies may be effective in mitigating IGSCC in flawed piping. In the case of IHSI, calculations of residual stress were performed for 24-in. and 12-in. Schedule 80 weldments with preexisting flaws of ∿8 and 40% throughwall, respectively. For the 24-in. pipe with the ∿8% throughwall crack, high tensile stresses (∿310 MPa) were present ahead of the crack tip, whereas with IHSI, the stresses were quite low (∿35 MPa) for an applied stress of ∿100 MPa. In the case of the 12-in. pipe with a ∿40% throughwall flaw, the crack tip was contained in a compressive stress field under typical applied loads, however, for highly stressed joints the crack tip would be subject to tensile stresses.

The calculations for weld overlays were performed for 12-in. Schedule 80 pipe weldments with preexisting circumferential cracks of ∿20% throughwall on each side of the weld and for a ∿60% throughwall crack located at the weld centerline. The results show that the stresses ahead of the crack tip for the 60% throughwall crack were compressive at an applied load of ∿60 MPa, which is typical for reactor piping of this size, and tensile at a load of ∿100 MPa. The complex pattern of crack opening displacements is indicative of the intense deformation at the crack tip produced by the weld overlay process. The calculations suggest that the overlay is effective in producing a favorable compressive residual stress state at the crack tip even for deep, 360 degree cracks. However, the present calculations are not adequate to define the range of crack depths or applied loads for which the weld overlay or IHSI can be expected to be effective in mitigating the propagation of IGSCC in reactor piping.

If IGSCC growth is not arrested by a favorable residual stress distribution, failure of the piping could occur by continued growth of a stress corrosion crack. Thus, it is important to assess the remaining lifetime of cracked pipe to prevent incidents that involve a significant loss of coolant during reactor operations. In this regard, a meaningful leak-before-break (LBB) margin requires that detectable leakage occur from a cracked pipe before it experiences rapid crack growth and final failure due to mechanical and pressure loads. Evaluation of this margin involves an analysis of the failure behavior of a pipe for a given crack geometry, crack opening area, and water/steam flow through the crack opening. An analysis of the time from the onset of a specified leakage rate (i.e., 5 gpm) to structural failure has been performed for 10- and 24-in. pipe in terms of the fractional depth of a 360° crack and the length of the throughwall portion of this crack for several applied loads. The results indicate that the length of the throughwall crack needed to obtain detectable leakage is not very dependent on pipe diameter, whereas the size of the crack to produce collapse is proportional to the pipe diameter. Consequently, the LBB margin increases with pipe size and decreases for high applied loads. Based on conservative estimates of crack growth rates and the residual stress distribution in the piping, the times from the onset of leakage (5 gpm) to failure were estimated for several crack geometries. For simple throughwall flaws the times range

from two months for the 10-in. pipe to three to four months for the 24-in. pipe. The time periods for pipes with compound cracks (i.e., a 360° part-through crack in addition to the throughwall crack) were relatively long for most crack geometries (viz., ∿10 days). The LBB margin was violated only in the case of very deep, very long part-through cracks. However, since the leakage rate is high through long cracks ($\gtrsim$30% of the circumference) at typical applied loads, although LBB would still be valid, the leakage rate would exceed the make-up water capacity of most BWRs and necessitate use of the high-pressure emergency core cooling system.

3. Technical Progress

a. Relative Susceptibility of Types 316NG, 316, and 304 SS in Impurity Environments

CERT tests were performed on Types 316NG (Heat No. P91576), 316 (Heat No. 0590019), and 304 (Heat No. 53319) stainless steels in oxygenated water (with 0.2 and 8 ppm dissolved oxygen) with or without Cl^- and SO_4^{2-} impurities. The chemical composition of the materials has been reported previously.[17] Specimens were tested in the solution annealed (1050°C/0.5 h), solution annealed and aged conditions (600-700°C/2-24 h), and in the as-welded condition with a subsequent heat treatment (500°C/24 h). The impurity additions in the initial studies were chosen to be consistent with the operating limits under off-normal conditions although the main focus of our effort is on studies under water chemistry conditions consistent with the Reg. Guide 1.56 limits. The impurities were added as hydrochloric and sulfuric acids. The characterization of water chemistry in terms of pH and conductivity has been reported previously.[18] The tests were conducted at different strain rates ($\dot{\varepsilon}$ = 10^{-5} to 4 x 10^{-8} s^{-1}) for the materials in impurity environments to establish the synergistic effects of microstructural state of the material, environment and strain rate in a quantitative manner. The SCC susceptibility was characterized in terms of macroscopic parameters such as time to failure (t_f), strain at failure ($\varepsilon_f \simeq \dot{\varepsilon} \times t_f$), uniform elongation, reduction in area, and maximum stress which follow from the tests. In addition the fracture surfaces were examined by scanning electron microscopy (SEM) to determine the fracture mode (e.g., IGSCC, TGSCC or ductile). When SCC occurred, the maximum crack length (a_f, intergranular or

transgranular) was measured and used to estimate the average crack velocity, which is a sensitive parameter (compared to either t_f or a_f) for expressing the severity of SCC. In making this estimate it was assumed that the crack length at initiation, a_o, is small compared to a_f and crack initiation in the environment occurs at relatively low strains compared to total strain, so that the time to attain this strain (crack initiation time) is small compared to t_f and can be ignored. The assumption of a small crack length at initiation ($a_o \ll a_f$) very early in life ($t_o \ll t_f$) is based on some preliminary interrupted CERT tests on Type 316 SS. This assumption is consistent with that used by other investigators[19,20] although some exceptions have been found.[21]

It has been shown previously[18] that Type 316NG SS is extremely resistant to IGSCC even after fairly severe heat treatments (e.g., SA + 650°/24 h) and aggressive environmental conditions (oxygenated water with 8 ppm O_2 containing chloride/or sulfate impurities at levels $\geq$0.2 ppm). However TGSCC has been observed in Type 316NG stainless steel. Most of the available data are in environments somewhat outside of the normal BWR water chemistry limits. However, more recent tests have produced TGSCC in environments much closer to or within the Reg. Guide 1.56 limits, i.e., in water containing 0.2 ppm dissolved oxygen and 0.2 ppm Cl^- or 0.1 ppm SO_4^{2-}. These include tests at a low strain rate (4×10^{-8} s^{-1}) on weldments with a treatment of 500°C/24 h.

In the second test TGSCC occurred at locations farther from the heat affected zone. (Fracture occurred at a distance of ∿13 mm from the weld-metal interface.) This test was interrupted after ∿500 h, which corresponds to an accumulated strain of about 7.0%. Examination of the gauge section showed the presence of a surface crack (TG) of ∿115 μm in length. This observation suggests that the TG crack initiation may occur at reasonably small strains and is not simply an artifact produced by the very high strains produced in a CERT test. TGSCC also occurred in the same environment at a higher strain rate of 1×10^{-7} s^{-1}. Because this test had about 3 interruptions as a result of malfunction of the feedwater pump, the experiment is being repeated. The average crack growth rates determined from these two tests suggest that the transgranular crack growth rate in the nuclear grade material in a normal BWR-type environment is approximately an order of

magnitude lower than the intergranular crack velocity in the conventional Type 316 SS as shown in Fig. 28. Although the data are obtained at different strain rates, the limited experimental results (indicated by symbols) are consistent with the predictions of a model (to be discussed later), which relates the crack growth rate to the strain rate and provides some basis for the comparison of the data. A similar relationship between $\dot{a}_{av}$ versus $\dot{\epsilon}$ for Types 316, and 316NG SS was observed in tests in oxygenated water (8 ppm dissolved O_2) with 0.5 ppm Cl^- under identical heat treatment conditions. Comparison of the data shown in Figs. 28 and 29 shows that the average crack growth rates in the aggressive environment are approximately 5 times the crack growth rates determined in environments consistent with the Reg. Guide 1.56 limits.

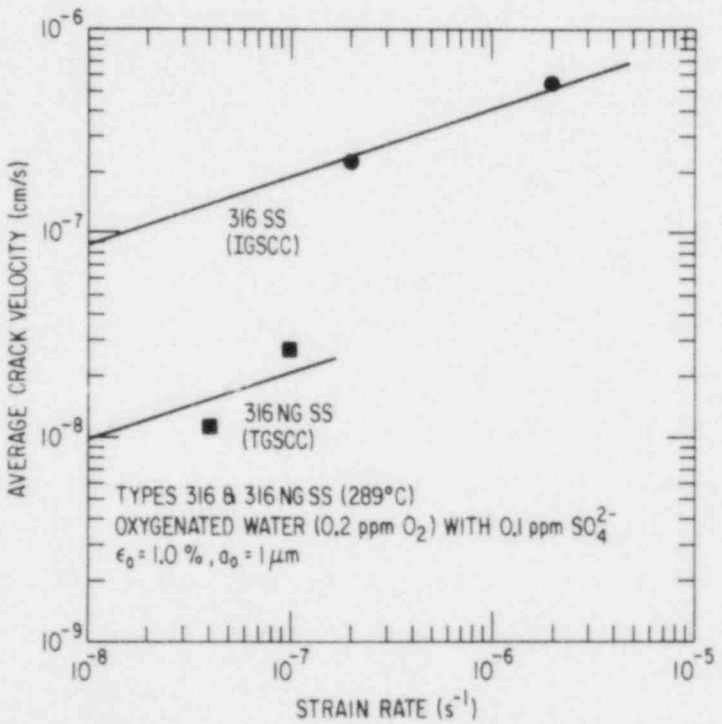

Fig. 28. Relative SCC Susceptibility of Types 316NG and 316 SS as a Function of Strain Rate in a Normal BWR-type Environment.

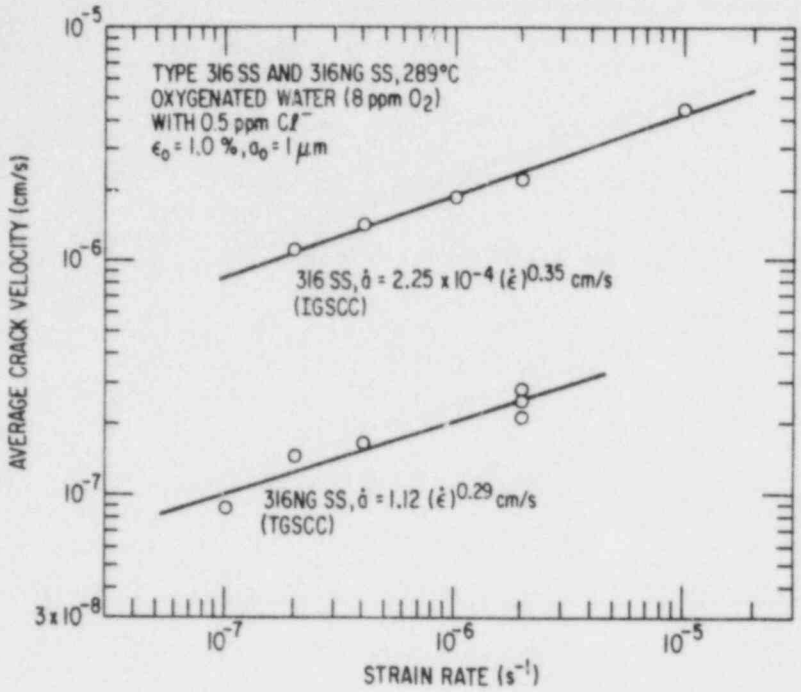

Fig. 29. Relative SCC Susceptibility of Types 316NG and 316 SS as a Function of Strain Rate in an Off-normal BWR-type Environments.

Examination of other properties such as uniform elongation, reduction in area, and maximum stress (σ_{max}) also provides some valuable information on SCC. For example, Fig. 30 shows that for 316 SS, σ_{max} decreases with a decrease in strain rate in the SCC regions. Although at present the data are insufficient to draw any firm conclusion, these results suggest that the maximum stress may become independent of strain rate in the slow-strain-rate regime ($\dot{\epsilon} \lesssim 10^{-8}$ s^{-1}). This possibility is more clearly illustrated in Fig. 31, which shows a normalized plot of σ_{max} (SCC)/σ_{max} (no SCC) versus $\dot{\epsilon}$; σ_{max} (SCC) represents the maximum stress in the strain rate regime where IGSCC occurs and σ_{max} (no SCC) is the maximum stress observed for solution-annealed Type 316 SS at $\dot{\epsilon}$ = 2 x 10^{-6} s^{-1} [σ_{max} (SCC) = 491 MPa]. The latter stress is expected to be independent of $\dot{\epsilon}$ at 289°C. The data shown in Fig. 31 strongly suggest that σ_{max} (SCC) becomes constant and independent of strain rate at slower strain rates (e.g., $\dot{\epsilon} \lesssim 10^{-8}$ s^{-1}). This constant stress may be related to the "threshold stress" required in a constant-load test to propagate an intergranular crack in Type 316 SS in the chloride-containing environment.

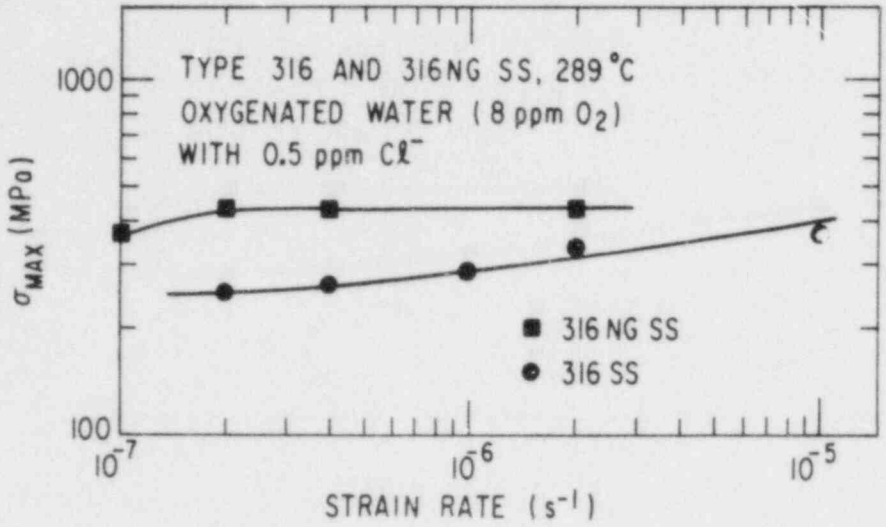

Fig. 30. Variation of Maximum Stress with Strain Rate for Types 316 and 316NG SS.

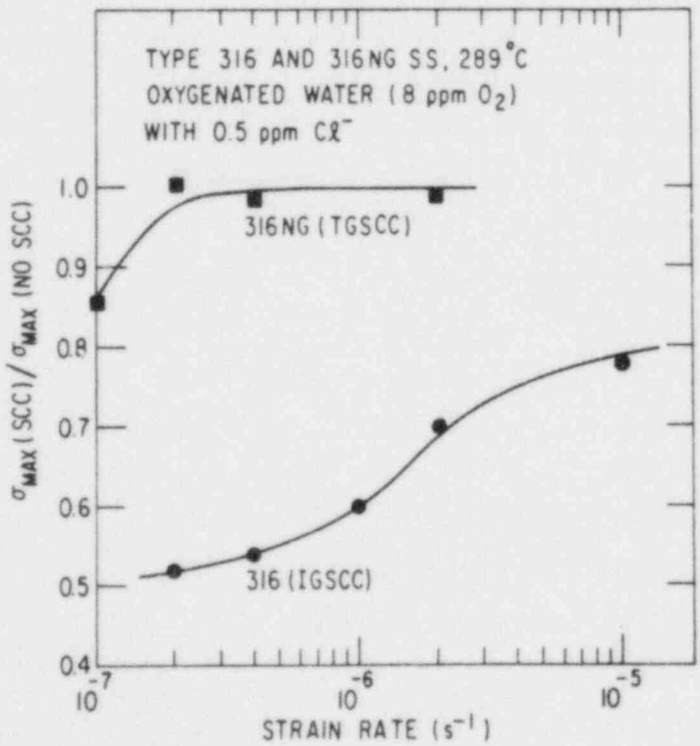

Fig. 31. Variation of σ_{max} (SCC)/σ_{max} (no SCC) with Strain Rate for Types 316 and 316NG SS in Oxygenated Water with 0.5 ppm Cl^- at 289°C.

Properties related to ductility, such as uniform elongation and reduction in area, also decrease with $\dot{\epsilon}$ in a manner that is consistent with the variation of σ_{max} with $\dot{\epsilon}$ (see Fig. 32). For Type 316NG, the tests show that σ_{max} starts decreasing at a strain rate of $\sim 2 \times 10^{-7}$ s^{-1} (see Figs. 30 and 31). These results suggest that tests on the nuclear-grade material must be performed at slower strain rates than those typically used to study IGSCC of conventional stainless steels. Further testing will emphasize slower strain rates and impurity environments consistent with the long-term operating limits in BWRs.

Although the average crack growth rate decreases with a decrease in strain rate, the extent of cracking, in particular the maximum crack length increases with a decrease in strain rate, i.e., cracking susceptibility increases with a decrease in strain rate. Since cracking in a reactor occurs at strain rates which are two or more orders of magnitude lower than those used in the laboratory, it is extremely important to understand the effect of strain rate on SCC susceptibility. We have developed a model relating $\dot{\epsilon}$ (nominal) and IGSCC parameters. The model is consistent with a diffusion-controlled crack-growth behavior and a fracture criterion based on a J-integral approach.

Based on a slip dissolution model, Ford[22,23] has proposed that

$$\dot{a} = A_T(\dot{\epsilon}_T)^{0.5}, \tag{13}$$

where A_T is a constant that is dependent on parameters which control the passivation rate, such as degree of sensitization and oxygen and impurity contents of the aqueous environment. Ford's model assumes that the strain rate determines the rate of oxide film rupture, and that the current decay following film rupture (which is a measure of the metal dissolution) follows parabolic kinetics. The latter assumption is based on measurements of anodic current decay transients at freshly created metal surfaces in passive steels in dilute solutions, which often show a $t^{-\frac{1}{2}}$ decay law. Such a law has been tentatively interpreted as suggesting that the rate-controlling step in the dissolution-repassivation process is the diffusion of ions from the crack tip. (Repassivation is assumed to occur between successive ruptures of the

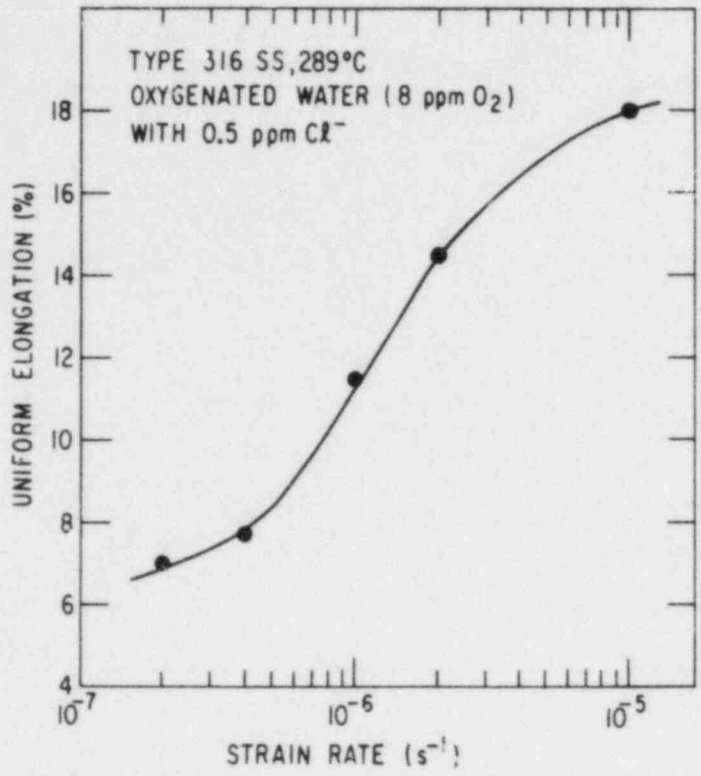

Fig. 32. Effect of Strain Rate on Uniform Elongation in Type 316 SS.

protective oxide, except possibly at high strain rates.) In order to relate the crack growth behavior to more macroscopic parameters and to determine whether the CERT results obtained in this study are consistent with Ford's model, a model for computing crack-tip strain rate $\dot{\varepsilon}_T$ in CERT tests is required. This was done by defining $\dot{\varepsilon}_T$ in terms of the crack-tip opening displacement δ and expressing δ in terms of the J-integral using an analysis similar to that used by Mowbray[24]

$$J = \alpha \varepsilon a = \beta \sigma_f \delta, \tag{14}$$

where α and β are constants, ε is the strain, a is the crack length, and σ_f is the flow stress. The crack-tip strain rate is given by

$$\dot{\varepsilon}_T = \frac{\dot{\delta}}{\delta} = \frac{\dot{J}}{J} = \left(\frac{\dot{\varepsilon}}{\varepsilon} + \frac{\dot{a}}{a} \right). \tag{15}$$

combining Eqs. (13) and (14) we obtain

$$\dot{a} = A_T \left(\frac{\dot{a}}{a} + \frac{\dot{\varepsilon}}{\varepsilon} \right)^{0.5} , \tag{16}$$

where a and $\dot{a}$ are the crack length and crack velocity at any time t. For CERT tests,

$$\frac{\dot{\varepsilon}}{\varepsilon} = \frac{1}{t} ; \tag{17}$$

therefore,

$$\dot{a} = A_T \left(\frac{\dot{a}}{a} + \frac{1}{t} \right)^{0.5} . \tag{18}$$

The exact analytical solution of Eq. (18) is

$$a = A_T \sqrt{6t} , \tag{19}$$

which suggests a diffusion-controlled crack propagation process. If we define $a = a_f$ and $t = t_f$ at failure, Eq. (19) becomes

$$a_f = A_T \sqrt{6t_f} = A t_f^{0.5} , \tag{20}$$

where $A_T = \sqrt{6}\ A$. An example of the good agreement between Eq. (20) and experimental results obtained for Type 316 SS in a chloride environment is illustrated in Fig. 33. In Eq. (20) A_T is a constant independent of $\dot{\varepsilon}$ but is assumed to be a function of the microstructural state of the material (for example, degree of sensitization) and the environment. It is important to point out that we have not obtained evidence in this study concerning crack growth behavior prior to failure.

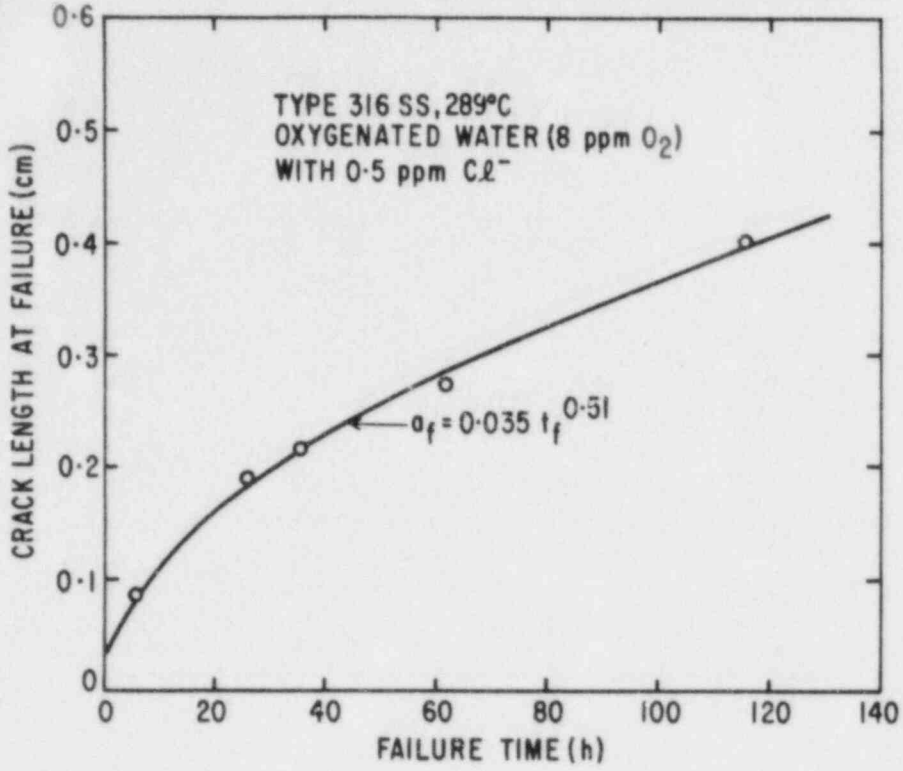

Fig. 33. Variation of Crack Length at Failure (a_f) with Time to Failure (t_f) in Tests Conducted at Different Strain Rates.

Equation (20) is a useful relation, but is not sufficient to determine t_f; an additional fracture criterion is required. A possible fracture criterion is that the failure of the specimen occurs when the J-integral (see Ref. 24) approaches the value J_c, given by

$$J_c = C_o \varepsilon_f^{n+1} f(n) a_f \tag{21}$$

or

$$\simeq C \varepsilon_f^{n+1} a_f$$

where J_c is a constant that depends on the material and geometry but is assumed to be independent of strain rate; C_o = material parameter; n = strain-hardening exponent at large strains (near fracture); f(n) = function of n, ε_f = strain at failure ($\simeq \dot{\varepsilon} t_f$); and $C \simeq C_o f(n)$. A log-log plot of a_f versus ε_f (Fig. 34), can be fit reasonably well (the correlation coefficient

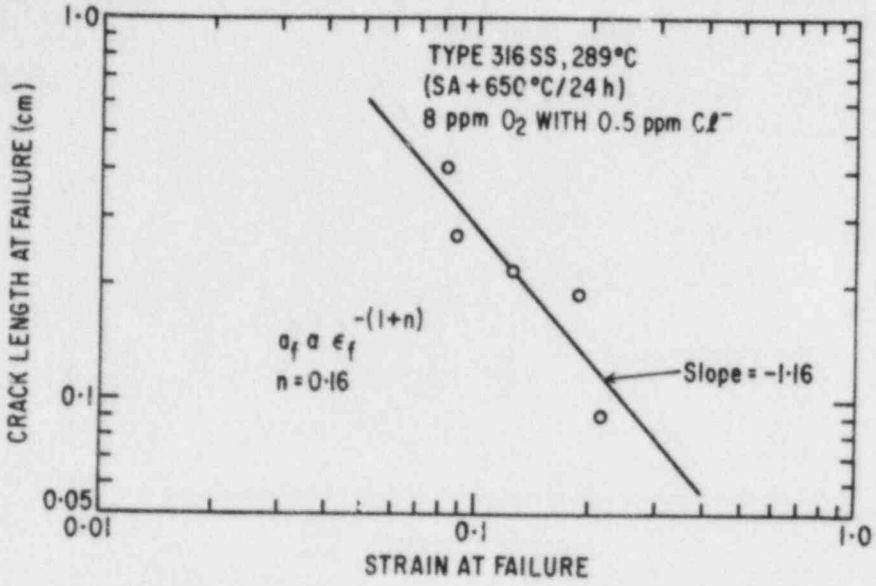

Fig. 34. Log-log Plot of Crack Length at Failure (a_f) versus Strain at Failure (ϵ_f).

of the least-squares fit of the data is 0.82), by a straight line with a slope equal to -1.16. From this slope, the value of n is found to be 0.16, which is in good agreement with the value determined from a true-stress/true-strain analysis of the data for large strains ($\epsilon \geq 9.0\%$). (The value of n = 0.16 is low compared to typical handbook values[25] of n = 0.4-0.5, which are descriptions of stress-strain behavior over a wide range of strains. However, n in Eq. (21) (and in Fig. 34), represents the value at large strains near fracture. Since n is small, Eq. (21) can be simplified to

$$J_c = C\epsilon_f a_f \ . \tag{22}$$

Equations (20) and (22) can be combined to derive correlations between the various IGSCC susceptibility parameters and the strain rate as follows:

$$\dot{a}_{av} = A(AC/J_c)^{1/3}\dot{\epsilon}^{1/3}, \tag{23}$$

$$t_f = (J_c/AC)^{2/3}\dot{\epsilon}^{-2/3}, \tag{24}$$

$$\epsilon_f = (J_c/AC)^{2/3}\dot{\epsilon}^{1/3}, \text{ and} \tag{25}$$

$$a_f = A(J_c/AC)^{1/3}\dot{\epsilon}^{-1/3}. \tag{26}$$

Good agreement is obtained between the results of the analysis and CERT test data over a fairly wide range of strain rates. For example, consider the correlation of $\dot{\varepsilon}$ with $\dot{a}_{av}$, a_f, and t_f. The log-log plots of $\dot{a}_{av}$ vs $\dot{\varepsilon}$, a_f vs $\dot{\varepsilon}$, and t_f vs $\dot{\varepsilon}$ yield straight lines with slopes that are in satisfactory agreement with the strain rate exponents described by Eqs. (23), (26), and (24), respectively (see Figs. 35-37). Figure 38 shows a log-log plot of time to failure versus strain rate for Types 316 and 304 SS (sensitized) in three different environments. The measured slopes ($\approx$-0.7) are in good agreement with that predicted by the model (see Eq. 24).

The limited experimental results reported in the literature also appear to be consistent with the present work. For example, Ford[22] has reported that $\dot{a}_{av} \propto \dot{\varepsilon}^{0.35}$ for Type 304 stainless steel in high-purity water containing 0.2 ppm O_2 and in water with 0.1M Na_2SO_4 at a temperature of $\sim$100°C. Also, from published[26] strain rate effects on uniform elongation for Type 304 stainless steel (sensitized at 600°C/24 h) tested in oxygenated water (8 ppm O_2 at 290°C), it can be shown that uniform strain $\propto \dot{\varepsilon}^{0.37}$.

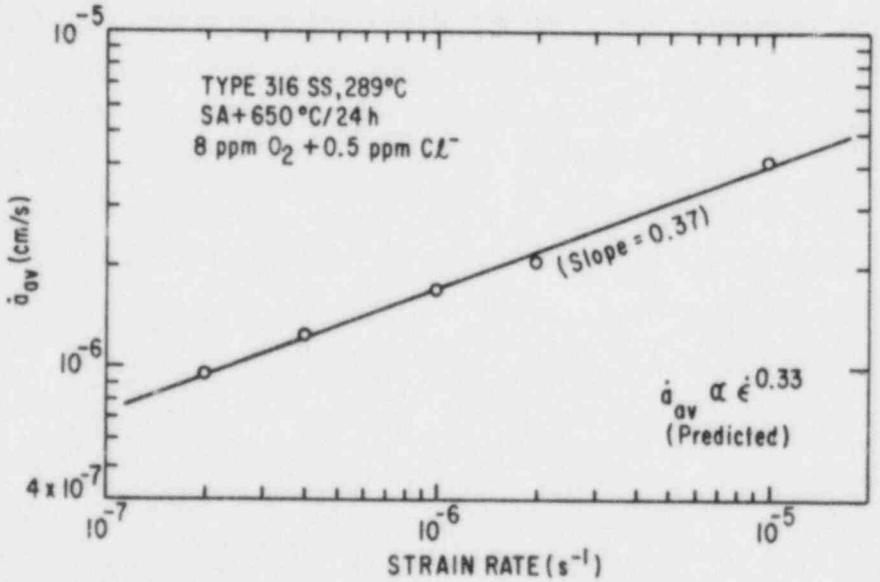

Fig. 35. Log-log Plot of Average Intergranular Crack Growth Rate ($\dot{a}_{av}$) versus Strain Rate ($\dot{\varepsilon}$).

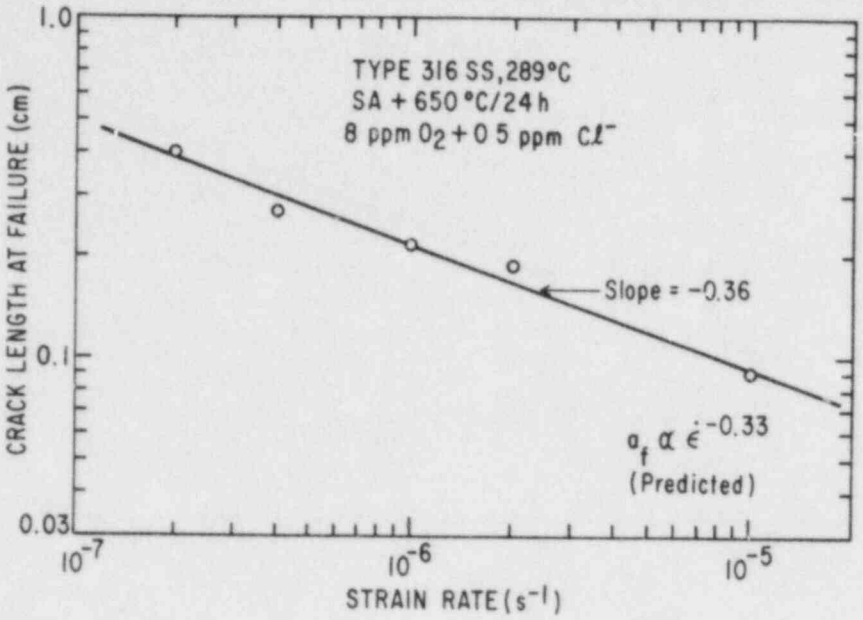

Fig. 36. Correlation between Crack Length at Failure (a_f) and Strain Rate ($\dot{\epsilon}$).

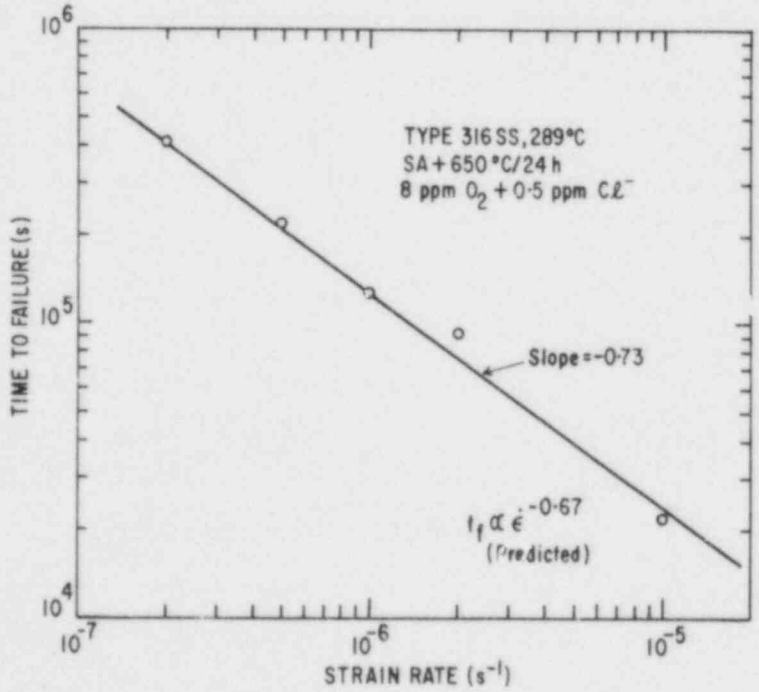

Fig. 37. Log-log Plot of Time to Failure versus Strain Rate.

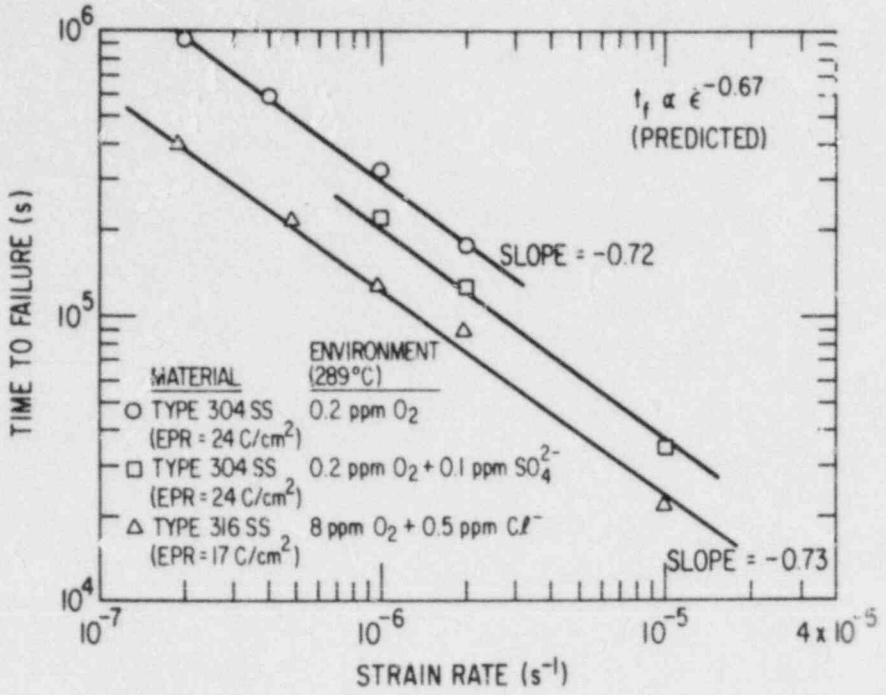

Fig. 38. A Plot of Time to Failure versus Strain Rate for Types 304 and 316 SS in Different BWR-related Environments.

The analysis of the effect of strain rate on IGSCC susceptibility embodied in Eqs. (23-26) thus appears to be applicable · a range of water chemistries that are of interest in BWRs. Furthermore, the good agreement between the predicted and the experimental results suggests that the approach provides a rational basis for extrapolating the results to the much slower strain rates ($\dot{\epsilon} \lesssim 10^{-8}$ s^{-1}) characteristic of operating BWRs.

Finally, it should be pointed out that the use of the J-integral to characterize fr re is difficult to rigorously justify a p or the large plastic deformations that occur in the CERT test. H , the results shown in Fig. 34, the value of the strain-hardening ex ermined from the fract re criterion, and the good agreement between the predicted and experimental results all indicate that it is a reasonable approximation.

The J-integral approach also appears to be promising in defining a crack-tip strain rate in CERT tests. Although the (nominal) strain rate is an appropriate parameter for characterizing CERT tests, correlation of $\dot{a}_{av}$ with the crack-tip strain rate $\dot{\epsilon}_T$ is more fundamental both from a mechanistic

viewpoint and from the viewpoint of understanding the effects of different types of loadings encountered in service on IGSCC susceptibility. Integration of Eq. (15) yields an expression for the average crack-tip strain rate $\bar{\dot{\varepsilon}}_T$,

$$\bar{\dot{\varepsilon}}_T = \frac{1}{t_f - t_o}\left[\ln\frac{\varepsilon_f}{\varepsilon_o} + \ln\frac{a_f}{a_o}\right], \tag{27}$$

where t_o, ε_o, and a_o are the time, strain, and crack length at the initiation of the crack, respectively, and the subscript f refers to values at failure. Following Ford,[22,23] we can write

$$\dot{a}_{av} = A_T(\bar{\dot{\varepsilon}}_T)^{0.5}, \tag{28}$$

which is similar to Eq. (13) deduced from the slip-dissolution model. A comparison of log-log plots of $\dot{a}_{av}$ versus $\bar{\dot{\varepsilon}}_T$ for different choices of crack initiation parameters shows that the average crack growth rate is proportional to the square root of the average crack-tip strain rate (see Fig. 39), which is consistent with Eq. (28). For example, for a_o = 1 μm and ε_o = 0.3%, we obtain $\dot{a} = A(\bar{\dot{\varepsilon}})^p$ cm/s with $A = 1.91 \times 10^{-4}$ and p = 0.51. Furthermore, as indicated in Fig. 38 the results are fairly insensitive to the choice of crack initiation parameters a_o and ε_o. In each case, the correlation coefficient for the least-squares fit of the data to the power law is 0.99. It can also be shown[27] that $\bar{\dot{\varepsilon}}_T \propto \dot{\varepsilon}^{2/3}$; over the range of strain rates used, $\bar{\dot{\varepsilon}}_T \simeq$ 50-150 $\dot{\varepsilon}$.

b. Stress/Strain/Strain-rate Relations for Sensitized Materials

The current mechanistic understanding of IGSCC suggests that in order to relate performance under laboratory loading histories (CERT tests, pipe tests, constant load tests, etc.) to the loading histories encountered under reactor operating conditions, it is necessary to be able to relate the strain rates produced by the different loading histories. Thus, a more detailed understanding of the stress/strain/strain-rate behavior for different thermomechanical states of Type 304 and 316 SS is needed. Stress relaxation experiments were carried out on Type 316 SS (Heat 0590019) and Type 304 SS (Heat 53319) to investigate the stress/strain rate behavior at temperatures between 28 and 289°C over a wide range of strain rates from $\sim 10^{-4}$-10^{-10} s^{-1}.

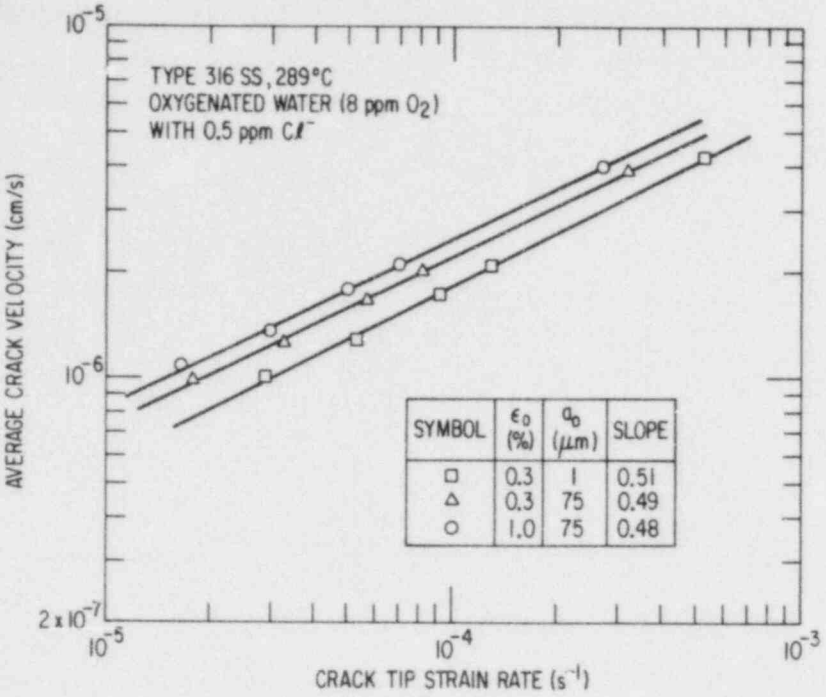

Fig. 39. Relationship between Average Intergranular Crack Growth Rate ($\dot{a}_{av}$) and Crack-tip Strain Rate ($\bar{\dot{\epsilon}}_T$) for Different Values of Crack Initiation Parameters. Average Crack-tip Strain Rate was Calculated Using Eq. (27).

Experiments on the materials in the as-received, solution annealed, and solution annealed and sensitized (600-650°C/24-50 h) conditions have been completed at 28°C and plans are underway to modify the system to obtain capability for measurements up to 300°C.

The stress relaxation data obtained at low temperatures (<350°C for stainless steels) can be described well by the state variable approach of Hart,[16] and the form of constitutive relations should not change significantly in the temperature range from 28-300°C. We will employ the stress relaxation data obtained from furnace-sensitized (1050°C/0.5 h + 650°C/50 h) specimens. This heat treatment is expected to produce an EPR value of >20 C/cm^2. The appropriate constitutive equation for describing the stress relaxation behavior at low temperatures involves only the glide friction element and is given by[16]

$$\dot{\epsilon} = \dot{a}^* \, (\sigma_f/G)^M \tag{29}$$

or

$$\sigma = \sigma^* + (G^M/\dot{a}^*)^{1/M} \, (\dot{\epsilon})^{1/M} , \tag{30}$$

where $\dot{\epsilon}$ is the nonelastic strain rate, $\dot{a}^*$ is the glide friction rate parameter, σ is the stress, σ^* is the hardness, $\sigma_f = \sigma - \sigma^*$, G is the shear modulus, and M is the material constant. As shown in Fig. 40, the data obtained from the load relaxation test at 28°C for the solution-annealed and aged Type 316 SS with initial stress equal to 1.1 σ_y (where σ_y is the yield stress of the material in the as-received condition) can be described fairly well by Eq. (30). The curve exhibits the concave-upward shape that is characteristic of low temperatures (i.e., less than half the melting temperature). It is found that the stress/strain-rate data obtained with initial stresses higher than 1.1 σ_y (i.e., 1.2 σ_y, 1.3 σ_y, 1.4 σ_y, and 1.5 σ_y) can also be described by Eqs. (29) or (30). Correlation of all the data to the constitutive Eq. (30) showed that values of σ^* for various initial stresses varied significantly, as expected. The coefficient $(G^M/\dot{a}^*)^{1/M}$ varied and 1/M was approximately constant. The data were then reanalyzed using an average value of 117.8 for $(G^M/\dot{a}^*)^{1/M}$ (G is in MPa, $\dot{a}^*$ is in s^{-1}) and an average value of 0.0715 for 1/M. The effect of the initial stress was taken into account through a single parameter, σ^*. As can be seen in Fig. 41, the stress relaxation plots (ln σ vs ln $\dot{\epsilon}$) yielded very good descriptions of the data for the initial stresses 1.1 σ_y (ϵ = 1.77%), 1.2 σ_y (ϵ = 2.91%), 1.3 σ_y (ϵ = 3.79%), 1.4 σ_y (ϵ = 5.8%), and 1.5 σ_y (ϵ = 7.38%), where ϵ is the nonelastic strain corresponding to the initial stress at the start of relaxation. The values of the hardness parameter σ^* determined by using average values of $(G^M/\dot{a}^*)^{1/M}$ and 1/M are shown in Table IX.

One of the unique properties of Hart's models[16,28] is the stress/strain-rate scaling of hardness curves generated at all levels of hardness. The existence of this scaling behavior has been tested for the present data. It was found that any curve plotted as ln σ vs ln $\dot{\epsilon}$ could be translated (without rotation) so that it would coincide (with very good precision) with the overlapping segment of any other hardness curve. Thus

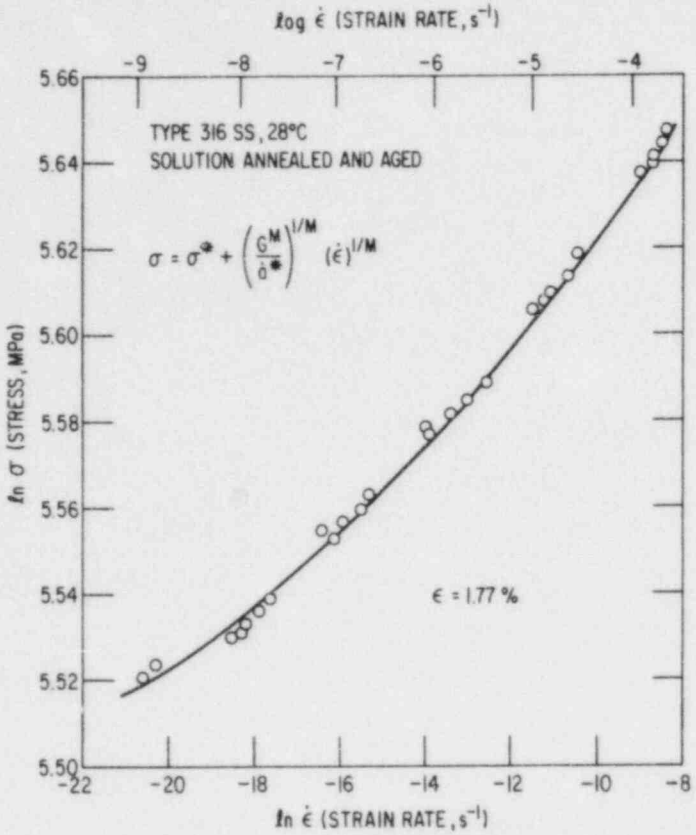

Fig. 40. Experimental Load Relaxation Data (Circles) for Type 316 SS with Initial Stress = 1.1 σ_y, and Fit (Solid Curve) Obtained by the Application of Hart's State Variable Approach.

Table IX. Hardness Parameter σ^* (see Eq. 30) Obtained for Type 316 SS at 28°C in Stress Relaxation Experiments. Heat treatment: 1050°C/0.5 h + 650°C/50 h

Initial Stress[a]	Non-elastic Strain, %	σ^*, MPa
1.1 σ_y	1.77-1.85	221
1.2 σ_y	2.91-2.99	249
1.3 σ_y	3.79-3.86	279
1.4 σ_y	5.80-5.87	309
1.5 σ_y	7.38-7.47	341

[a] σ_y = 255 MPa.

there exists a master hardness curve which could be used to generate all the observed curves by rigid translation of the master curve in a single direction. The direction of the translation is determined by a line connecting points that correspond to the same slope on different hardness curves. In other words, the intersections of the translation line with the stress relaxation curves belonging to different hardness levels satisfy the relationship

$$\left(\frac{\delta \ln \sigma}{\delta \ln \dot{\varepsilon}}\right)_{\sigma_1^*} = \left(\frac{\delta \ln \sigma}{\delta \ln \dot{\varepsilon}}\right)_{\sigma_2^*} = \left(\frac{\delta \ln \sigma}{\delta \ln \dot{\varepsilon}}\right)_{\sigma_i^*}, \tag{31}$$

where σ_i^* is the hardness parameter of the ith curve. The slope of the translation line is equal to the strain rate exponent 1/M of Eq. (30). The translation line so determined, shown in Fig. 41, has a slope of 0.0715. The validity of the scaling law is demonstrated in Fig. 42, which is produced by translating all the curves in Fig. 41 along the indicated straight line onto the lowest curve (the lowest curve corresponds to the curve obtained with an initial stress of 1.1 σ_y). The validity of such a scaling law has been demonstrated previously by Yamada and Li.[28] This scaling behavior suggests that the curves in Fig. 41 belong to a one-parameter family of curves with hardness as the parameter.

Somewhat more accurate values for å* and σ* can be determined from a master plot of σ versus $\dot{\varepsilon}^{1/M}$ (1/M = 0.0715), shown in Fig. 43. This relation, as suggested by Eq. (30), is nearly linear. A least-squares fit yields σ* = 221 MPa and $(G^M/å^*)^{1/M}$ = 117.

Further experiments on the material at different temperatures and subjected to different thermomechanical treatments (e.g., cold work and heat treatments, IHSI) will furnish information on the amount of stress relaxation that can result in materials with different susceptibilities to SCC. Furthermore, the approach provides a phenomenological basis to determine the plastic strain rates produced by applying the same load to specimens with different hardness parameters.

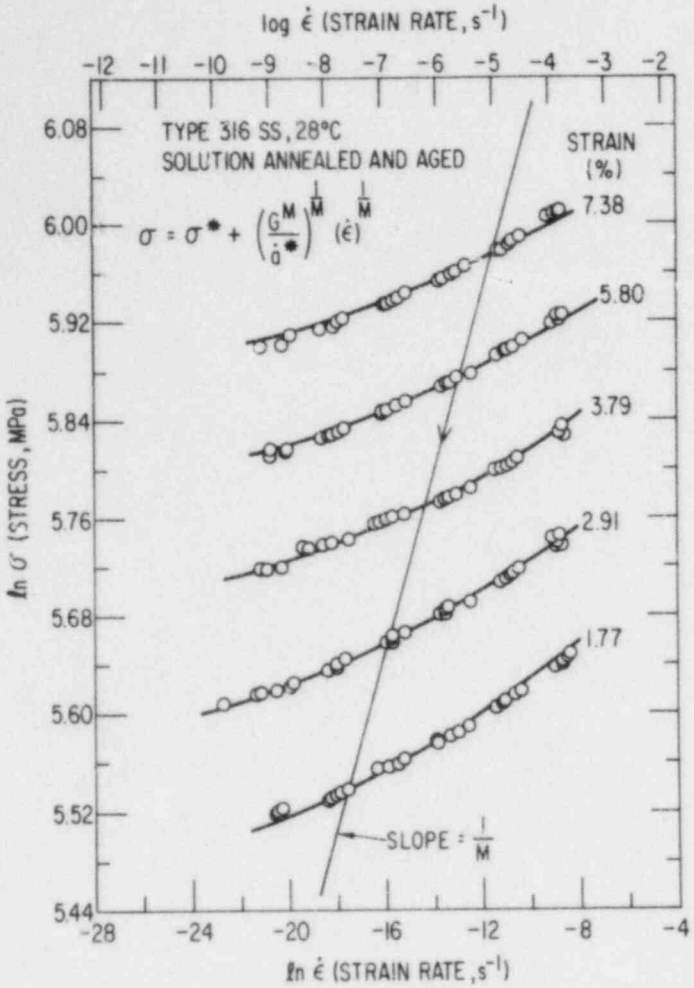

Fig. 41

Stress Relaxation Data (Circles) and Predictions (Solid Curves) Based on Eq. (30) in the Text. The diagonal line represents the analytically determined scaling direction.

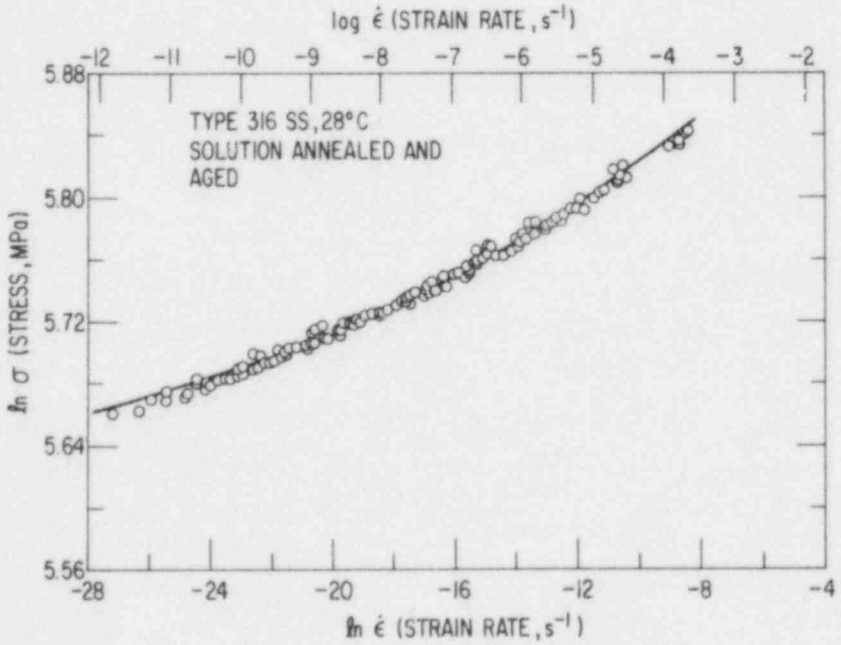

Fig. 42. A Master Hardness Curve for Type 316 SS.

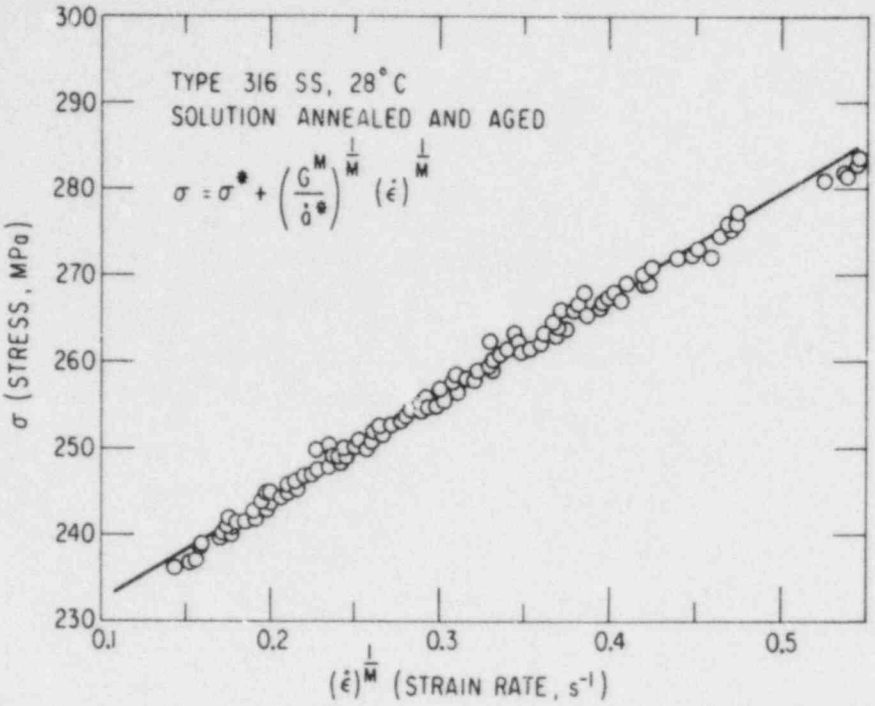

Fig. 43. Master Plot of σ vs $\dot{\epsilon}^{1/M}$ (1/M = 0.0715).

The data can also be described fairly well by a slightly modified version of the constitutive equations proposed by Miller[29] although the state variable approach of Hart[16] gave better agreement. One of the significant differences between the two approaches lies in the choice of the structure parameter, the state variable approach uses hardness parameter σ* and the creep-law of Miller uses the non-elastic strain ϵ_n as the structure variable. This is simply illustrated as follows: the Miller's method (based on a creep law) predicts the non-elastic strain rate $\dot{\epsilon}_{in}$ as a function of temperature T, the applied stress σ and the current level of non-elastic strain itself, i.e.

$$\dot{\epsilon}_n = f(T) \quad g(\sigma, \epsilon_{in}) \ . \tag{32}$$

On the other hand, the state variable approach describes

$$\dot{\epsilon}_n = h(\sigma, \sigma_*, \dot{a}_*) \ , \tag{33}$$

where $\dot{a}_*$ is the friction rate parameter which is temperature dependent. Although, conceptually σ_* is a better parameter for describing the loading history effects than ε_n, it is not always easy to determine σ_* in many practical situations. Furthermore there exists more extensive discussions concerning the application of Miller's equation to determine $\dot{\varepsilon}$ from loading histories of interest to BWR applications. Therefore, we propose to rewrite Hart's equation in a form that contains the essential ingredients of Miller's creep law in the following manner. Equation (33) can be rewritten as

$$\dot{\varepsilon}_n = h(\sigma, \varepsilon_n, \dot{a}_*) \ , \tag{34}$$

where σ_* has been replaced by ε_n. If the temperature dependence is contained in $\dot{a}_*$ (i.e., for example, $\dot{a}_* = \dot{a}_o^* \exp(-\Delta H/RT)$ where ΔH is an activation energy whose physical significance remains to be identified), Eq. (34) in essence contains the ingredients of Miller's equation. Specifically, using the data obtained for Type 316 stainless steel at 28°C, we have shown that the following constitutive equation

$$\dot{\varepsilon} = \dot{a}_* \left(\frac{\sigma - \sigma_*}{G} \right)^M \tag{35}$$

describes the data fairly well. It is observed that σ^* and ε_n are related by a power law

$$s_* = B(\varepsilon_n)^\beta \tag{36}$$

as shown in Fig. 44 with B = 714 MPa and β = 0.3. Thus Eq. (35) becomes

$$\dot{\varepsilon} = \dot{a}^* (T) \left[\frac{\sigma - B(\varepsilon_n)^\beta}{G} \right]^M \ , \tag{37}$$

in which M is shown to be equal to 14. If the strain rate effects on work hardening can be ignored at temperatures between 28 and 300°C, Eq. (37) (NOTE: Eqs. (35) and (37) are interchangeable) represents a useful constitutive equation for investigating the loading history effects on IGSCC.

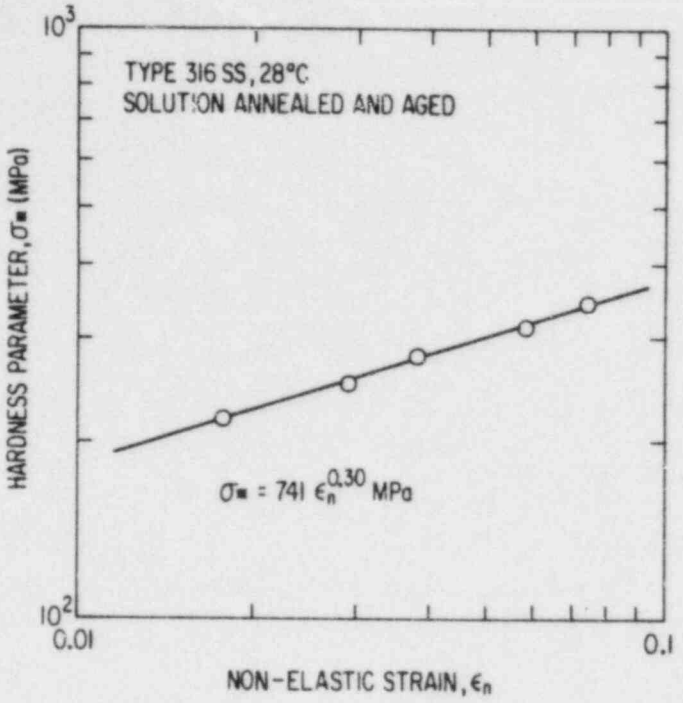

Fig. 44. Relationship between Hardness Parameter and Non-elastic Strain.

c. Finite Element Analyses of Flawed Weldments with IHSI and Weld Overlays

Residual stress improvement remedies such as IHSI and weld overlay techniques have been proposed as both long- and short-term remedies. Research work on the effectiveness of IHSI on unflawed weldments has been carried out in both the U.S. and Japan.[31,32] Much more limited information is available on the effectiveness of IHSI on flawed weldments, especially on flawed weldments subject to applied loads. In the pipe testing program weldments with initial defects did not show any significant benefit of the IHSI process even for relatively shallow (<10% throughwall) precracks.[31] This has been attributed to the relatively high loads in the pipe test, and it is argued that with actual plant loads a significant benefit is likely for the shallow cracks that might escape detection.[32] Similarly, a number of calculations have been carried out to demonstrate the effectiveness of the weld overlay procedure in producing compressive residual stresses in the heat affected zone, but most of these calculations have been done for uncracked weldments.[33] Finite elements calculations have been carried out under

subcontract to E. F. Rybicki, Inc. to try to quantify the range of crack sizes and applied loads for which the IHSI and the weld overlay technique may be effective.

In the case of IHSI, calculations were performed for a 24-in. Schedule 80 weldment with preexisting flaws ∿8% throughwall, which is representative of a flaw that has a low probability of detection during an in-service inspection, and for a 12-in. Schedule 80 weldment with preexisting flaws ∿40% throughwall. The model assumes axisymmetry and symmetry across the weld centerline. At a distance of 5.4 mm (0.25 in.) from the centerline of the weld, the finite element grid was refined to permit a crack to be introduced (actually two cracks due to the assumed symmetry across the weld centerline). Double nodes were used along the intended path of the crack to permit crack growth simulation. Before the crack is present, the nodes are coupled. To simulate crack growth, the nodes are uncoupled one pair at a time.

The first steps in the calculation model the butt welding process. This weld consists of seven weld layers, and the welding parameters are summarized in Table X. The weld metal and the pipe are modeled as an elastic-plastic material with temperature dependent mechanical properties. A more detailed description of the modeling of the welding process is given in Ref. 34.

The next stage of the calculation involves growing the crack. This was done in a step-wise fashion by releasing the double nodes along the crack plane, and then checking the stress state ahead of the crack. The crack was allowed to grow until the crack tip encounters a compressive, crack-plane-normal (axial) stress.

The stress state ahead of the crack was examined as a function of applied load both for the case without IHSI and with IHSI. The IHSI process was again modeled in terms of a temperature dependent elastic-plastic material. The temperature profile in the pipe during IHSI was obtained using a lumped circuit parameter model of coil and pipe to determine the heat generation profile, and then using a standard finite element program to find

Table X. Welding Parameters for the Simulated Seven Layer Girth Weld

Layer	Current, Amps	Voltage, Volts	Travel Speed, in/min	Heat Input (at 75%),[a] Btu/s	Interpass Temp., °F
1	130	9	2	0.83	70
2	180	9	3	1.15	100
3	90	24	3	1.54	150
4	115	26	4	2.13	150
5	115	26	4	2.13	250
6	115	26	4	2.13	250
7	95	23	4	1.56	250

[a]Thermal conductivity = 0.00026 Btu/in-s-°F, volume heat capacity = 0.036 Btu/in^3-°F.

the resulting temperature distributions. These distributions were then used as input to the elastic-plastic analysis. A detailed description of the modeling process is given in Ref. 35.

For the pipe with the ∿8% throughwall crack the distributions of stress ahead of the crack tip under an applied stress of 103 MPa (15 ksi) in weldments with and without IHSI are shown in Fig. 45. Without IHSI, high tensile stresses [∿310 MPa (45 ksi)] are present ahead of the crack tip; with IHSI, the stresses ahead of the crack tip under this rather high applied load are not compressive, but they are quite low [∿35 MPa (5 ksi)]. The crack opening displacements and the stresses ahead of the crack tip after IHSI for the 12-in. Schedule 80 weldment with a ∿40% throughwall flaw with applied loads corresponding to internal pressure [∿41 MPa (6 ksi)], 52 MPa (9 ksi), and 103 MPa (15 ksi) are shown in Fig. 46. Even for this rather deep crack the crack tip is contained in a compressive stress field under typical applied loads, although it would be subject to tensile stresses at highly stressed joints.

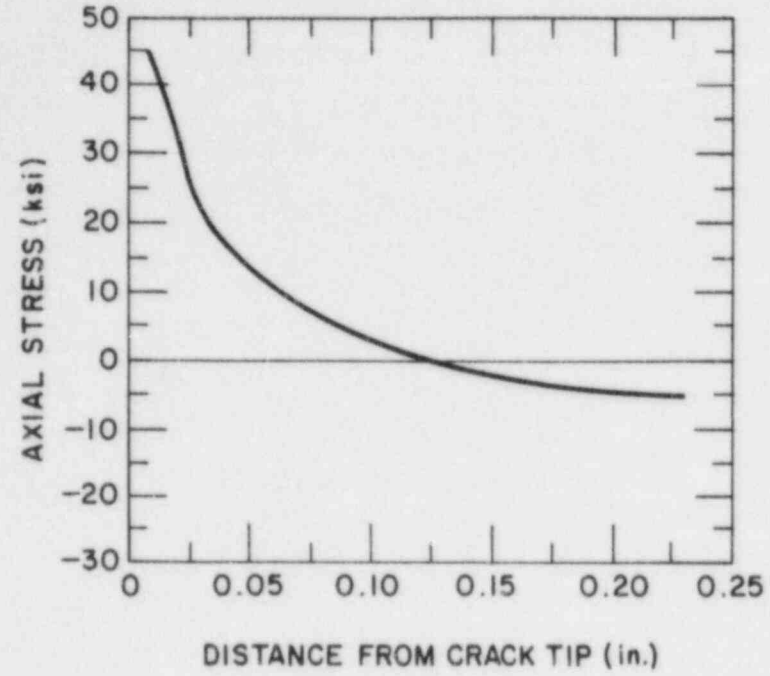

Normal stresses on crack plane with 15 ksi applied stress without IHSI

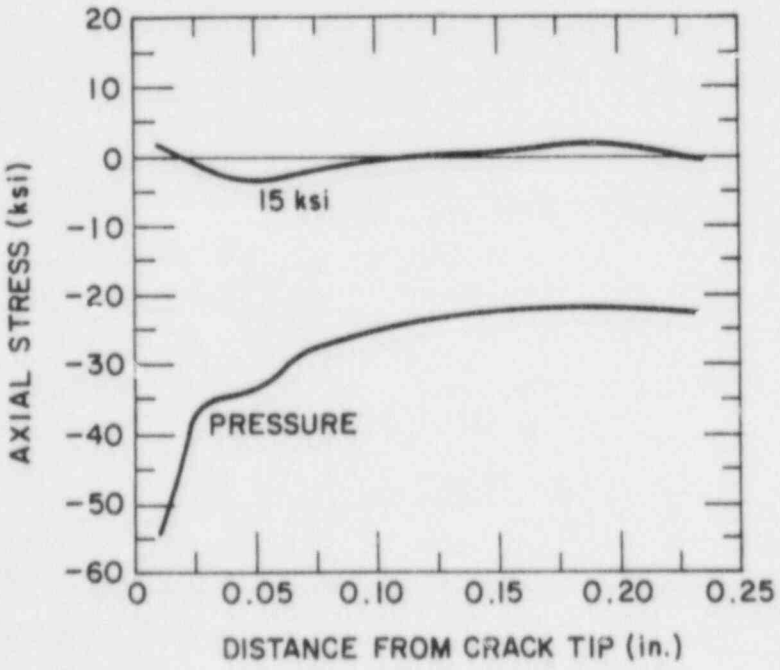

Normal stresses on crack plane after IHSI

Fig. 45. Calculated Stress State Ahead of the Tip of an ~8% Throughwall Crack under an Applied Load of 103 MPa (15 ksi) for a Weldment without IHSI (Top) and a Weldment with IHSI (Bottom).

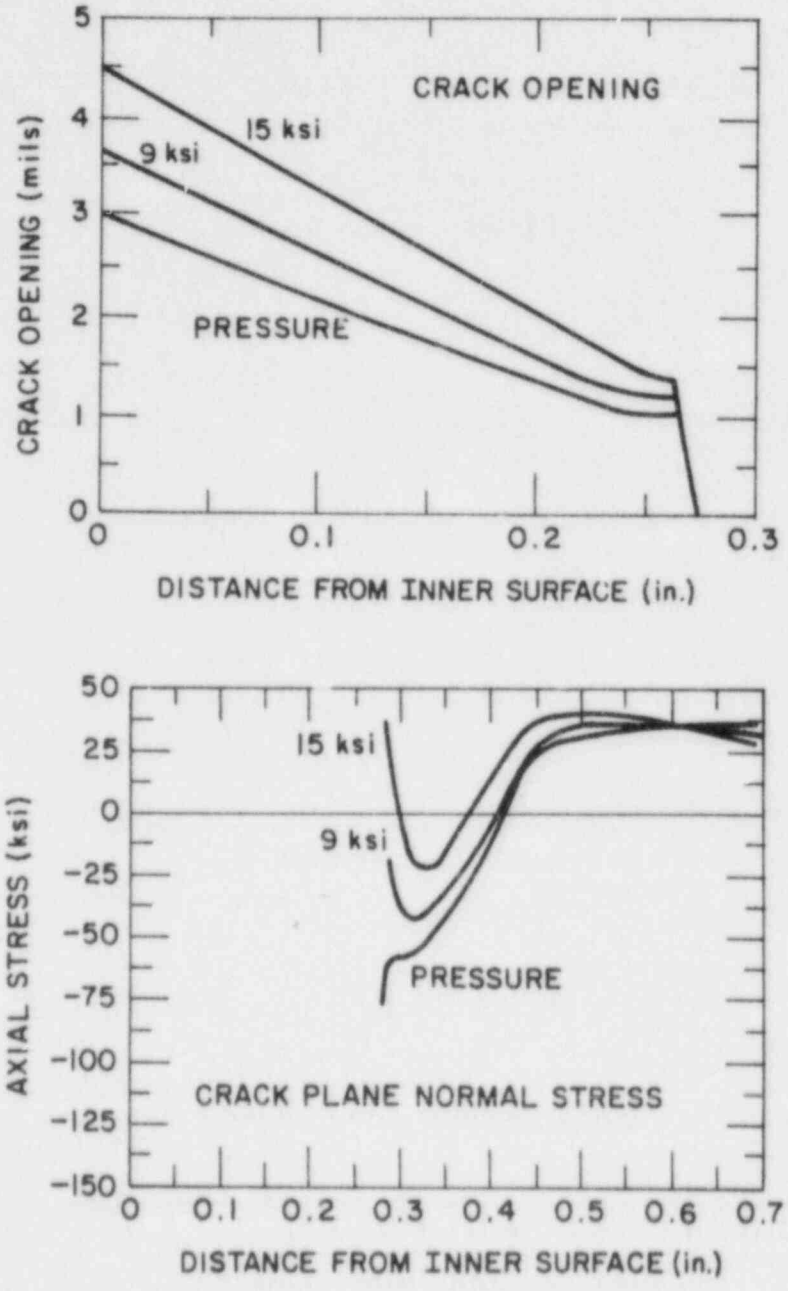

Fig. 46. Crack Opening Displacements and Axial Stresses Ahead of the Crack Tip after IHSI for a 12-in. Schedule 80 Pipe Weldment with ∿40% Throughwall Flaws.

The calculations for the weld overlays were carried out for 12-in. Schedule 80 pipe weldments. An axisymmetric finite element model with additional symmetry across the weld centerline was again used. Two cases were considered. In the first case the weld was assumed to have a preexisting circumferential crack on each side of the weld. The cracks are 4.3 mm from the weld centerline and 3.5 mm deep (20% throughwall). Both the girth weld and the overlay were simulated, although it appears that the stresses due to the overlay completely dominate the original residual stresses due to the initial welding process. The assumption of symmetry across the weld centerline implies that the overlay is deposited symmetrically about the weld centerline. This is not the case, but it is felt that the additional idealization does not greatly distort the results. In the second case a single crack, 10.5 mm deep (60% throughwall), was assumed, but to maintain symmetry the crack was located at the weld centerline. This is, of course, unlikely to occur for metallurgical reasons, but the idealization should not greatly affect the stress state at the crack tip.

During applications of IHSI and the weld overlay process the calculated crack opening displacements at the crack tip are small [<0.2 mm (<8 mils)] for the cracks considered. Stainless steel crack tip opening displacements of this magnitude will not produce crack extension, and hence, these calculations indicate that unless the cracks are very deep initially, they are unlikely to extend during the application of the remedies.

The axial residual stresses on the inner surface and the stresses on the crack plane ahead of the crack after weld overlay of the 12-in. pipe with a 20% throughwall crack are shown in Fig. 47. The stresses on the crack plane and the crack opening displacements for the 60% throughwall flaw are shown in Fig. 48 for an applied axial stress of 62 MPa (9 ksi). The complex pattern of the crack opening displacement indicates the intense deformation at the crack tip produced by the weld overlay. At this applied load, which is typical for actual reactor piping of this size, the stresses ahead of the crack are still compressive. The corresponding displacements and stresses for an applied stress of 103 MPa (15 ksi) are shown in Fig. 49. The crack tip is now in a tensile stress field, and the crack is completely open.

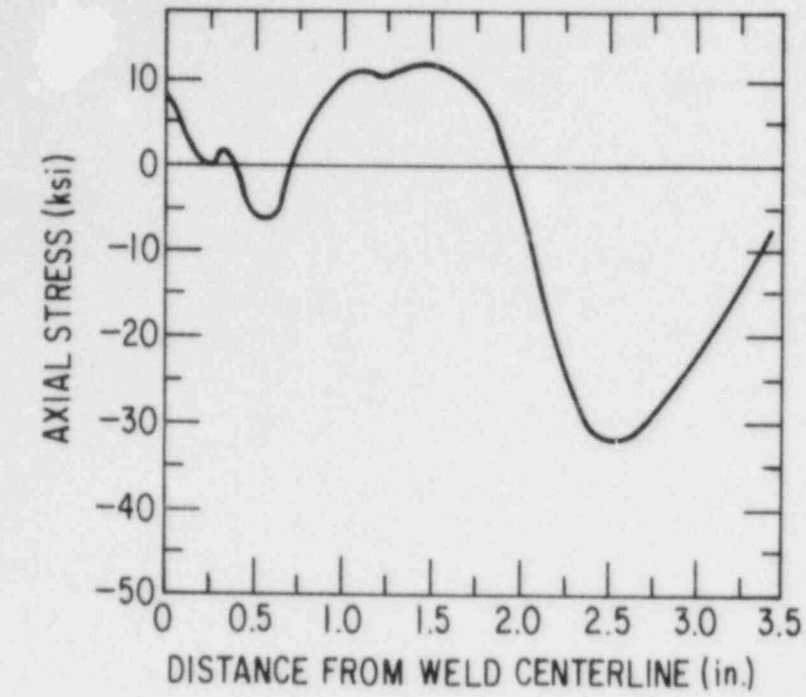

(a) Total Stress on Pipe ID with Weld Overlay and 15 ksi Applied Stress

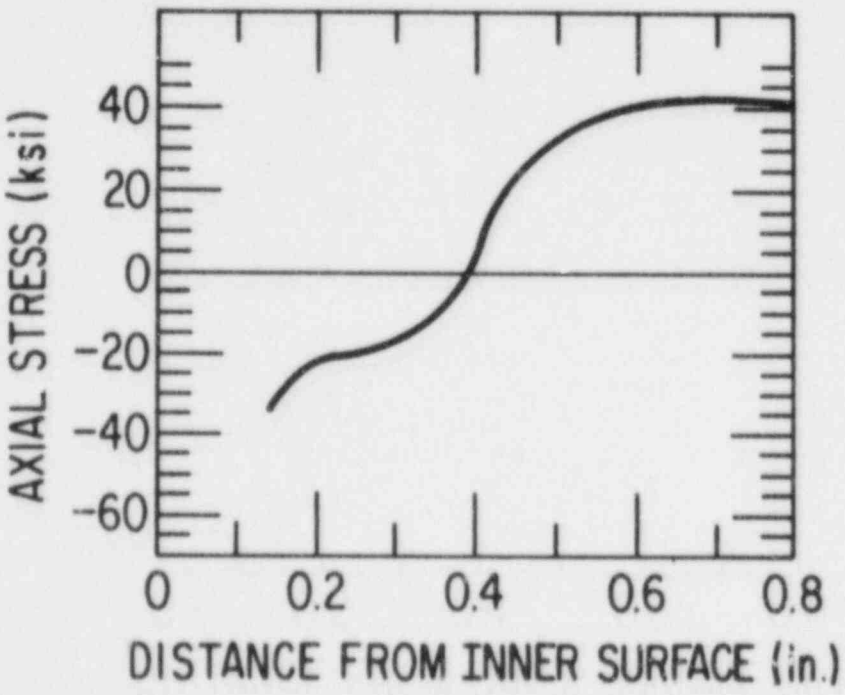

(b) Stresses Ahead of Crack Tip with 15 ksi Applied Stress

Fig. 47. Residual Stresses after Weld Overlay for a 12-in. Pipe with a 20% Throughwall Flaw. (a) Total axial stress on the inner surface with 103 MPa (15 ksi) applied stress; (b) stresses on the crack plane ahead of the crack tip with 103 MPa (15 ksi) applied stress.

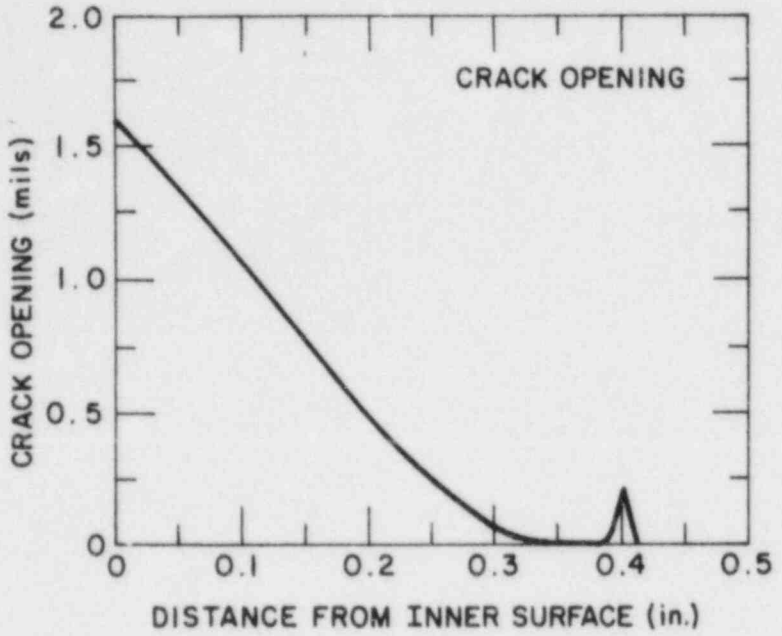

(a)

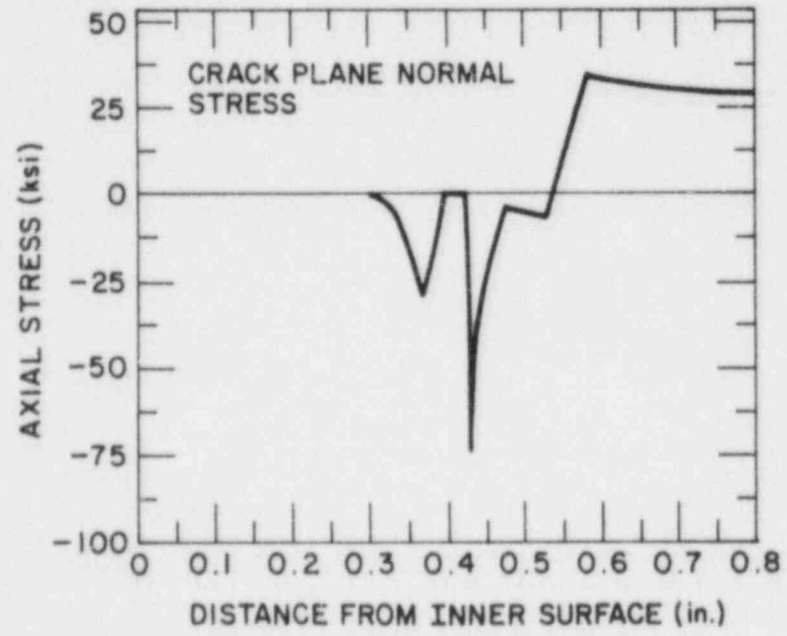

(b)

Fig. 48. (a) Crack Opening Displacement and (b) Normal Stress on the Crack Plane with 62 MPa (9 ksi) Applied Stress for the Pipe with a 60% Throughwall Flaw after Weld Overlay.

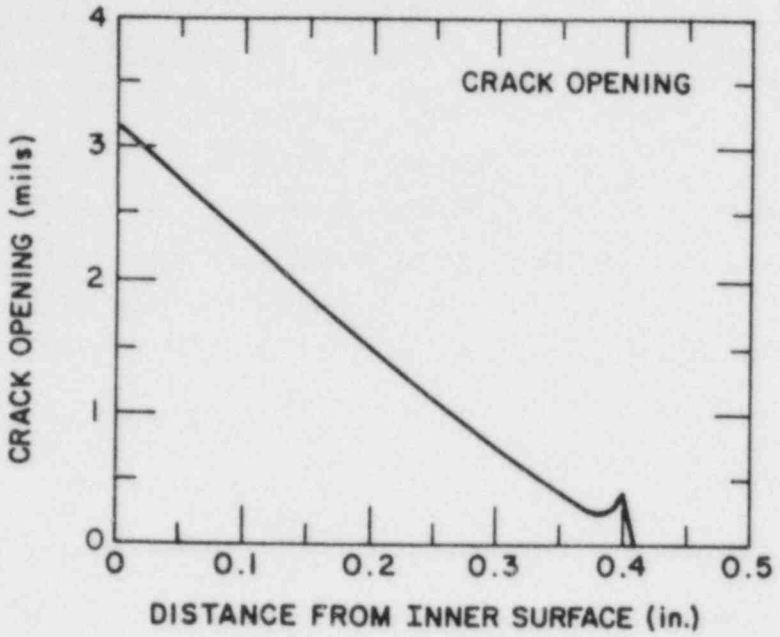

(a)

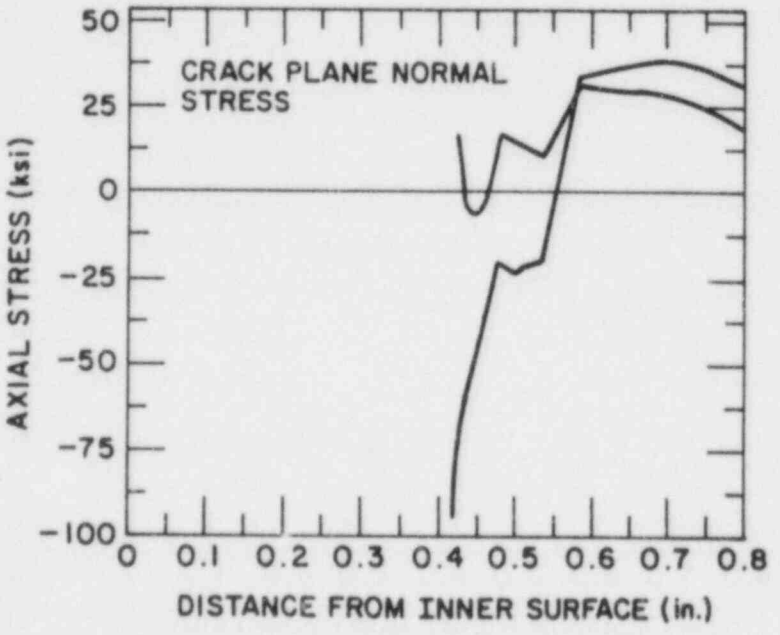

(b)

Fig. 49. (a) Crack Opening Displacement and (b) Normal Stress on the Crack Plane with 103 MPa (15 ksi) Applied Stress for the Pipe with a 60% Throughwall Flaw after Weld Overlay.

These calculations suggest that the weld overlay is effective in producing a favorable (compressive) residual stress state at the crack tip even for deep, 360° cracks. Similarly the calculations for IHSI indicate that for realistic stress levels the process produces favorable residual stresses even for weldments with significant cracking. These limited calculations cannot completely define the range of crack depths and applied loads for which these remedies can be expected to be effective, and additional calculations are planned to compare the results of the finite element calculations presented here with the results of the somewhat simpler analyses typically used in the design and assessment of weldments that have been treated by IHSI or weld overlay.

d. Margin for Leak-Before-Break of Flawed Piping

Analyses of the remaining lifetime of cracked pipe are subject to significant degrees of uncertainty. If worst case assumptions are made for the initial crack sizes, crack growth rates, and residual stress distributions, the predicted behavior (rapid, throughwall growth of small aspect ratio cracks) is not consistent with field experience or laboratory studies on large diameter piping. If "typical" values are used for the crack growth rates and residual stresses, the predicted behavior appears much more consistent with field experience. However, the residual stress pattern in a given weldment cannot be determined nondestructively, and the crack growth rate of a particular heat of material cannot a priori be shown to be "typical". Even the conservative assumptions on residual stress and crack growth rate used by NRR in assessing the remaining lifetime may be unconservative in a particular case. However, further assurance that neither the cracks that were detected and repaired nor the cracks that were not detected are likely to cause a serious loss of coolant during reactor operation can be obtained by demonstration of a significant margin for leak-before-break (LBB).

The inherent toughness of Type 304 stainless steel generally leads to LBB behavior and few, if any, sudden, catastrophic failures have been associated with its use not only in the nuclear industry but also in a wide variety of other industries. However, IGSCCs in large diameter

weldments are characterized by large aspect ratios, and the possibility that cracking will occur 360° around the circumference before a throughwall crack develops must be considered.

Unless IGSCC growth is arrested by a favorable residual stress distribution, failure of the piping system could occur by continued growth of the crack by stress corrosion without the necessity for postulating loads on the piping beyond the normal operating and upset loads. A meaningful LBB margin requires that detectable leakage occur from a cracked pipe before the pipe experiences rapid crack growth and final failure due to mechanical loading leading to a large loss of coolant.

The determination of this margin requires an analysis of the failure behavior of the pipe for a particular crack geometry, and calculation of the crack opening area and flow through the crack. In the results presented here the failure of the cracked pipe is assumed to be adequately described by a net section stress approach similar to that used in IWB3640.[36] Most welds in BWR piping systems are probably tough enough for this assumption to be valid. The calculation of the leak rate through the crack is also subject to considerable uncertainty. The crack opening area has been estimated on the basis of elastic solutions for a throughwall crack in an infinite plate with an approximate correction for plasticity effects based on the Dugdale model.[37] More complete elastic-plastic solutions for the crack opening area suggest that this solution is conservative.[38]

The flow of steam-water mixtures through tight cracks is a complex function of crack geometry, crack surface roughness, and temperature and pressure. Limited experimental measurements of the fluid flux through IGSCC and simulated cracks have been carried out.[39,40] Comparisons of this data with the flow predicted by the homogeneous critical flow model developed by Henry[1] indicate that the actual flux is from 1 to 0.1 of the corresponding frictionless flux predicted by the Henry model. Although models which attempt to account for the frictional losses have been developed,[41] the limited data base and the uncertainty about the internal crack geometry, corrosion product deposition, and roughness make it difficult to predict accurately the flow through an IGSCC.

This uncertainty has surprisingly little effect on the assessment of the LBB margin in piping. Figure 50 shows a typical case for a 10-in. pipe. It is assumed that the crack can grow completely around the pipe circumference before a throughwall crack occurs. The collapse curve in Fig. 50 assumes that the net section stress at failure equals 3 S_m. The observed variations in flux are used to estimate upper and lower bounds on the crack sizes necessary to obtain a 5 gal/min leak rate. Based on crack size there is a significant margin unless the circumferential crack is quite deep. Because of the steep nature of the collapse curve for deep circumferential cracks, the size of the crack that can be postulated before violation of LBB is not very dependent on the value chosen for the fluid flux. The corresponding case for a 24-in. pipe is shown in Fig. 51. The size of the crack needed to obtain detectable leakage is only very weakly dependent on pipe diameter, while the size of the crack needed to produce collapse is roughly proportional to pipe diameter. Hence the margin for LBB generally increases with pipe size. As Figs. 52 and 53 show, however, the LBB margins are smaller at highly stressed joints.

Estimates of the time from the onset of unallowable leakage to structure failure depend strongly on the mechanism of crack growth and the corresponding crack growth rate assumptions. In most cases, much of the remaining crack growth will occur by stress corrosion. Figure 54 summarizes the available data on IGSCC growth rates in BWR-type environments; i.e., both data from fracture mechanics tests under controlled load, and from slow-strain-rate tests in which the load is varied to maintain a constant the nominal strain rate. It is unlikely that the strain rates commonly used in slow strain tests can be maintained under reactor loading conditions, and therefore an upper bound for in-reactor loading based on growth rates in these tests should be very conservative. The crack growth curve selected in Fig. 54 bounds all available fracture mechanics data (the plateau rate is ten times the highest reported rate in a constant load fracture mechanics test), and the plateau rate is typical of slow strain rate tests.

Using this crack growth rate curve and the usual linear elastic-fracture-mechanics approach, the time from the onset of leakage to failure can be estimated for different crack geometries. For simple throughwall

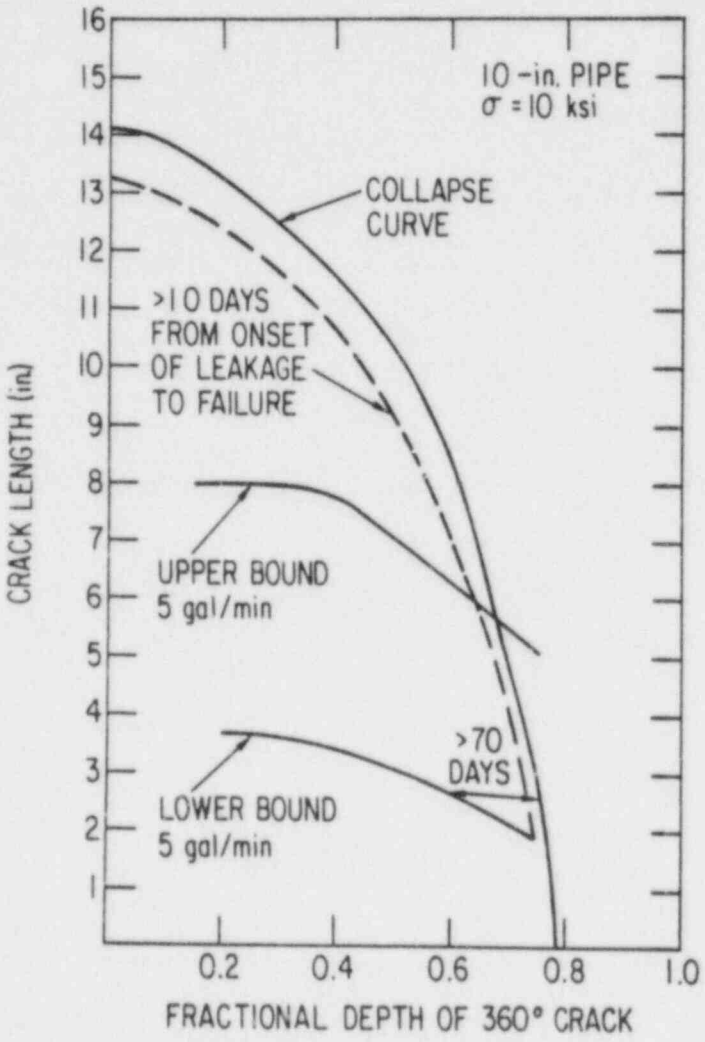

Fig. 50. Collapse Curve for a 10-in. Pipe with Throughwall and Part-through 360° Cracks with Bounds for Crack Sizes for 5 gal/min Leak Rate under an Applied Stress of 10 ksi.

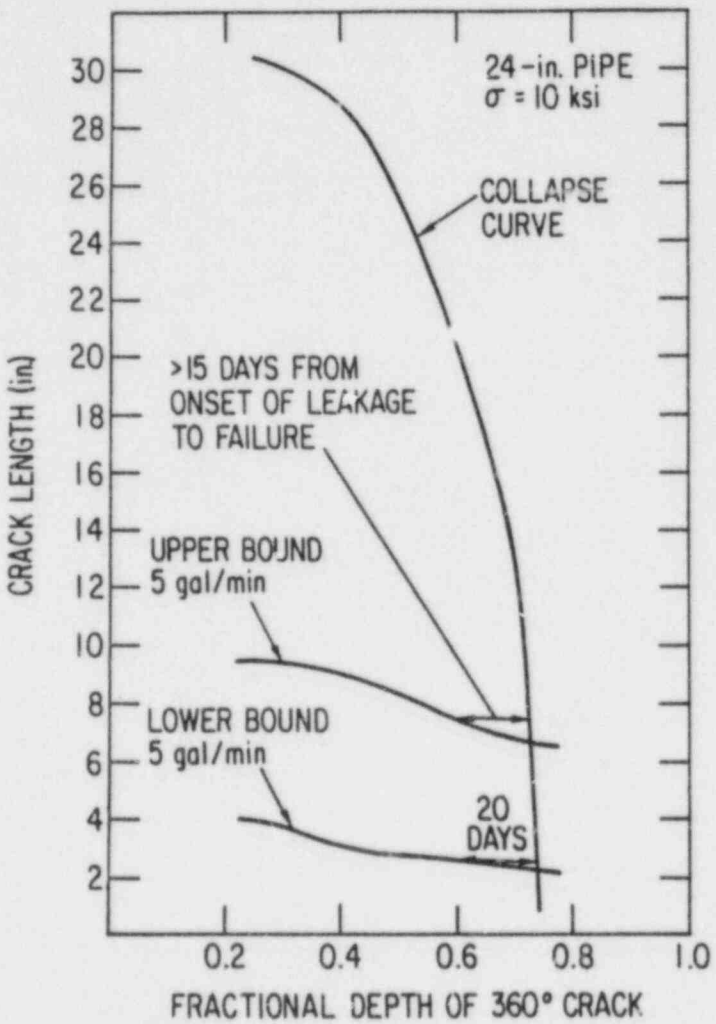

Fig. 51. Collapse Curve for a 24-in. Pipe with Throughwall and Part-through 360° Cracks with Bounds for Crack Sizes for 5 gal/min Leak Rate under an Applied Stress of 10 ksi.

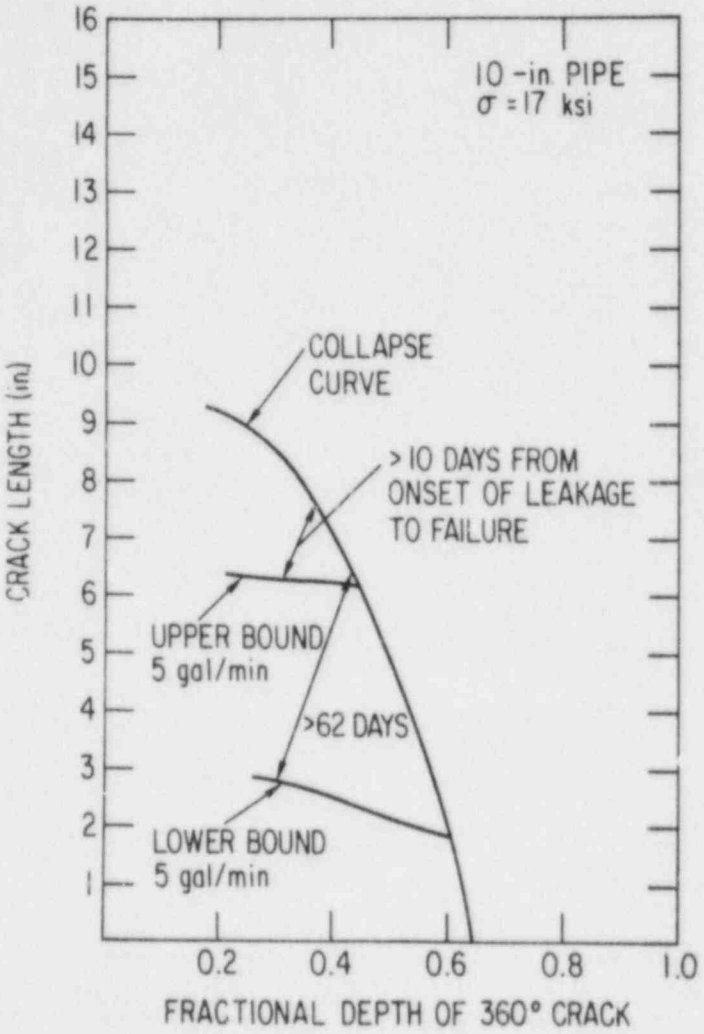

Fig. 52. Collapse Curve for a 10-in. Pipe with Throughwall and Part-through 360° Cracks with Bounds for Crack Sizes for 5 gal/min Leak Rate under an Applied Stress of 17 ksi.

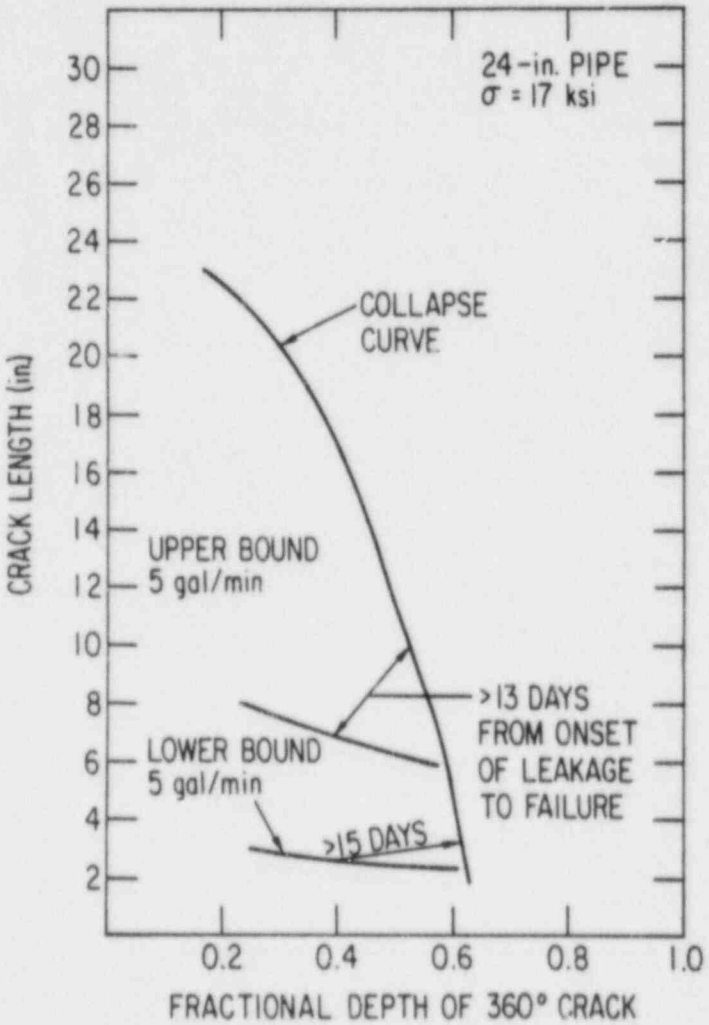

Fig. 53. Collapse Curve for a 24-in. Pipe with Throughwall and Part-through 360° Cracks with Bounds for Crack Sizes for 5 gal/min Leak Rate under an Applied Stress of 17 ksi.

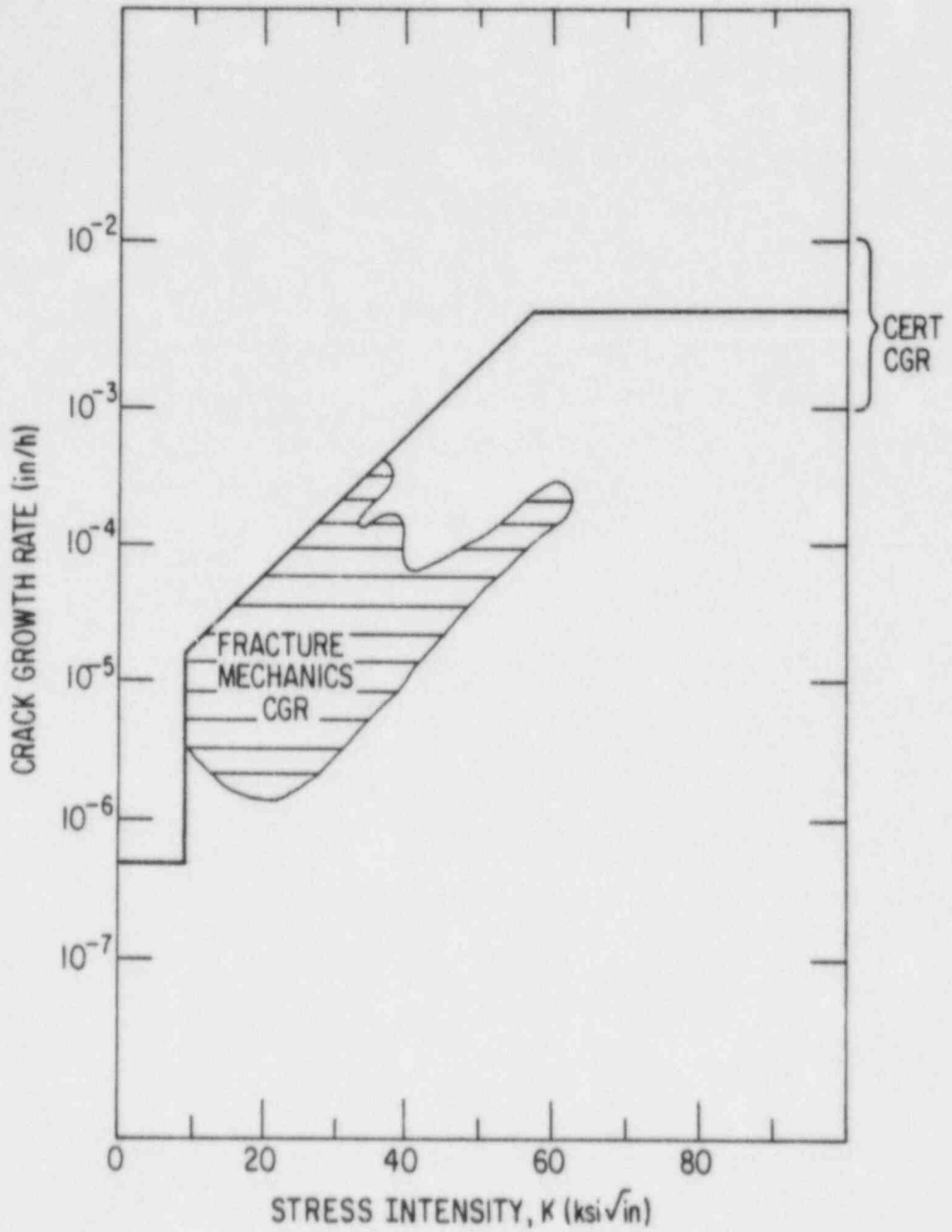

Fig. 54. Conservative Estimate of Upper-Bound Stress Corrosion Crack Growth Rates for Type 304 SS in BWR Environments.

flaws conservative estimates of the times range from two months for the 10-in. pipe to three months for the 24-in. pipe. Even for the case of the compound crack with a complete circumferential part-through crack in addition to the throughwall crack, the time is relatively long for most crack geometries. Figure 50 shows the bounding envelope of crack geometries for which there is at least ten days before the onset of unallowable leakage and failure. Leak-before-break in this sense is violated only in the case of very deep, very long part-through cracks. However, it should also be noted that leakage from cracks which are not large enough to cause collapse can be very large. For a 24-in. pipe, the leak rate through a 22-in.-long crack (∿30% of the circumference) under typical applied stresses is ∿100 gpm, which is close to the make-up capacity of most BWRs. Hence, while LBB is still valid in many cases for cracks greater than 30% of circumference, the resulting leakage could require use of the high-pressure emergency core cooling system.

E. Evaluation of Environmental Corrective Actions
(W. E. Ruther, W. K. Soppet, and T. F. Kassner)

1. Introduction

The objective of this subtask is to evaluate the potential effectiveness of proposed actions to solve or mitigate the problem of IGSCC in BWR piping and safe ends thorugh modifications of the water chemistry. Although the reactor coolant environment has a profound influence on the performance and reliability of nuclear power-plant components, the synergistic effects of oxygen (produced by radiolytic decomposition of the water) and impurities (e.g., H_2SO_4 from decomposition of ion exchange resins during periodic intrusions into the primary system) on the IGSCC susceptibility and cyclic crack growth properties of sensitized Type 304 SS have not been investigated adequately. Also, it is not clear whether the potential benefits associated with small additions of hydrogen to the coolant can be realized in the presence of impurities within the normal operating limits on pH (5.6 to 8.6 at 25°C) and specific conductance ($\leq$1 μS/cm at 25°C) of the reactor coolant water.

2. Summary of Results

During this reporting period, additional results have been obtained from constant-extension-rate-tensile (CERT) tests on a reference heat of Type 304 SS, with two levels of sensitization, in 289°C water with a range of dissolved oxygen and sulfate concentrations. The effect of 0.5 and 2.0 ppm dissolved hydrogen on the SCC susceptibility of lightly (EPR = 2 C/cm^2) and moderately (EPR = 20 C/cm^2) sensitized steel was also evaluated and the CERT parameters (viz., the time to failure and fracture morphology) were correlated with the sulfate concentration, feedwater conductivity, and electrochemical potential of Type 304 SS and platinum electrodes in the high-temperature environment.

The influence of pH at high temperature on the IGSCC susceptibility of the steel in the lightly sensitized condition was determined in very dilute H_2SO_4-Na_2SO_4 solutions containing 0.2 ppm dissolved oxygen at a strain rate of 1×10^{-6} s^{-1}. The influence of several other cations, in conjunction with

0.1 ppm sulfate, on IGSCC of the steel at 289°C was also investigated at this oxygen concentration and strain rate.

Several crack growth experiments were performed on fracture-mechanics type specimens of the steel in high-purity water and in water containing 0.1 ppm sulfate as H_2SO_4 at 289°C with cyclic loading at a low frequency, moderate stress intensity, and high load ratio (R).

From the standpoint of delineating the influence of high-temperature water on IGSCC susceptibility of Type 304 SS, the corrosion potential of the steel is primarily a function of the dissolved oxygen concentration, whereas the conductivity is directly related to the concentration of ionic species in the water. The region of corrosion potential and conductivity that yields immunity to IGSCC of sensitized (EPR = 2 and 20 C/cm^2) Type 304 SS was determined from CERT experiments at 289°C in water with a range of dissolved oxygen, hydrogen, and sulfate concentrations. The results show that the steel is (1) susceptible to IGSCC in very pure water ($\lesssim$0.1 μS/cm) at corrosion potentials $\gtrsim$50 mV(SHE), and (2) the conductivity of reactor coolant water would have to be maintained to $\lesssim$0.2 μS/cm to achieve immunity to IGSCC at a corrosion potential of -350 mV(SHE), i.e., a value that was measured during hydrogen addition to the feedwater of the Dresden-2 BWR to suppress the dissolved oxygen concentration of the recirculation loop water.

CERT experiments in which the dissolved oxygen and hydrogen concentrations were varied over the range ~0.005 to 0.2 and 0 to 2.0 ppm, respectively, indicate that dissolved hydrogen per se in the water has only a small beneficial effect on IGSCC susceptibility at low dissolved oxygen concentrations ($\lesssim$0.03 ppm) and virtually no effect at an oxygen concentration of ~0.2 ppm for sulfate concentrations between ~0.1 and 1 ppm.

With regard to the relative effects of pH and sulfate concentration on IGSCC susceptibility of the sensitized steel in 289°C water containing 0.2 ppm dissolved oxygen, the CERT experiments reveal that the sulfate concentration in the range 0.01 to 100 ppm is a major factor in IGSCC in contrast to pH at 25 or 289°C of the H_2SO_4-Na_2SO_4 at a given sulfate concentration. Also, other cations typical of corrosion product species, in conjunction with

0.1 ppm sulfate, do not produce significant differences in the IGSCC behavior of the steel in water containing 0.2 ppm dissolved oxygen as determined in CERT experiments at 289°C. Based on limited data and other factors that complicate direct comparisons, it is unlikely that differences in the extent of intergranular cracking in reactor coolant circuits can be attributed to certain cations that may be present in the water of one system and not in another.

3. Technical Progress

a. Influence of Dissolved Oxygen, Hydrogen, and Sulfate (as H_2SO_4) on IGSCC of Sensitized Type 304 SS at 289°C

There appears to be a strong synergistic effect of dissolved oxygen (produced by radiolytic decomposition of the water in the reactor) and impurities (e.g., sulfate and chlorides, which may be present from decomposition of ion exchange resins and condenser leakage, respectively) on IGSCC susceptibility of Type 304 SS. (Both sulfates and chlorides have been examined; for a given concentration, sulfate additions appear to be somewhat more detrimental; also, under current water chemistry specifications, chloride levels are closely monitored, but no explicit measurement of sulfate levels is normally made.) The influence of dissolved oxygen and sulfate (as H_2SO_4) concentrations on the time to failure in CERT tests of lightly and moderately sensitized Type 304 SS (Heat 30956) in 289°C water is shown in Fig. 55. A sulfate concentration of 0.1 ppm, which is within the normal operating limits for conductivity (<1.0 μS/cm at 25°C) and pH (5.6 to 8.6 at 25°C) of reactor coolant water, produces a large increase in IGSCC susceptibility (i.e., a significant decrease in the time to failure) of Type 304 SS for dissolved oxygen concentrations $\gtrsim$0.1 ppm.

The results shown in Fig. 55 suggest that the influence of impurities decreases rapidly as the oxygen level decreases below ~0.08 ppm. Additional results shown in Fig. 56 indicate that at low dissolved oyxgen concentrations, viz., ~0.03 and 0.005 ppm (upper curve of each panel), which are representative of an alternative BWR water chemistry produced by adding ~1.5 ppm hydrogen to the feedwater, sulfuric acid additions that produce a

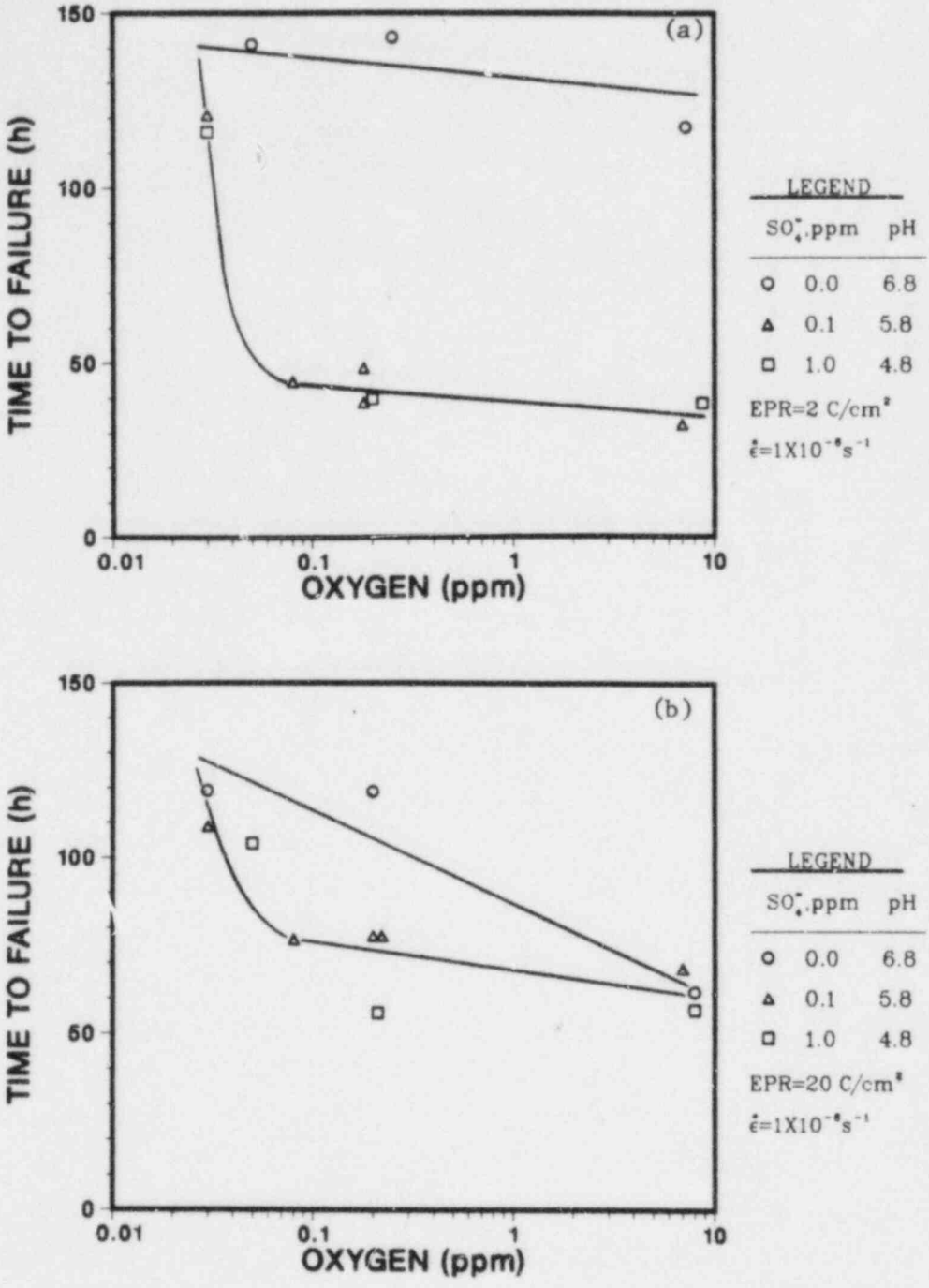

Fig. 55. Effect of Dissolved Oxygen and Sulfate (as H_2SO_4) Concentration in 289°C Water on the Time to Failure of (a) Lightly (EPR = 2 C/cm^2) and (b) Moderately (EPR = 20 C/cm^2) Sensitized Type 304 SS (Heat 30956) in CERT Experiments at a Strain Rate of 1 x 10^{-6} s^{-1}.

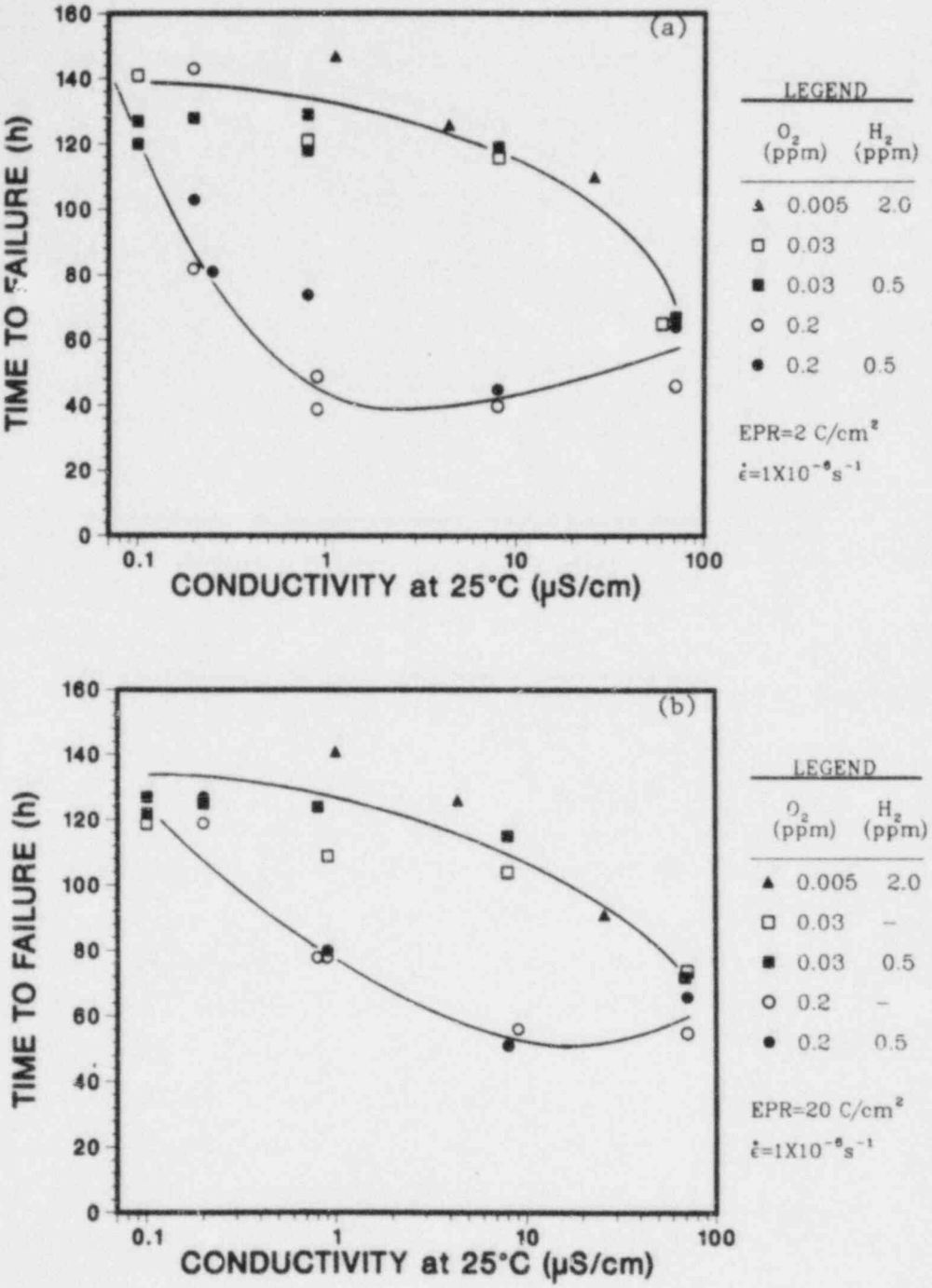

Fig. 56. Influence of Conductivity of the Feedwater on the Time to Failure of (a) Lightly (EPR = 2 C/cm^2) and (b) Moderately (EPR = 20 C/cm^2) Sensitized Type 304 SS (Heat 30956) in CERT Experiments at 289°C and a Strain Rate of 1 x 10^{-6} s^{-1} in Water Containing 0.2, 0.03, and 0.005 ppm Dissolved Oxygen Without (Open Symbols) and With (Closed Symbols) 0.5 or 2.0 ppm Hydrogen.

conductivity of <1 μS/cm have a small effect on IGSCC susceptibility (as measured by time to failure). However, for the normal dissolved oxygen concentrations of ~0.2 ppm (lower curve of each panel), addition of sulfuric acid produces a marked decrease in the time to failure even with a dissolved-hydrogen level of ~0.5 ppm.

In the reactor core and recirculation system, the dissolved oxygen and hydrogen are coupled through radiolysis of the water in the core, whereas in the laboratory the concentration of each species can be altered independently. The results shown in Fig. 56 indicate that hydrogen itself has a relatively minor effect on the SCC susceptibility in comparison to the dissolved oxygen concentration.

During the CERT experiments, the electrochemical potentials of Type 304 SS and a platinum electrode were monitored and recorded as a function of time. The measurements of electrochemical potential were made at 289°C relative to an external 0.1M KCl/AgCl/Ag reference electrode and the values were converted to the standard hydrogen electrode at 289°C. The results, shown in Figs. 55 and 56, can be restated in terms of the electrochemical potential and the conductivity. Although it is usually assumed that the corrosion potential of the stainless steel in a BWR is primarily a function of the dissolved oxygen concentration, other oxidizing species could be present in the reactor coolant, and the corrosion potential is perhaps a more general characterization of the environment than the dissolved-oxygen concentration. Conductivity is a direct measure of the concentration of ionic impurities in the water. The regime of corrosion potential and conductivity in which Type 304 SS is immune to IGSCC at 289°C, based upon the CERT results for a strain rate of 1×10^{-6} s^{-1}, is shown in Fig. 57. At both levels of sensitization, Type 304 SS is susceptible to IGSCC at 289°C at corrosion potentials $\gtrsim$50 mV(SHE), even in very pure water ($\lesssim$0.1 μS/cm). However, for corrosion potentials between 50 mV and -500 mV(SHE), water purity has a strong influence on IGSCC susceptibility, e.g., at a corrosion potential of -350 mV(SHE), the conductivity must be $\lesssim$0.2 μS/cm to achieve immunity to IGSCC. A corrosion potential of -350 mV(SHE) was obtained for Type 304 SS in the Dresden-2 reactor during a period when hydrogen was added to the feedwater to suppress the oxygen concentration of the water in the recirculation loop to $\lesssim$20 ppb.[42]

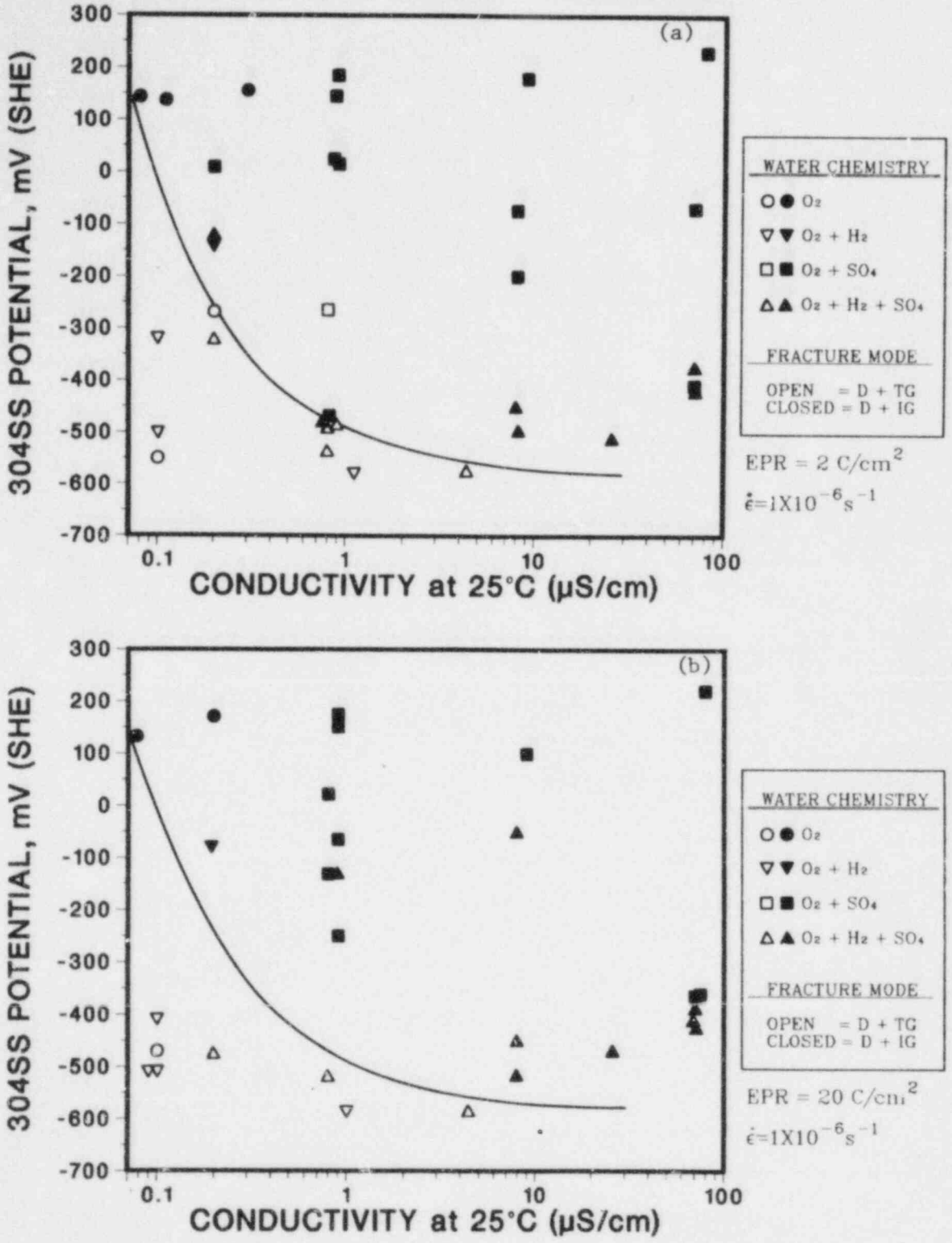

Fig. 57. Regime of Corrosion Potential and Feedwater Conductivity That Results in Immunity of Sensitized Type 304 SS to IGSCC (Region Below Curve in Each Panel in CERT Experiments at 289°C in Simulated BWR-Quality Water Containing Dissolved Oxygen, Hydrogen, and Sulfate as H_2SO_4. (a) Lightly sensitized (EPR = 2 C/cm^2) and (b) moderately (EPR = 20 C/cm^2) sensitized Type 304 SS. Open and closed symbols represent transgranular and intergranular fracture mode, respectively.

Other studies[43] suggest an even greater role of impurities at low oxygen levels. It is important to note that the results in Fig. 57 are based on one impurity (sulfate) and one strain rate (1×10^{-6} s^{-1}). Additional testing at lower strain rates will be performed to confirm our results on the effect of sulfates at low dissolved-oxygen concentrations (potentials). The influence of other impurities must also be investigated before we can realistically specify the impurity levels (which may depend on the nature of the impurity) at which additions of hydrogen will significantly reduce susceptibility to IGSCC.

b. Effect of pH at 289°C on IGSCC Susceptibility of Type 304 SS in Dilute H_2SO_4-Na_2SO_4 Solutions

In the previous CERT experiments to investigate the influence of impurities on IGSCC of sensitized Type 304 SS, sulfate was added to the feedwater in the form of H_2SO_4 since this is the major product[44] from the thermal degradation of cation exchange resins that are used in reactor-water-cleanup demineralizer systems. From the standpoint of understanding the influence of water chemistry on IGSCC, the relative contributions of the pH and the concentration of specific anions (e.g., sulfate) in the water on crack propagation has not been established. Technical specification limits, utility administrative goals, and the U.S. NRC Regulatory Guide 1.56 pertaining to the maintenance of water purity in BWRs are formulated in terms of the conductivity, pH, and concentration of specific ions (viz., Cl^-) to minimize corrosion of reactor components, including the Zircaloy fuel cladding. Water chemistry is also a significant factor in the deposition of activated corrosion products which contribute to radiation buildup in the heat transport system outside of the reactor vessel.

The envelope for pH and conductivity of recirculation loop water for normal operation and for off-normal water chemistry, not to exceed a period of 72 h for any single incident, is shown in Fig. 58 for H_2SO_4, Na_2SO_4, and NaOH impurity species. Typically, BWRs operate with at slightly acidic pH (~6.0-7.0 at 25°C) with conductivities in the range of 0.15 to 0.8 μS/cm. Water chemistry experience regarding the frequency and magnitude of reactor

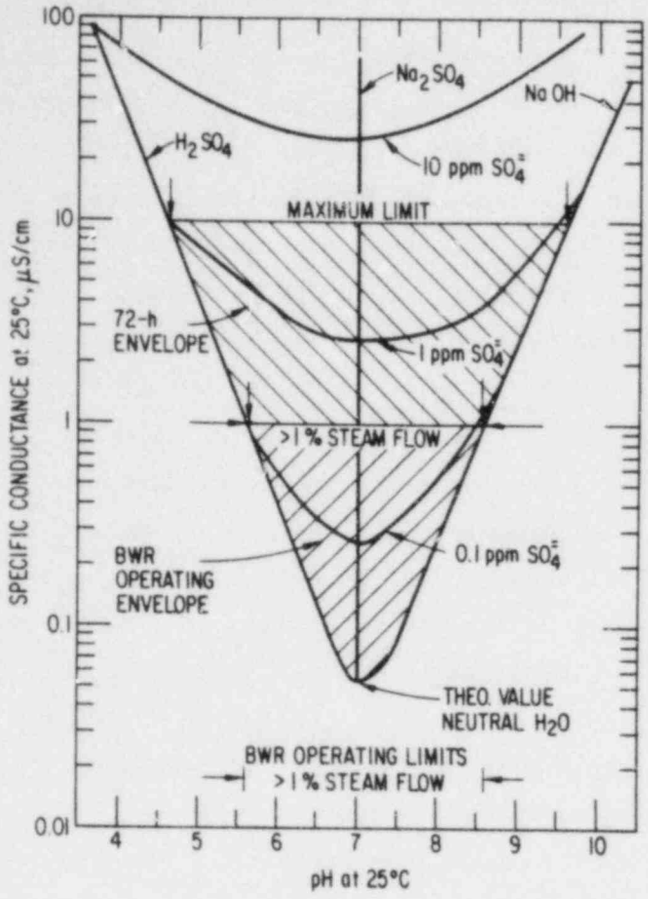

Fig. 58.
Regime of Conductivity and pH at 25°C of BWR Coolant Water for Normal and Off-Normal Operation with Sulfate Impurity.

water transients from resin intrusions, condenser tube leakage, and unavailability of the reactor water cleanup system in U.S. BWRs has been reviewed.[45] This survey confirms that resin intrusions into the reactor coolant are not an uncommon occurrence.

The effect of pH on IGSCC of sensitized (EPR = 2 C/cm^2) Type 304 SS (Heat 30956) has been evaluated in a series of CERT tests in which the sulfate was held fixed at several concentrations between 0.01 and 100 ppm while the pH was varied by changing the proportions of sulfuric acid and sodium sulfate in the solution. CERT tests were also performed in solutions in which the pH at 289°C was fixed at several values between 4.27 and 6.35 (5.63 is neutral pH at 289°C) by adjusting the molar ratios of H_2SO_4 and Na_2SO_4 for total sulfate concentrations up to 100 ppm. These conditions encompass the range of pH and conductivity values between the H_2SO_4 and Na_2SO_4 curves depicted in Fig. 58. The rationale for concentrations of H_2SO_4 and Na_2SO_4 for the specific experiments is based on the plot of pH at 289°C as a

function of the sulfate concentration in Fig. 59 for different molar ratios of the constituents. The feedwater chemistries for CERT experiments in which the total sulfate concentration was maintained at 0.01, 0.1, 1.0, 10.0, and 100 ppm are given in Table XI along with the measured pH and conductivity values at 25°C. Similar information for tests to determine the influence of sulfate concentration for pH values of ~4.3, 5.3, 5.5, 5.6, and 6.3 at 289°C are given in Table XII. The calculated pH values at 289°C are based on the concentrations of H_2SO_4 and Na_2SO_4 along with information on the dissociation of water[46] and the second dissociation constant of sulfuric acid[47] at high temperature. Our results of high-temperature pH measurements of dilute H_2SO_4, NaOH, and H_2SO_4/Na_2SO_4 solutions at 289°C by means of a solid-electrolyte sensor[48] indicate that the agreement between the measured and calculated values was quite good.[49] Figure 60 illustrates the theoretical response of the sensor along with measured potential values for different H_2SO_4 and NaOH concentrations in the feedwater for two experiments.

The IGSCC results in Table XI show that the CERT parameters are not strongly dependent on the pH of the solution, particularly for sulfate concentrations $\gtrsim$1.0 ppm. At lower total sulfate concentrations (viz., 0.01 and 0.1 ppm), the less acidic solutions tend to be more detrimental in terms of the time to failure, maximum stress, etc., as well as the amount of intergranular fracture and the morphology of the fracture surface. For example, at total sulfate concentrations of 1, 10, and 100 ppm, the fracture surfaces of specimens in Na_2SO_4 solutions were completely intergranular, whereas in H_2SO_4 solutions a granulated fracture morphology with river patterns on some of the grain faces (G_3 in Table XI) was observed. At total sulfate concentrations of 0.01 and 0.1 ppm, the intergranular nature of the fracture surface was less severe, as evidenced by more river patterns (G_2), for CERT specimens in water containing H_2SO_4.

The results in Table XII corroborate the premise that the sulfate concentration at a fixed pH at 289°C is the major factor in IGSCC susceptibility, particularly for near neutral pH values of ~5.3, 5.5, and 5.6 at 289°C and for total sulfate concentrations below ~10 ppm.

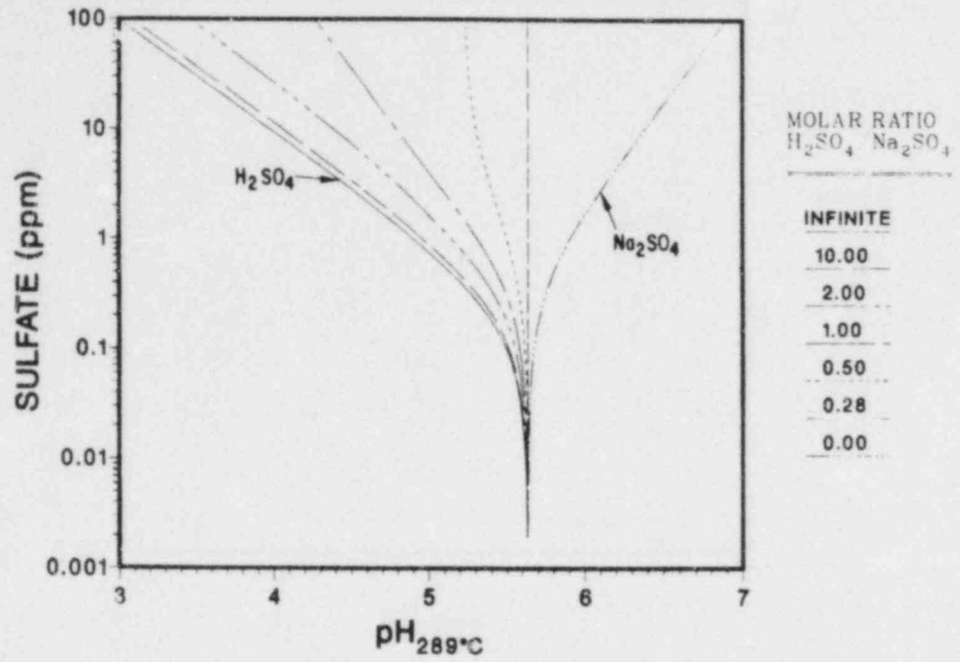

Fig. 59. Relationship between Sulfate Concentration and pH at 289°C for Different Molar Ratios of H_2SO_4/Na_2SO_4 Based on the Dissociation of Water and the Second Dissociation Constant for H_2SO_4 in Aqueous Solutions at High Temperatures.

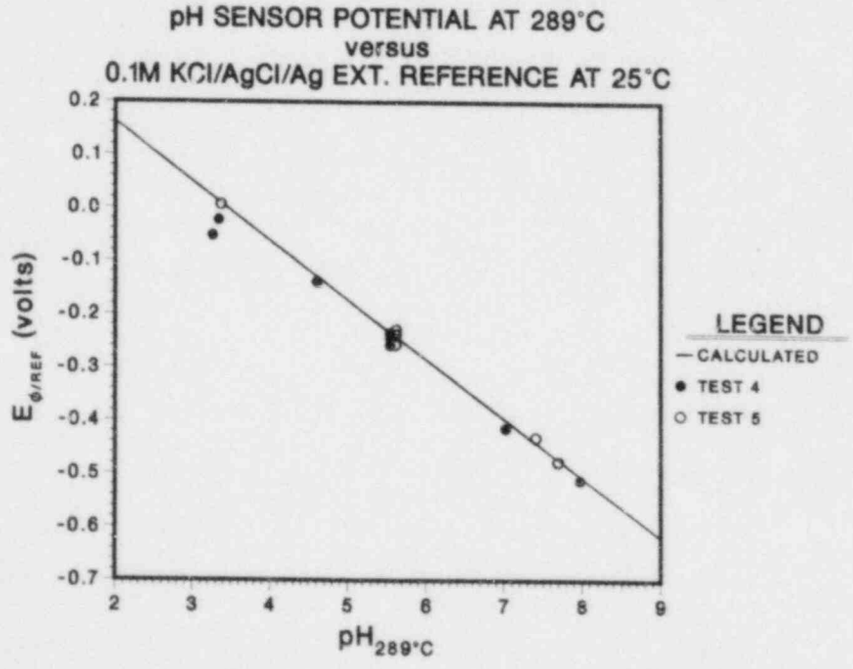

Fig. 60. Potential of Yttria-stabilized Zirconia Solid Electrolyte Sensor (with a Cu/Cu_2O Internal Reference) at 289°C, with Respect to a 0.1M KCl/AgCl/Ag External Reference Electrode, as a Function of pH 289°C of Deaerated Water. The line denotes the theoretical response of the sensor and the symbols represent measured values for different H_2SO_4 and NaOH concentrations for two experiments.[49]

Table XI. Results of CERT Tests on Sensitized Type 304 SS Specimens[a] (Heat 30956) to Establish the Influence of pH at Constant Sulfate Concentrations in 289°C Water

	Feedwater Chemistry							CERT Parameters				
Test No.	Oxygen, ppm	(Total) $SO_4^=$, ppm	(H_2SO_4) $SO_4^=$, ppm	(Na_2SO_4) $SO_4^=$, ppm	Molar[b] Ratio	Cond. at 25°C, μS/cm	pH at 25°C	pH[c] at 289°C	Failure Time, h	Maximum Stress, MPa	Total Elong., %	Reduction in Area, %	Fracture[d] Morphology
A28	0[e]	100.0	100.0	0	∞	785.0	2.76	3.00	41	301	15	18	0.12D, 0.88G_3
A27	0[e]	100.0	100.0	0	∞	800.0	2.74	3.00	45	287	16	24	0.14D, 0.86G_3
A34	0[e]	100.0	50.0	50.0	1.0	530.0	3.05	4.26	57	359	20	24	0.19D, 0.81G_3
A23	0.35[e]	100.0	33.0	67.0	0.50	450.0	3.22	5.23	54	343	19	20	0.24D, 0.76G_3
A15	0.01[e]	100.0	33.0	67.0	0.50	485.0	3.23	5.23	79	413	28	33	0.27D, 0.12T, 0.61G_3
A22	0.40[e]	100.0	22.0	78.0	0.28	390.0	3.40	5.63	48	328	17	18	0.16D, 0.84G_3
A14	0.01[e]	100.0	22.0	78.0	0.28	390.0	3.44	5.63	51	324	18	27	0.17D, 0.09T, 0.74I
A24	0.42[e]	100.0	6.5	93.5	0.07	290.0	3.94	6.30	43	300	15	24	0.10D, 0.90G_3
A26	0.45[e]	100.0	0	100.0	0	270.0	6.91	6.89	41	308	15	15	0.15D, 0.85G_3
A13	0.05[e]	100.0	0	100.0	0	270.0	6.81	6.89	37	303	13	13	0.11D, 0.89I
A36	0[e]	50.0	50.0	0	∞	425.0	3.01	3.30	56	342	20	26	0.16D, 0.84G_3
A37	0.18	10.0	10.0	0	∞	77.0	3.78	4.04	49	300	17	23	0.18D, 0.82I
A6	0.21	8.5	8.5	0	∞	74.0	3.80	4.03	77	377	28	24	0.10D, 0.90G_3
A17	0.25	10.0	3.3	6.7	0.50	48.0	4.24	5.30	45	312	16	19	0.26D, 0.74G_3
A21	0.20	10.0	2.2	7.8	0.28	41.0	4.42	5.63	37	290	13	15	0.15D, 0.85G_3
A9	0.19	9.8	0.1	9.7	0.01	25.6	5.87	5.76	45	286	16	29	0.15D, 0.85I
A10	0.23	10.0	0	10.0	0	26.3	7.10	6.35	40	296	14	20	0.17D, 0.83I
A5	0.18	0.82	0.82	0	∞	8.4	4.80	4.96	51	326	19	18	0.30D, 0.70G_3
A31	0.21	1.0	0.50	0.50	1.0	5.5	5.06	5.31	51	330	18	26	0.21D, 0.22T, 0.57G_3
A16B	0.20	1.0	0.33	0.67	0.50	3.6	6.14	5.50	43	303	16	24	0.24D, 0.76G_3
A20B	0.24	1.0	0.22	0.78	0.28	4.1	5.52	5.63	54	341	20	25	0.12D, 0.88G_3
A8	0.20	0.97	0.05	0.92	0.05	2.9	6.00	5.56	46	309	17	16	0.11D, 0.89I
A11	0.22	1.10	0	1.10	0	3.0	6.40	5.89	45	299	16	22	0.16D, 0.84I
A3	0.20	0.09	0.09	0	∞	0.91	5.74	5.51	79	402	29	37	0.22D, 0.78G_2
A7	0.20	0.05	0.04	0.01	4.0	0.45	6.05	5.58	61	366	22	24	0.28D, 0.72G_3
A30	0.20	0.15	0.10	0.05	2.0	0.93	5.82	5.53	59	365	21	27	0.22D, 0.78G_3
A12	0.20	0.15	0	0.15	0	0.66	6.90	5.69	54	345	20	29	0.22D, 0.78G_3
A29	0.19	0.01	0.01	0	∞	0.14	6.36	5.62	109	485	39	43	0.67D, 0.33G_2
A18	0.20	0.01	0.0022	0.0078	0.28	0.33	6.97	5.63	93	453	33	34	0.26D, 0.47T, 0.27G_3

[a]Specimens were sensitized to an EPR value of 2 C/cm^2 by heat treatment at 700°C for 0.25 h plus 500°C for 24 h; the specimens were exposed to the environment for ~20 h at 289°C before straining at a rate of 1 x 10^{-6} s^{-1}.

[b]Molar ratio of H_2SO_4/Na_2SO_4.

[c]Calculated pH at 289°C based on the concentrations of H_2SO_4 and Na_2SO_4 along with information on the dissociation of water and the second dissociation constant of sulfuric acid at high temperatures.

[d]Ductile (D), transgranular (T), granulated (G), intergranular (I), in terms of the fraction of the reduced cross-sectional area. Characterization of the fracture surface morphologies is in accordance with the illustrations and definitions provided in Alternate Alloys for BWR Pipe Applications: Sixth Semiannual Progress Report, April-September 1980, General Electric Company Report NEDC-23750-8, pp. 5-70 to 5-81.

[e]Effluent oxygen concentrations by Chemetric colorimetric analyses.

Table XII. Results of CERT Tests on Sensitized Type 304 SS Specimens[a] (Heat 30956) to Establish the Influence of Sulfate Concentration for Constant pH at 289°C

	Feedwater Chemistry								CERT Parameters				
Test No.	Oxygen, ppm	(Total) $SO_4^{=}$, ppm	(H_2SO_4) $SO_4^{=}$, ppm	(Na_2SO_4) $SO_4^{=}$, ppm	Molar[b] Ratio	Cond. at 25°C, µS/cm	pH at 25°C	pH[c] at 289°C	Failure Time, h	Maximum Stress, MPa	Total Elong., %	Reduction in Area, %	Fracture[d] Morphology
A10	0.23	10.0	0	10.0	0	26.3	7.10	6.35	40	296	14	20	0.17D, 0.83I
A25	0.35	20.0	1.0	19.0	0.05	61.0	4.76	6.30	21	362	8	17	0.17D, 0.85G_3
A25B	0.20	20.0	1.0	19.0	0.05	57.0	4.75	6.30	51	340	18	23	0.22D, 0.78G_3
A24	0.42	100.0	6.5	93.5	0.07	290.0	3.94	6.31	43	300	1[illegible]	24	0.10D, 0.90G_3
A2	0.24	0	0	0	-	0.14	6.12	5.62	166	493	60	66	0.80D, 0.20T
A18	0.20	0.01	0.0022	0.0078	0.28	0.33	6.97	5.63	93	453	33	34	0.26D, 0.47T, 0.27G_3
A19	0.20	0.1	0.022	0.078	0.28	0.50	6.45	5.63	52	323	19	30	0.15D, 0.85G_3
A20B	0.24	1.0	0.22	0.78	0.28	4.10	5.55	5.63	54	341	20	25	0.12D, 0.88G_3
A21	0.20	10.0	2.20	7.80	0.28	41.0	4.42	5.63	37	290	13	15	0.15D, 0.85G_3
A22	0.40	100.0	22.0	78.0	0.28	390.0	3.40	5.63	48	328	17	18	0.16D, 0.84G_3
A3	0.20	0.09	0.09	0	∞	0.91	5.74	5.51	79	402	29	37	0.22D, 0.78G_2
A30	0.20	0.15	0.10	0.05	2.0	0.93	5.82	5.53	59	365	21	27	0.22D, 0.78G_3
A16B	0.20	1.0	0.33	0.67	0.5	3.58	6.14	5.50	43	303	16	24	0.24D, 0.76G_3
A4	0.18	0.23	0.23	0	∞	2.0	5.45	5.38	58	363	21	25	0.26D, 0.74G_3
A31	0.21	1.0	0.50	0.5	1.0	5.5	5.06	5.31	51	330	18	26	0.21D, 0.22T, 0.57G_3
A17	0.25	10.0	3.3	6.7	0.5	48.0	4.24	5.30	45	312	16	19	0.26D, 0.74G_3
A35	0.20	5.0	5.0	0	∞	43.0	4.03	4.26	36	287	13	8	0.16D, 0.84G_3
A32	0.05[e]	5.8	5.3	0.5	10.0	45.0	3.99	4.27	59	334	21	28	0.17D, 0.83G_3
A33	0.21	12.9	8.6	4.3	2.0	77.0	3.78	4.27	43	309	15	22	0.30D, 0.70G_3
A34	0[e]	100.0	50.0	50.0	1.0	530.0	3.05	4.26	57	359	20	24	0.19D, 0.81G_3

[a]Specimens were sensitized to an EPR value of 2 C/cm^2 by heat treatment at 700°C for 0.25 h plus 500°C for 24h; the specimens were exposed to the environment for ~20 h at 289°C before straining at a rate of 1 x 10^{-6} s^{-1}.

[b]Molar ratio of H_2SO_4/Na_2SO_4.

[c]Calculated pH at 289°C based on the concentrations of H_2SO_4 and Na_2SO_4 along with information on the dissociation of water and the second dissociation constant of sulfuric acid at high temperatures.

[d]Ductile (D), transgranular (T), granulated (G), intergranular (I), in terms of the fraction of the reduced cross-sectional area. Characterization of the fracture surface morphologies is in accordance with the illustrations and definitions provided in Alternate Alloys for BWR Pipe Applications: Sixth Semiannual Progress Report, April-September 1980, General Electric Company Report NEDC-23750-8, pp. 5-70 to 5-81.

[e]Effluent oxygen concentrations by Chemetric colorimetric analyses.

The dependence of the time to failure on pH at 25 and 289°C is shown in Fig. 61 for several sulfate concentrations between 0.01 and 100 ppm. Because of accelerated corrosion of the high-temperature regions of the stainless steel system, it was not possible to maintain the effluent dissolved oxygen concentration of the water at ~0.2 ppm with high sulfuric acid concentrations ($\gtrsim$20 ppm) in the feedwater, even when the inlet oxygen concentration was increased to ~1-2 ppm. Electrochemical potential values below -300 mV(SHE) as well as measurements of the effluent dissolved oxygen concentration by a conductometric thallium column technique and Chemetric colorimetric analyses confirmed that the dissolved oxygen in the water was, in fact, very low ($\lesssim$0.01 ppm). Since IGSCC susceptibility is dependent on dissolved oxygen as well as the impurity concentration (Fig. 55), the results in Fig. 61 are based on data in Table XI in which the effluent dissolved oxygen values were between ~0.2 and 0.4 ppm.

The relationship between the time to failure of the CERT specimens at 289°C and the conductivity of the feedwater is shown in Fig. 62 for experiments with different total sulfate concentrations and molar ratios of H_2SO_4 and Na_2SO_4. This figure depicts the strong influence of impurity concentration on IGSCC for conductivity values between ~0.1 and 1 μS/cm. No further decrease in the time to failure occurs at higher conductivity values. At values $\gtrsim$1 μS/cm (sulfate concentrations $\gtrsim$0.1 ppm), the results in Fig. 61 and Table XI also reveal no significant variations in the time to failure at fixed sulfate concentrations with different molar ratios of H_2SO_4 and Na_2SO_4.

In summary, this series of CERT experiments indicates that the bulk pH per se has a minimal effect on IGSCC susceptibility of sensitized Type 304 SS at 289°C relative to the sulfate concentration in water containing ~0.2 ppm dissolved oxygen. Thus, of the several processes that alone or in combination are thought to facilitate breakdown of the passive film or impede repassivation of the crack tip (viz., differential aeration, migration of sulfate, and local acidification), it appears that the pH of the bulk water in itself is not an important factor in the intergranular cracking process. Also, an increase in the anion (i.e., sulfate) concentration of the bulk water above ~0.1 ppm, which could increase the chemical driving force for sulfate

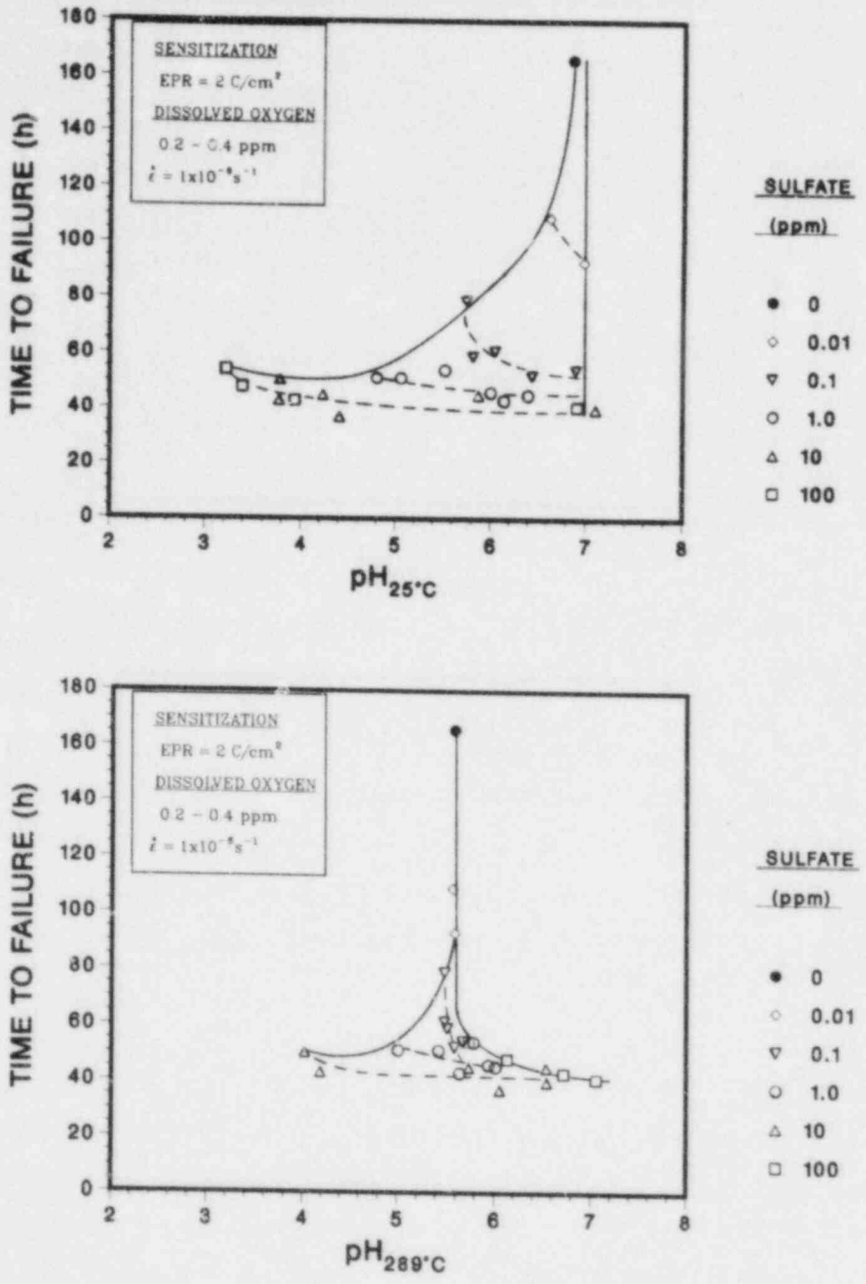

Fig. 61. Effect of pH at 25 and 289°C of H_2SO_4-Na_2SO_4 Solutions, at Several Total Sulfate Concentrations, on the Time to Failure of Lightly Sensitized (EPR = 2 C/cm^2) Type 304 SS Specimens in CERT Experiments at a Strain Rate of 1 x 10^{-6} s^{-1} in 289°C Water with 0.2-0.4 ppm Dissolved Oxygen.

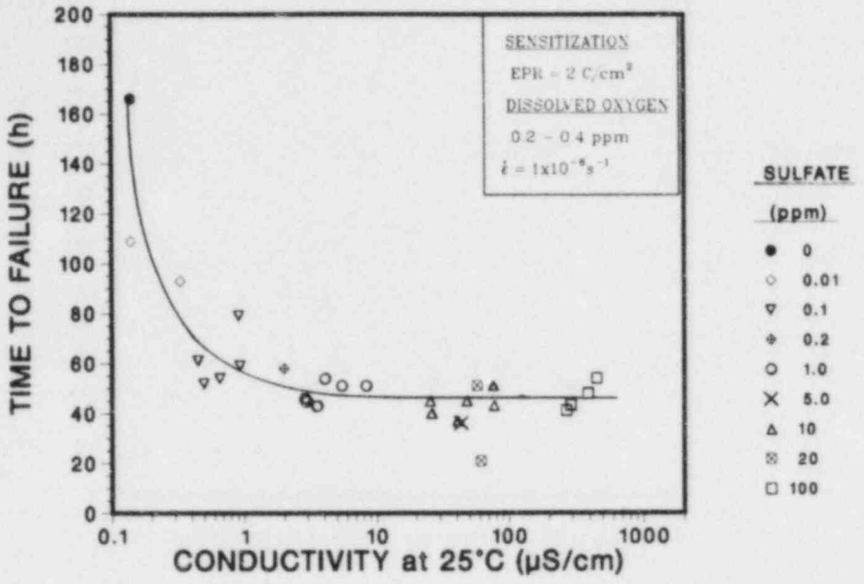

Fig. 62. Effect of Conductivity of the Feedwater with Different Sulfate Concentrations and Molar Ratios of H_2SO_4-Na_2SO_4 on the Time to Failure of Lightly Sensitized (EPR = 2 C/cm^2) Type 304 SS (Heat 30956) in CERT Experiments at 289°C and a Strain Rate of 1 x 10^{-6} s^{-1} in Water Containing 0.2-0.4 ppm Dissolved Oxygen.

migration to the crack tip, does not accelerate the intergranular cracking process at a dissolved oxygen concentration of ~0.2 ppm. This is not the case at lower dissolved oxygen concentrations ($\lesssim$0.03 ppm) where the susceptibility increases as the conductivity of the water increases over the range ~1.0 to 80 μS/cm[49] (sulfate concentrations between ~0.1 and 10 ppm), as shown in Fig. 56.

Parenthetically, if a quantitative comparison is made of the CERT data in very dilute H_2SO_4 solutions,[49-51] including the information in Figs. 55-57, with the data in Tables XI and XII, and Figs. 58 and 59, the following anomaly must be considered. Although the heat of material (30956), level of sensitization, specimen geometry, and experimental procedures were identical in both sets of experiments, the former tests were performed in an Instron testing machine in contrast to a more compliant system with a worm gear Jactuator, gear reducer, and variable speed motor loading mechanism that was used in the A-series of experiments (Tables XI and XII). The strain rate of the specimens in the two systems was also identical (viz., 1 x 10^{-6} s^{-1})

based on measured extension rates of the specimens during the CERT tests. However, the failure times and total strain values for specimens tested in the more compliant loading system were ~20% larger for the same degree of sensitization of the material, water chemistry, flow rate, and temperature. This difference is reflected in the time to failure data for the lightly sensitized material (EPR = 2 C/cm^2) in water containing 0.2 ppm dissolved oxygen with different H_2SO_4 additions in Fig. 56 and the results in Fig. 62.

c. Influence of Dissolved Cations with 0.1 ppm Sulfate on IGSCC of Lightly Sensitized (EPR = 2 C/cm^2) Type 304 SS at 289°C in Water with 0.2 ppm Dissolved Oxygen

In addition to dissolved oxygen (produced by radiolytic decomposition of the water) and corrosion products, other impurity species can enter the reactor coolant water through a number of sources (e.g., condensate and reactor-water-cleanup demineralizers, condensate storage tank, the suppression pool and reactor heat removal system, etc.). Hydrogen and sodium are common cations in conjunction with sulfate and chloride from the decomposition or exhaustion of ion exchange resins and condenser leakage. Corrosion product species from the condenser, feedwater train, and other components can also enter the reactor coolant water. The influence of several dissolved cations in conjunction with 0.1 ppm sulfate on the IGSCC susceptibility of the lightly sensitized steel was evaluated at 289°C in water containing ~0.2 ppm dissolved oxygen. The results in Table XIII and Fig. 63 reveal that the various metal cations, typical of corrosion product species, and NH_4^+ at concentrations in excess of those measured in reactor coolant circuits do not produce significant differences in the IGSCC behavior of the steel as determined in the CERT experiments. Based on this limited information and other factors that complicate direct comparisons, it is unlikely that differences in the extent of intergranular cracking in reactor coolant circuits can be attributed to certain cations that may be present in the water of one system and not in another.

Table XIII. Influence of 0.1 ppm Sulfate with Different Cations on the SCC Susceptibility of Sensitized (EPR = 2 C/cm^2) Type 304 SS Specimens[a] (Heat 30956) in 289°C Water Containing 0.2 ppm Dissolved Oxygen

	Feedwater Chemistry				CERT Parameters				
Test No.	Oxygen, ppm	Impurity Species	Cond. at 25°C, µS/cm	pH at 25°C	Failure Time, h	Maximum Stress, MPa	Total Elong., %	Reduction in Area, %	Fracture Morphology[b]
A3	0.20	H_2SO_4	0.91	5.74	79	402	29	37	$0.22D, 0.78G_2$
A12	0.20	Na_2SO_4	0.66	6.90	54	345	20	29	$0.22D, 0.78G_3$
A40	0.24	$(NH_4)_2SO_4$	0.43	6.27	54	307	19	27	$0.10D, 0.90G_3$
A55	0.21	$Fe_2(SO_4)_3$	0.69	5.82	55	328	20	22	$0.19D, 0.81G_3$
A41	0.25	$FeSO_4$	0.55	6.11	58	324	21	33	$0.19D, 0.81G_3$
A42	0.26	$CuSO_4$	0.44	6.22	56	330	20	17	$0.28D, 0.72G_3$
A43	0.25	$NiSO_4$	0.37	6.26	49	315	17	20	$0.13D, 0.87G_3$
A44	0.25	$Cr_2(SO_4)_3$	0.59	5.95	47	307	17	27	$0.09D, 0.91G_3$
A45	0.28	$Al_2(SO_4)_3$	0.73	5.73	40	281	15	15	$0.21D, 0.79G_3$
A46	0.26	$ZnSO_4$	0.39	6.13	55	347	20	27	$0.33D, 0.67G_3$

[a]Specimens were exposed to the environment for ~20 h at 289°C before straining at a rate of 1×10^{-6} s^{-1}.
[b]Ductile (D) and granulated (G) in terms of the fraction of the reduced cross-sectional area. Characterization of the fracture surface morphologies is in accordance with the illustrations and definitions provided in Alternate Alloys for BWR Pipe Applications: Sixth Semiannual Progress Report, April-September 1980, General Electric Company Report NEDC-23750-8, pp. 5-70 to 5-81.

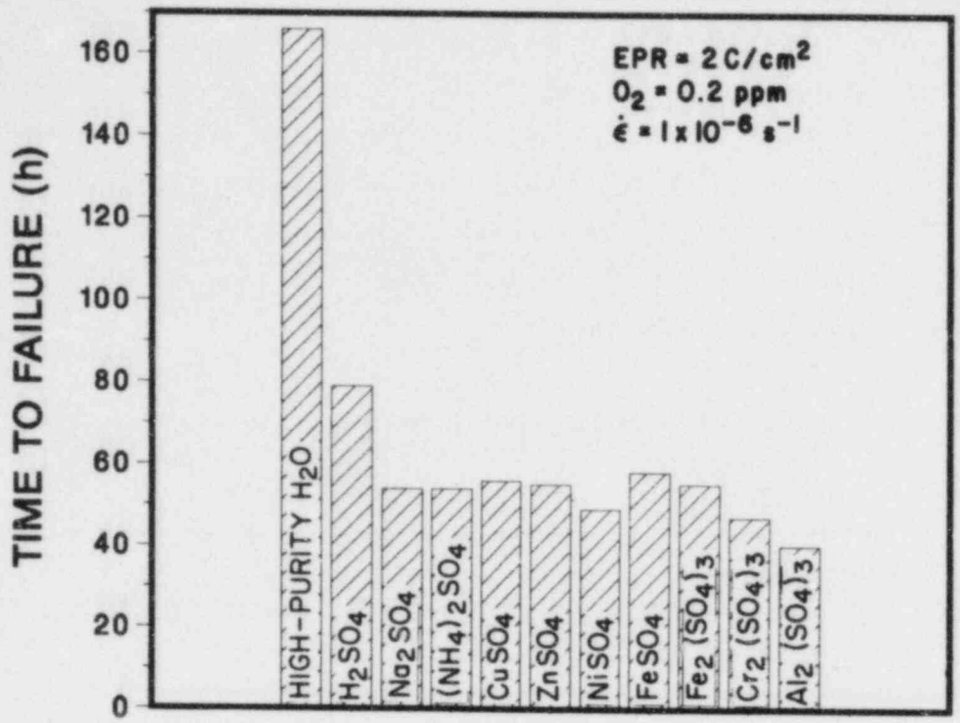

Fig. 63. Effect of 0.1 ppm Sulfate with Different Cations on the Time to Failure of Lightly Sensitized (EPR = 2 C/cm^2) Type 304 SS Specimens in CERT Experiments at a Strain Rate of 1 x 10^{-6} s^{-1} in 289°C Water with 0.2 ppm Dissolved Oxygen.

d. Crack Growth Rate Results on Type 304 SS

Fracture mechanics type crack growth tests are in progress on the same heat of material as in the CERT experiments. Three 1TCT specimens of Type 304 SS in the solution annealed and sensitized conditions (EPR = 0, 2, and 20 C/cm^2) were connected in series and stressed at an R value of 0.95 and an initial K_{max} of 28 MPa·m$^{1/2}$ under a positive sawtooth waveform. In the initial experiment, stress corrosion cracks in the sensitized specimens initiated in the test environment (8 ppm dissolved oxygen) after a relatively short time (~100 h). Since considerably longer time periods were encountered at a lower dissolved oxygen concentration, subsequent specimens were fatigue precracked in air at 289°C to provide 3-mm-deep starter cracks before testing in water at this temperature. Crack growth was determined from compliance measurements made periodically on each specimen with MTS clip gauges. The measured total crack lengths at the end of test were in good agreement with the values obtained from the clip gauges.

Crack growth rates in moderately sensitized material (EPR = 20 C/cm^2) in 289°C water with 8 ppm dissolved oxygen at low flow rate are given in Table XIV. The dependence of the crack growth rate on the stress intensity factor is shown in Fig. 64. The crack growth rate data are based on measurements of crack length versus time for intervals of ~300 to 2000 h, depending on the magnitude of the stress intensity. These results provide baseline information for comparison with subsequent experiments under different water chemistry conditions.

Table XIV. Crack Growth Rate Results on Sensitized (EPR = 20 C/cm^2) Type 304 SS in High-purity Water with 8 ppm Dissolved Oxygen at 289°C and an R Value of 0.95

Specimen[a] No.	Loading Time, s	Frequency,[b] Hz	K_{max}, $MPa \cdot m^{1/2}$	Crack Growth Rate	
				$m \cdot s^{-1}$	$mm \cdot h^{-1}$
2	12	8×10^{-2}	28	7.5×10^{-10}	2.7×10^{-3}
10			34	1.0×10^{-9}	3.7×10^{-3}
11			35	1.2×10^{-9}	4.3×10^{-3}
2	126	8×10^{-3}	34	1.2×10^{-10}	4.7×10^{-4}
			38	1.5×10^{-10}	5.6×10^{-4}
			50	4.7×10^{-10}	1.7×10^{-3}
			61	1.1×10^{-9}	3.9×10^{-3}
			64	1.7×10^{-9}	6.0×10^{-3}
2	1260	8×10^{-4}	28	1.2×10^{-10}	4.3×10^{-4}
			67	1.9×10^{-9}	6.8×10^{-3}
			70	3.2×10^{-9}	1.1×10^{-2}
			72	3.3×10^{-9}	1.2×10^{-2}

[a] Compact tension specimens (1TCT) from Heat 30956 were solution annealed at 1050°C for 0.5 h and sensitized at 700°C for 12 h.
[b] Frequency of the positive sawtooth waveform is based primarily on the loading time, since the load decrease occurs within ~1 s.

To further investigate the effect of impurities, viz., H_2SO_4 from decomposition of ion exchange resins, on the crack growth properties of the steel at 289°C, similar experiments are in progress in an identical MTS/autoclave system. Typical results for the crack length versus time for specimens with EPR values of 0, 2, and 20 C/cm^2 in 289°C water with 0.2 ppm dissolved oxygen and 0.1 ppm sulfate as H_2SO_4 are shown in Fig. 65. Loading

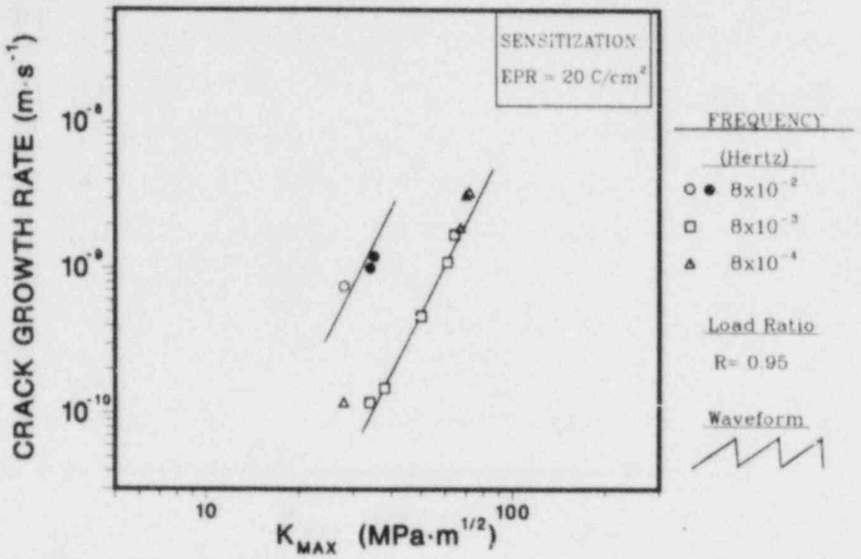

Fig. 64. Dependence of Crack Growth Rate on Stress Intensity Factor, K_{max}, for Moderately Sensitized (EPR = 20 C/cm^2) Type 304 SS in High-Purity Water with 8 ppm Dissolved Oxygen at 289°C. Steady-state crack growth rates were obtained at an R value of 0.95 with a positive sawtooth waveform, in which the frequency was determined by the slow loading time.

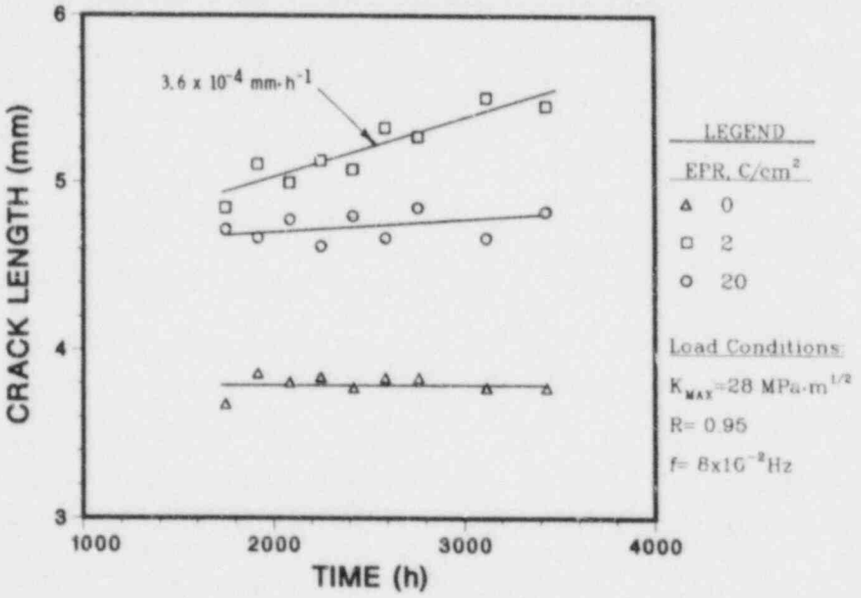

Fig. 65. Crack Length versus Time for 1TCT Specimens of Solution Annealed (EPR = 0) and Sensitized (EPR = 2 and 20 C/cm^2) Type 304 SS in 289°C Water Containing 0.2 ppm Dissolved Oxygen and 0.1 ppm Sulfate as H_2SO_4. The loading conditions for the positive sawtooth waveform with a slow loading time (12 s) and rapid unloading (1 s) are as follows; stress ratio R = 0.95, K_{max} = 28·m$^{1/2}$, and frequency = 8 x 10^{-2} Hz.

conditions for the initial phase of the experiment depicted in this figure were K_{max}, R, and frequency equal to ~28 MPa·$m^{1/2}$, 0.95, and 8 x 10^{-2} Hz, respectively, for the positive sawtooth waveform. Crack growth data obtained in a similar manner at higher K_{max} values are given in Table XV and Fig. 66. The most consistent crack growth occurred in the lightly sensitized specimen (EPR = 2 C/cm^2). Crack growth initiated in the solution annealed specimen at a K_{max} value of ~34 MPa·$m^{1/2}$ and the growth rate is somewhat larger than for the lightly sensitized specimen at a given K_{max} value. The crack growth rate for the moderately sensitized specimen (EPR = 20 C/cm^2) decreased as the apparent K_{max} increased early in the test (Table XV), which suggests that multiple cracks had formed in the specimen. This will be determined from metallographic evaluation of the specimen.

During a latter stage of the experiment, sulfate was not added to the feedwater to explore the effect of improved water chemistry (high-purity water with 0.2 ppm dissolved oxygen) on the crack growth rate of the material with three heat treatment conditions. The results in Table XV indicate that the crack growth rates in the solution annealed and lightly sensitized specimens decreased slightly, and that crack growth ceased in the moderately sensitized specimen. Upon the addition of sulfate to the feedwater in the last phase of the experiment, the crack growth rates in the impurity environment increased commensurate with the stress intensity values for each specimen.

Additional crack growth experiments will be performed under transient water chemistry conditions to determine the effect of impurity and dissolved oxygen concentrations on crack growth rates in sensitized Type 304 SS. Transients involving the dissolved oxygen concentration will simulate full oxygen suppression of the recirculation loop water (e.g., 10-20 ppb) achieved by hydrogen additions to the feedwater of a BWR.

Table XV. Crack Growth Rate Results on Type 304 SS in 289°C Water with 0.2 ppm Dissolved Oxygen and 0.1 ppm Sulfate as H_2SO_4 at an R Value of 0.95

Specimen[a] No.	EPR, C/cm^2	Frequency,[b] Hz	K_{max}, $MPa \cdot m^{1/2}$	Crack Growth Rate	
				$m \cdot s^{-1}$	$mm \cdot h^{-1}$
7	0	8×10^{-2}	28.0	0	0
			31.2	0	0
			34.3	2.7×10^{-10}	9.9×10^{-4}
			40.5	5.8×10^{-10}	2.1×10^{-3}
			45.2[c]	5.5×10^{-10}	2.0×10^{-3}
			49.3	7.0×10^{-10}	2.5×10^{-3}
9	2	8×10^{-2}	30.0	1.0×10^{-10}	3.6×10^{-4}
			35.6	2.2×10^{-10}	7.8×10^{-4}
			41.5	3.9×10^{-10}	1.4×10^{-3}
			50.2	5.8×10^{-10}	2.1×10^{-3}
			55.5[c]	5.0×10^{-10}	1.8×10^{-3}
			61.1	1.4×10^{-9}	5.2×10^{-3}
8	20	8×10^{-2}	29.4	$\sim 1.4 \times 10^{-11}$	$\sim 5.0 \times 10^{-5}$
			33.3	1.0×10^{-10}	3.6×10^{-4}
			36.6	3.1×10^{-11}	1.1×10^{-4}
			41.2	9.5×10^{-11}	3.4×10^{-4}
			41.6[c]	~ 0	~ 0
			42.1	1.6×10^{-10}	5.6×10^{-4}

[a] Compact tension specimens (1TCT) from Heat 30956 were solution annealed at 1050°C for 0.5 h (EPR = 0), sensitized at 700°C for 12 h (EPR = 20 C/cm^2), and 700°C for 0.25 h plus 500°C for 24 h (EPR = 2 C/cm^2).

[b] Frequency of the positive sawtooth waveform is based primarily on the loading time of 12 s, since the load decrease occurs within ~1 s.

[c] Sulfate was not added to the feedwater during this phase of the experiment, i.e., high-purity water with 0.2 ppm dissolved oxygen.

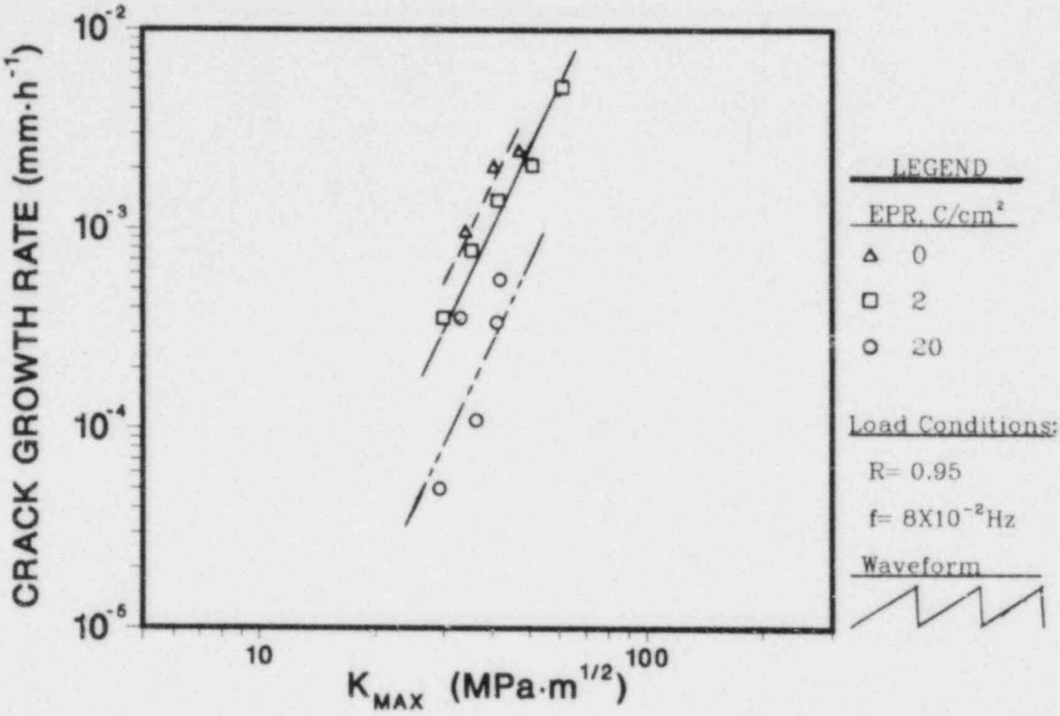

Fig. 66. Effect of Stress Intensity Factor on the Crack Growth Rate of Type 304 SS in 289°C Water with 0.2 ppm Dissolved Oxygen and 0.1 ppm Sulfate as H_2SO_4. Steady-state crack growth rates were obtained at a frequency and load ratio of 8 x 10^{-2} Hz and 0.95, respectively, for a positive sawtooth waveform.

F. Mechanistic Studies (W. E. Ruther, F. A. Nichols, and T. F. Kassner)

1. Introduction

The most likely mechanism for SCC of Type 304 SS in LWR systems involves the film rupture concept.[52] Plastic (creep) deformation of the alloy causes a buildup of displacements in surface layers, which, in turn, causes rupture of the inherently protective but relatively brittle film formed by chemical reaction between the alloy and the high-temperature water. Rupture of the film exposes a fresh, unprotected metallic surface at the crack tip. Subsequently, a new protective film forms on the newly exposed surface, but if metallic dissolution also occurs, the two processes compete with one another. SCC data from many different alloy/environment systems support this model. However, at least one modification of this concept needs to be considered, i.e., the assumption that incremental crack growth is due not to dissolution but to hydrogen embrittlement (HE). The potential/pH conditions in the solution within the crack can differ greatly from the bulk water such that hydrogen production and adsorption by the alloy at the crack tip can occur. Dissolution, though it may not significantly advance the crack, is necessary to keep the crack tip sharp enough for hydrogen to cause brittle crack advance. The sharp notch elevates the local stresses and couples the two concepts of the crack advance mechanism. However, the role of HE for significant crack advance in ductile-alloy/aqueous systems (e.g., Type 304 SS in BWR-quality water) has not been established.

The occurrence of HE, by any presently known process, requires the presence of hydrostatic stress near the crack tip.[53] This suggests that experiments involving Mode I (tensile) and Mode III (shear) loading can be used to better define the actual mechanism of crack advance. If HE is the mechanism, theory predicts no SCC for Mode III, which produces zero hydrostatic stress. Such comparative studies have been performed with high-strength steel[54] and titanium alloys[55,56] where the absence of SCC in Mode III strongly supports HE as the operative mode of crack advance. Such studies have not yet been performed for Type 304 SS or ferritic pressure vessel steels in aqueous environments; therefore, the primary experimental effort in this subtask is focused on this type of testing in simulated BWR environments.

2. Technical Progress

A schematic of the loading system for the Mode I and Mode III SCC experiments on sensitized Type 304 SS in simulated BWR-quality water is shown in Fig. 67. Water is supplied to the 1.5-ℓ autoclave system via a regenerative heat exchanger and a small preheater at the autoclave inlet of the once-through water system. The oxygen concentration of the feedwater is established by bubbling an appropriate oxygen/nitrogen gas mixture through deoxygenated/deionized water (conductance ~0.1 μS/cm) contained in a 120 ℓ stainless steel tank. Sulfuric acid is added to the feedwater prior to sparging with the gas mixture to ensure adequate mixing. A flow rate of ~0.6 ℓ/h at a pressure of 8.3 MPa is maintained in the autoclave.

SCC experiments under Mode I and Mode III loading are being performed at 289°C on notched specimens (Heat 30956) sensitized to an EPR value of 2 C/cm^2. This material exhibits a high susceptibility to IGSCC in oxygenated water containing 0.1 ppm sulfate as H_2SO_4 (Subtask E). Constant strain-rate tests were conducted in air at 289°C to determine the maximum tensile, σ_t^m, and torsional, σ_s^m, strengths of the notched specimens. The values are 654 and 577 MPa, respectively, and the corresponding yield stresses are 340 and 202 MPa, where ($\sigma_{ty} = 0.52\ \sigma_t^m$) and ($\sigma_{sy} = 0.35\ \sigma_s^m$).

Initial results of SCC tests in 289°C water containing 8 ppm dissolved oxygen and 0.1 ppm sulfate as H_2SO_4 are shown in Table XVI. Intergranular failure occurred under tensile loads at the higher stress levels; however, no failures were produced under torsion loading. Subsequently, the torsion specimens were fractured at liquid nitrogen temperature and an examination revealed no crack initiation during exposures up to ~800 h in the high-temperature environment. These results clearly indicate that crack initiation is more difficult under torsion load; however, the role of loading mode on crack propagation cannot be determined from the present results. Additional experiments under torsional loads will be performed on fatigue precracked specimens to overcome the problem of slow crack initiation. The fatigue precrack will also facilitate development of the crack-tip chemistry that may be necessary for propagation of a stress corrosion crack.

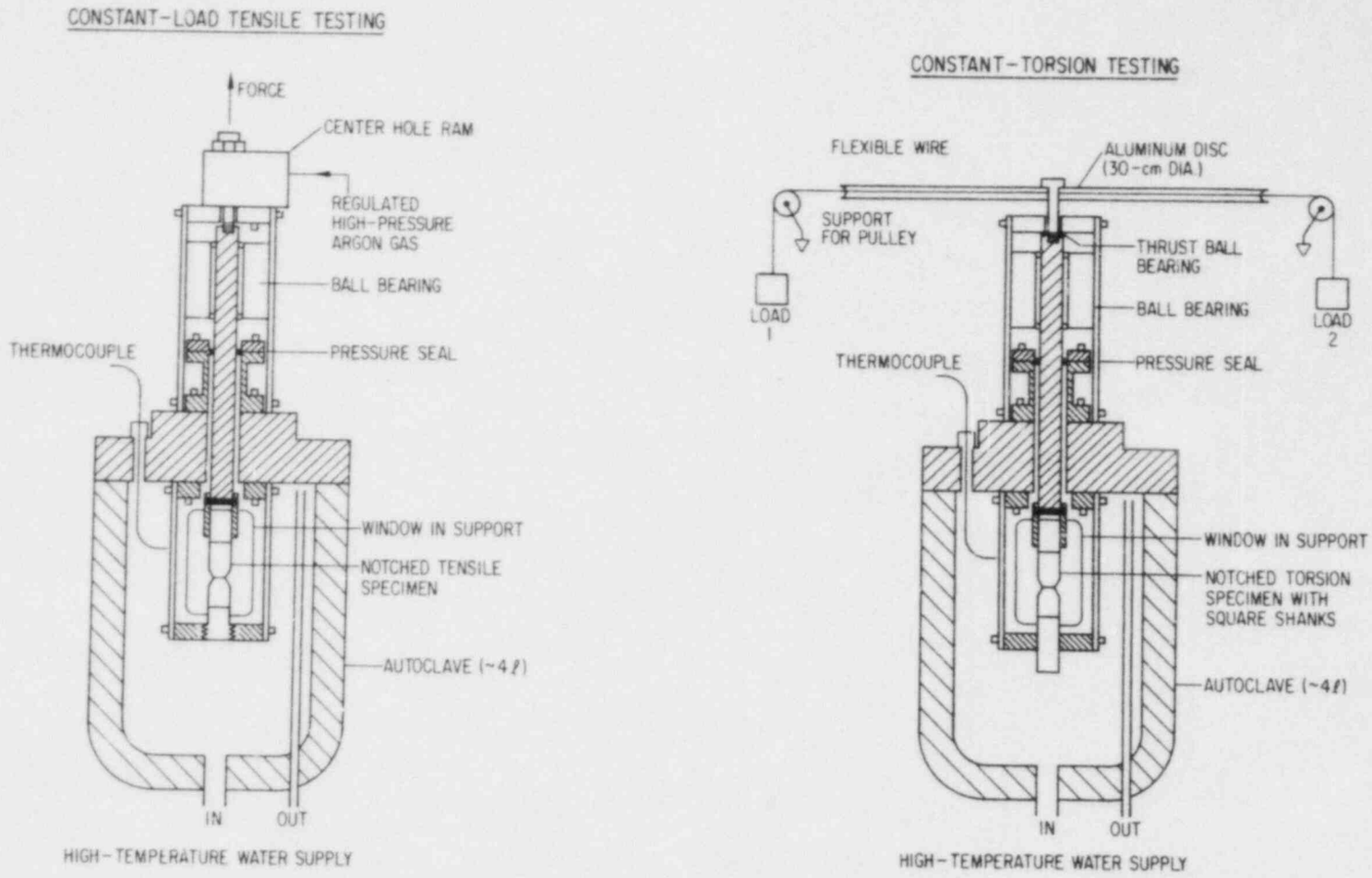

Fig. 67. Schematic of the (left) Tensile (Mode I) and (right) Shear (Mode III) Loading Systems for SCC Experiments in High-Temperature Water.

Table XVI. Stress vs Time to Failure Results from Constant Tensile and Torsion Load Experiments on Sensitized Type 304 SS Specimens (EPR = 2 C/cm^2) in 289°C Water with 8 ppm Dissolved Oxygen and 0.1 ppm Sulfate as H_2SO_4

Test No.	Loading Mode	Maximum Stress, MPa	Fractional Stress σ/σ^m	Failure Time, h	Fracture Morphology
TE-1	Tension	523	0.80	8.2	Intergranular
TE-6	↓	425	0.65	1.6	↓
TE-2	↓	392	0.60	6.6	↓
TE-5	↓	360	0.55	>715[a]	-
TE-4	↓	327	0.50	196	Intergranular
TE-3	↓	262	0.40	>216[a]	-
TO-2	Torsion	520	0.90	>794[a]	-
TO-1	Torsion	462	0.80	>479[a]	-

[a]Failure did not occur; the test was terminated at the indicated time.

REFERENCES

1. R. E. Henry, The Two Phase Critical Discharge of Initially Saturated or Subcooled Liquid, Nucl. Sci. Eng. 41, 336-342 (1970).

2. R. P. Collier, J. S. K. Liu, M. E. Mayfield and F. B. Stulen, Study of Critical Two Phase Flow Through Simulated Cracks, Battelle Columbus Laboratories, Interim Report BCL-EPRI-80-1 (November 1980).

3. D. S. Kupperman et al., in Environmentally Assisted Cracking in Light Water Reactors: Annual Report, October 1981 -- September 1982, NUREG/CR-3292, ANL-83-27, pp. 7-10 (February 1983).

4. D. S. Kupperman et al., in Materials Science Division Light-Water-Reactor Safety Research Program: Quarterly Progress Report, January-March 1982, NUREG/CR-2970 Vol. I, ANL-82-42 Vol. I, pp. 2-8 (October 1982).

5. E. J. Skudrzyk and G. P. Haddle, Noise Production in a Turbulent Boundary Layer by Smooth and Rough Surfaces, J. Acoust. Soc. Am. 32(1), 19-28 (1960).

6. P. H. Hutton, T. T. Taylor, J. F. Dawson, K. A. Pappas, and R. J. Kurtz, Acoustic Emission Monitoring of ASME Section III Hydrostatic Test, NUREG/CR-2880 (October 1982).

7. D. S. Kupperman et al., in Materials Science Division Light-Water-Reactor Safety Research Program: Quarterly Progress Report, April-June 1982, NUREG/CR-2970 Vol. II, ANL-82-41 Vol. II, pp. 2-9 (May 1983).

8. V. Cihal, Intercrystalline Corrosion of Corrosion Resistant Steels, Zaschch. Met. 4 (6), 637-655 (1968).

9. J. Y. Park, in Environmentally Assisted Cracking in Light Water Reactors: Annual Report, October 1981-September 1982, NUREG/CR-3292, ANL-83-27, pp. 23-29 (February 1983).

10. W. J. Shack et al., Environmentally Assisted Cracking in Light Water Reactors: Critical Issues and Recommended Research, NUREG/CR-2541, ANL-82-2, pp. 3.34-3.50 (February 1982).

11. J. Y. Park and D. S. Kupperman, Ultrasonic and Metallurgical Examination of a Cracked Type 304 Stainless Steel BWR Pipe Weldment, ANL-84-1 (November 1983).

12. J. Y. Park and W. J. Shack, in Environmentally Assisted Cracking in Light Water Reactors: Annual Report, October 1981-September 1982, NUREG/CR-3292, ANL-83-27, pp. 29-34 (February 1983).

13. F. P. Ford, A Mechanism of Environmentally Controlled Crack Growth of Structural Steels in High-temperature Water, General Electric Co. Report 81-CRD-125 (August 1981).

14. P. M. Scott and A. E. Truswell, "Corrosion Fatigue Crack Growth in Reactor Pressure Vessel Steels in PWR Primary Water," in Aspects of Fracture Mechanics in Pressure Vessels and Piping, PVP Vol. 58, American Society of Mechanical Engineers (1982).

15. J. R. Rice, "Mechanics of Crack Tip Deformation and Extension by Fatigue," in Fatigue Crack Propagation, ASTM STP 415 (1967).

16. E. W. Hart, Constitutive Relations for the Nonelastic Deformation of Metals, J. Eng. Mater. Technol., Trans. ASME, p. 193 (July 1976).

17. J. Y. Park, in Environmentally Assisted Cracking in Light Water Reactors: Annual Report, October 1981-September 1982, NUREG/CR-3292, ANL-83-27, pp. 23-25 (February 1983).

18. P. S. Maiya and W. J. Shack, in Ref. 17, pp. 35-38.

19. F. P. Ford and M. J. Povich, The Effect of Oxygen Temperature Combinations on the Stress Corrosion Susceptibility of Sensitized Type 304 Stainless Steel in High Purity Water, Corrosion, 35 (12), 569-574 (1979).

20. H. Choi, F. H. Beck, Z. Szklarska-Smialowska and D. D. MacDonald, Stress Corrosion Cracking of ASTM A508 C12 Steel in Oxygenated Water at Elevated Temperature, Corrosion, 38 (3), 136-144 (1982).

21. P. L. Andresen, Crack Initiation in CERT Tests on Type 304 Stainless Steel in Pure Water, Corrosion, 38(1), 53-59 (1982).

22. F. P. Ford, "Mechanism of Stress Corrosion Cracking," in Aspects of Fracture Mechanics in Pressure Vessels and Piping, PVP-Vol. 58; ASME, New York, N.Y. (1982), p. 229.

23. F. P. Ford, Mechanisms of Environmentally Enhanced Cracking in Systems Peculiar to the Power Generation Industry, EPRI NP-2589 (September 1982).

24. D. F. Mowbray, "Derivation of a Low-cycle Fatigue Relationship Employing the J-integral Approach to Crack Growth," in Cracks and Fracture, ASTM STP 601 (1976).

25. Donald Peckner and I. M. Bernstein, Handbook of Stainless Steels, McGraw-Hill Book Company, p. 27-3 (1977).

26. H. Takaku, M. Tokiwai, and H. Hirano, Effects of Cyclic Tensile Loading on Stress Corrosion Cracking Susceptibility for Sensitized Type 304 Stainless Steel in 290°C High Purity Water, Corrosion, 35 (11), 523-531 (1979).

27. P. S. Maiya, to be reported.

28. H. Yamada and Che-Yu Li, Stress Relaxation and Mechanical Equation of State in Austenitic Stainless Steels, Met. Trans. 4 (9), 2133-2136 (1973).

29. A. K. Miller, An Inelastic Constitutive Model for Monotonic, Cyclic and Creep Deformation Part I - Equations Development and Analytical Procedures, ASME J. Eng. Mater. Technol. Series H 96 (2), 97 (1976).

30. A. K. Miller and T. Tanaka, in Development of an Engineering Model for Predicting IGSCC Damage-Particularly in Type 304 Stainless Steel in BWR Water Environments, EPRI NP-2808-LD, Electric Power Research Institute, Prepared by S. Levy, Inc., Campbell, California (February 1983).

31. H. P. Offer et al., Techniques to Mitigate BWR PIpe Cracking in Existing Plants (Induction Heating Stress Improvement), 6th Semiannual Progress Report July 1981-December 1981, NEDC-25146-5, EPRI-RP1394-1, General Electric Co. (December 1981).

32. A. J. Gianuzzi, Ed., Residual Stress Improvement by Means of Induction Heating, Prepared by Ishikawajima-Harima Heavy Industries Co., Japan, EPRI NP-81-4-LD, Electric Power Research Institute (March 1981).

33. Revision to the Analyses and Repairs on Large-Diameter Piping Welds Submittal and RCS Leakage Detection Surveillance Commitment, Edwin I. Hatch Nuclear Plant Unit 2, Operating License NPF-5, USNRC Docket 50-366, (June 1983).

34. E. F. Rybicki et al., Residual Stresses at Girth-Butt Welds in Pipes and Pressure Vessels, NUREG-0376, Battelle Columbus Laboratories (1977).

35. E. F. Rybicki et al., Computational Residual Stress Analysis for Induction Heating of Welded BWR Pipes, EPRI NP-2662-LD, Electric Power Research Institute (1982).

36. ASME Boiler and Pressure Vessel Code, Winter Addenda, 1983, Section XI, IWB 3640.

37. S. Ranganath, "Prediction of Leak Rates," in The Growth and Stability of Stress Corrosion Cracks in Large Diameter BWR Piping, EPRI NP-2472 Vol. 2, Electric Power Research Institute (1982).

38. C. F. Shih et al., Methodology for Plastic Fracture, EPRI-NP-1735, Electric Power Research Institute (1981).

39. D. Kupperman, W. J. Shack, and T. Claytor, "Leak Rate Measurements and Detection Systems," in CSNI Leak-Before-Break Conference, Monterey California, September 1-2, 1983.

40. R. P. Collier et al., Study of Critical Two-Phase Flow Through Intergranular Stress Corrosion Cracks, Draft Report to the Electric Power Research Institute, Battelle Columbus Laboratories (1982).

41. D. Abdollahian and B. Chexal, Calculation of Leak Rates Through Cracks in Pipes and Tubes, EPRI NP-3395, Electric Power Research Institute (1983).

42. E. L. Burley, Oxygen Suppression in Boiling Water Reactors - Phase 2 Final Report, NEDC-23856-7, DOE/ET/34203-47 General Electric Company (October 1982).

43. W. Childs et al., Plant Materials Program: Progress June 1981 to May 1982, EPRI NP-2879-SR, Electric Power Research Institute (February 1983).

44. R. J. Kartz, D. W. Shannon, B. Francis, F. M. Kustas, and P. L. Koehmstedt, Evaluation of BWR Resin Intrusions on Stress Corrosion Cracking of Reactor Structural Materials, Final Report EPRI NP-3145, Electric Power Research Institute (June 1983).

45. R. H. Asay, J. Blok, and J. H. Holloway, Water Quality in Boiling Water Reactors, Final Report EPRI NP-1603, Electric Power Research Institute (November 1980).

46. F. H. Sweeton, R. E. Mesmer, and C. F. Baes, Jr., Acidity Measurements at Elevated Temperature; VII. Dissociation of Water, J. Solu. Chem. 3(3), 191-214 (1974).

47. W. L. Marshall and E. V. Jones, Second Dissociation Constant of Sulfuric Acid from 25 to 350°C Evaluated from Solubilities of Calcium Sulfate in Sulfuric Acid Solutions, J. Phys. Chem. 70(12), 4028-4040 (1966).

48. L. W. Niedrach, Use of a High Temperature pH Sensor as a "Pseudo-Reference Electrode" in Monitoring of Corrosion and Redox Potentials at 285°C, J. Electrochem. Soc. 129(7), 1445-1449 (1982).

49. W. E. Ruther et al., in Materials Science and Technology Division Light-Water Reactor Safety Research Program: Quarterly Progress Report, April-June 1983, NUREG/CR-3689 Vol. II, ANL 83-85 Vol. II (June 1984), pp. 31-57.

50. W. E. Ruther et al., in Materials Science and Technology Division Light-Water Reactor Safety Research Program: Quarterly Progress Report, January-March 1983, NUREG/CR-3689 Vol. I, ANL-83-85 Vol. I (April 1984), pp. 47-59.

51. W. E. Ruther, W. K. Soppet, G. Ayrault, and T. F. Kassner, Effect of Sulfuric Acid, Oxygen, and Hydrogen in High-Temperature Water on Stress Corrosion Cracking of Sensitized Type 304 Stainless Steel, to be published Corrosion 40 (1984).

52. H. L. Logan, Film-Rupture Mechanism of Stress Corrosion, J. Res. Nat. Bur. Stand. 48, 99 (1952).

53. A. W. Thompson, Current Status of the Role of Hydrogen in Stress Corrosion Cracking, Mater. Sci. Eng. 43, 41 (1980).

54. C. St. John and W. W. Gerberich, The Effect of Loading Mode on Hydrogen Embrittlement, Met. Trans. 4, 589 (1973).

55. J. A. S. Green, H. W. Hayden, and W. C. Montague, "The Influence of Loading Mode on the Stress Corrosion Susceptibility of Various Alloy/Environment Systems," in Effect of Hydrogen on Behavior of Materials, eds. A. W. Thompson and I. M. Bernstein, TMS-AIME, New York (1976), p. 200.

56. J. A. Green and H. W. Hayden, "Influence of Two Modes of Loading on the Stress Corrosion Susceptibility of Ti-8Al-1Mo-1V Alloy in Various Chloride-Containing Environments," in Hydrogen in Metals, eds. I. M. Bernstein and A. W. Thompson, ASM, Metals Park, OH (1974), p. 235.

Distribution for NUREG/CR-3806 (ANL-84-36)

Internal:

R. Avery
G. Ayrault
E. S. Beckjord
M. Blander
F. A. Cafasso
O. K. Chopra
H. M. Chung
T. N. Claytor
L. W. Dietrich
D. R. Diercks
F. Y. Fradin
B. R. T. Frost
D. M. Gruen
P. R. Huebotter
T. F. Kassner (10)
K. L. Kliewer
D. S. Kupperman
P. S. Maiya
V. A. Maroni
K. Natesan
F. A. Nichols
F. S. Onesto
J. Y. Park
R. B. Poeppel
K. J. Reimann
J. Rest
G. S. Rosenberg
W. Ruther
W. J. Shack (3)
W. K. Soppet
E. M. Stefanski (2)
C. E. Till
R. A. Valentin
R. W. Weeks
H. Wiedersich
R. S. Zeno
ANL Patent Dept.
ANL Contract File
ANL Libraries (3)
TIS Files (6)
D. K. Moores

External:

NRC, for distribution per R5 (350)
DOE-TIC (2)
Manager, Chicago Operations Office, DOE
R. Dalton, DOE-CH
Materials Science and Technology Division Review Committee:
B. Alcock, U. Toronto
A. Arrott, Simon Fraser U.
R. C. Dynes, Bell Labs., Murray Hill
A. G. Evans, U. California, Berkeley
L. M. Falicov, U. California, Berkeley
H. K. Forsen, Bechtel Group, San Francisco
E. Kay, IBM San Jose Research Lab.
B. Maple, U. California, San Diego
C. L. McCabe, Cabot Corp., Kokomo, Ind.
P. G. Shewmon, Ohio State U.
J. Tien, Columbia U.
R. B. Adamson, General Electric Co., Vallecitos Nuclear Center, P. O. Box 460, Pleasanton, Calif. 94566
P. L. Andresen, General Electric Corporate Research and Development, Schenectady, N.Y. 12301
G. A. Arlotto, Office of Nuclear Regulatory Research, USNRC, Washington
D. Atteridge, Battelle Pacific Northwest Lab., P. O. Box 999, Richland, Wash. 99352
W. Berry, Battelle-Columbus Labs., 505 King Ave., Columbus, OH 43201
C. Y. Cheng, Office of Nuclear Reactor Regulation, NSNRC, Washington
R. A. Clark, Battelle Pacific Northwest Lab., P. O. Box 999, Richland, Wash. 99352
W. J. Collins, Office of Inspection and Enforcement, USNRC, Washington
G. Cragnolino, Dept. of Metallurgical Engineering, Ohio State U., Columbus, OH 43210
D. Cubiciotti, Electric Power Research Inst., P. O. Box 10412, Palo Alto, Calif. 94304
J. C. Danko, Electric Power Research Inst., P. O. Box 10412, Palo Alto, Calif. 94304

B. J. Elliot, Office of Nuclear Reactor Regulation, USNRC, Washington
M. Fox, Fox Enterprises, 7490 Stanford Place, Cupertino, Calif. 95014
Y. S. Garud, S. Levy, Inc., 1901 S. Bascom Ave., Campbell, Calif. 95008
J. H. Gittus, Springfields Nuclear Power Development Labs., U.K. Atomic Energy Authority, Springfields, Salwick, Preston, PR4 ORR, England
D. O. Harris, 750 Welch Rd., Palo Alto, Calif. 94304
W. S. Hazelton, Office of Nuclear Reactor Regulation, USNRC, Washington
R. E. Johnson, Office of Nuclear Reactor Regulation, USNRC, Washington
W. V. Johnston, Office of Nuclear Reactor Regulation, USNRC, Washington
R. L. Jones, Electric Power Research Inst., P. O. Box 10412, Palo Alto, Calif. 94304
P. M. Lang, Office of Converter Reactor Deployment, USDOE, Washington, D. C. 20545
J. Muscara, Office of Nuclear Regulatory Research, USNRC, Washington
D. M. Norris, Electric Power Research Inst., P. O. Box 10412, Palo Alto, Calif. 94304
D. R. O'Boyle, Commonwealth Edison Co., P. O. Box 767, Chicago, Ill. 60690
J. T. A. Roberts, Electric Power Research Inst., P. O. Box 10412, Palo Alto, Calif. 94304
E. J. Rowley, Commonwealth Edison Co., P. O. Box 767, Chicago, Ill. 60690
E. F. Rybicki, Dept. of Mechanical Engineering, Univ. of Tulsa, Tulsa, Okla. 74110
C. Z. Serpan, Office of Nuclear Regulatory Research, USNRC, Washington
L. Shao, Office of Nuclear Regulatory Research, USNRC, Washington
R. D. Silver, Office of Nuclear Reactor Regulation, USNRC, Washington
L. J. Sobon, NUTECH Engineers, 6835 Via del Oro, San Jose, CA 95119
A. A. Solomon, School of Nuclear Engineering, Purdue U., West Lafayette, Ind. 47907
D. M. Stevens, Lynchburg Research Center, Babcock & Wilcox Co., P. O. Box 239, Lynchburg, VA 24505-0239
J. Strosnider, Office of Nuclear Regulatory Research, USNRC, Washington
A. Taboada, Office of Nuclear Regulatory Research, USNRC, Washington
J. R. Weeks, Brookhaven National Lab., Upton, N.Y. 11973
K. R. Wichman, Office of Nuclear Reactor Regulation, USNRC, Washington

NRC FORM 335 (2.84) NRCM 1102, 3201, 3202

U.S. NUCLEAR REGULATORY COMMISSION

BIBLIOGRAPHIC DATA SHEET

SEE INSTRUCTIONS ON THE REVERSE

1. REPORT NUMBER (Assigned by TIDC and Vol. No., if any)

NUREG/CR-3806
ANL-84-36

2. TITLE AND SUBTITLE

ENVIRONMENTALLY ASSISTED CRACKING IN LIGHT WATER REACTORS: ANNUAL REPORT, October 1982—September 1983

3. LEAVE BLANK

4. DATE REPORT COMPLETED

MONTH: June — YEAR: 1984

5. AUTHOR(S)

W. J. Mack, T. F. Kassner, D. S. Kupperman, T. N. Claytor, J. Y. Park, P. S. Maiya, W. E. Ruther, and F. A. Nichols

6. DATE REPORT ISSUED

MONTH: August — YEAR: 1984

7. PERFORMING ORGANIZATION NAME AND MAILING ADDRESS (Include Zip Code)

Argonne National Laboratory
9700 South Cass Avenue
Argonne, Illinois 60439

8. PROJECT/TASK/WORK UNIT NUMBER

9. FIN OR GRANT NUMBER

A2212

10. SPONSORING ORGANIZATION NAME AND MAILING ADDRESS (Include Zip Code)

U. S. Nuclear Regulatory Commission
Office of Nuclear Regulatory Research
Washington, D. C. 20555

11a. TYPE OF REPORT

Technical; annual

b. PERIOD COVERED (Inclusive dates)

Oct. 1982—Sept. 1983

12. SUPPLEMENTARY NOTES

13. ABSTRACT (200 words or less)

This progress report summarizes work performed by the Argonne National Laboratory and subcontractors at GARD Inc., Pacific Northwest Laboratory, and E. F. Rybicki, Inc. on environmentally assisted cracking in light water reactors during the twelve months from October 1982 through September 1983.

14. DOCUMENT ANALYSIS — a. KEYWORDS/DESCRIPTORS

stress corrosion cracking
leak detection
inservice inspection
crack growth
water chemistry
acoustic emission

b. IDENTIFIERS/OPEN-ENDED TERMS

15. AVAILABILITY STATEMENT

Unlimited

16. SECURITY CLASSIFICATION

(This page) unclassified

(This report) unclassified

17. NUMBER OF PAGES

18. PRICE